A ca. 273-261 Ma multi-component arc pluton in the southern area of the Beishan Orogenic Collage, NW China: a geochronological, geochemical, and petrogenetic analysis

by

Quinn Worthington

A thesis
presented to the University of Waterloo
in fulfillment of the
thesis requirement for the degree of
Master of Science
in
Earth Sciences

Waterloo, Ontario, Canada, 2022

Author's Declaration

This thesis consists of material all of which I authored or co-authored: see Statement of Contributions included in the thesis. This is a true copy of the thesis, including any required final revisions, as accepted by my examiners.

I understand that my thesis may be made electronically available to the public.

Statement of Contributions

Due to COVID-19, travel to the field site and the SHRIMP lab in China was not possible. The following contributors assisted in data collection of the specified sections. All other parts of this thesis, including analysis and interpretations, are my own work.

Field work: conducted by Shoufa Lin who elucidated the field relationships.

Petrology and geochemistry samples: collected by Longming Li, Hang Liu, Shoufa Lin and Tong Hong.

Geochronology samples: collected by Longming Li, Hang Liu and Shoufa Lin.

SHRIMP analysis: Analysis for samples 20LYS-5301, 20LYS-5302, and 20LYS-5304 was conducted by Chaoyang Wang, under the supervision of Peizhi Wang. Analysis for sample 17LYS-5018 was conducted by Tong Hong, assisted by Lamei Feng, under the supervision of Chunyan Dong. Initial data processing was performed by Peizhi Wang and Chunyan Dong.

Abstract

Along the southern edge of the Central Asian Orogenic Belt lies the Beishan Orogenic Collage, bridging the Tianshan Orogen (west) to the Mongolia-Xing'anling Orogen (east). The Beishan Orogenic Collage is thought to represent the final stages of closure of the Paleo-Asian Ocean, and consequently the last tectonic events in the orogeny. The tectonic setting of the region has been a long-standing point of contention, and the timing and location of final ocean closure is highly debated. This study focuses on the geochemistry, geochronology, and petrogenesis of the multi-component Nanquan Quarry pluton located at the southernmost edge of the Beishan, providing new insight into the controversial and poorly understood tectonic history of the region. The pluton is hosted in the South Baidunzi Complex and consists of mingled quartz-diorite and quartz-monzonite, which are intruded by granodiorite. The quartz-diorite and quartz-monzonite both have geochemical signatures indicative of an arc setting, and the granodiorite has a post-collisional and adakitic signature. The mingled mixture of quartz-diorite and quartz-monzonite yielded SHRIMP U-Pb ages of ca. 273 Ma, while the granodiorite yielded a SHRIMP U-Pb age of ca. 261 Ma. This new data suggests subduction was still active in the Beishan Orogenic Collage between 273 – 261 Ma, ca. 10 Ma later than suggested by previous models. This study suggests that the Nanquan Quarry arc formed in either a north-dipping subduction zone between a terrane from the Dunhuang Orogenic Belt and the South Baidunzi Complex, or a south-dipping subduction zone between the North Baidunzi Complex and the South Baidunzi Complex. This new information about the most recent tectonic stage of the Paleo-Asian Ocean could help better define the history of the Central Asian Orogenic Belt.

Acknowledgments

There are so many people I would like to acknowledge in this section, I don't even know where to begin. First of all, thank you to my supervisor Dr. Shoufa Lin (University of Waterloo) for taking me on as a student. I'm sure you weren't expecting what I had in store for us these past few years, but I thank you for your kindness, patience, understanding, and encouragement through it all. Thank you for working with me and find a project through all the unexpected hurdles, for coordinating with members of the Chinese Geological Survey to help with funding, sample collecting, and communicating with the personnel at the Beijing SHRIMP Center in the Chinese Academy of Geological Sciences. Special thanks to my committee members Jen Parks, Chris Yakymchuk, and Cees van Staal for the advice and expertise, especially since they all keep busy schedules. I am extremely grateful for Tong Hong and Gabriel Santos for their endless advice, patience with my questions, and time taken to edit and proofread for me.

I quite literally would not be here today without the help and support of friends, family, colleagues, and the various medical personnel in China. A big thank you goes to Gabe, Jordy, and Shoufa, who kept me in good spirits, and the biggest thank you goes to my mom and Tong for forcing me to take care of my personal health. Thanks to these people, the only appendix I have is located on page 68. Although my time was short, Liuyuan will forever have a special place in my heart.

And of course, so much love and gratitude go to my family for the constant support and encouragement throughout these unpredictable few years. Thank you to my roommates, officemates, and down-the-hall-friends for the morale boosts, extended coffee breaks, and comradery; to Jen for the continuous mentorship and friendship since my undergrad; and to everybody else, of which I cannot possibly name them all, for making my experience at Waterloo memorable.

Table of Contents

AUTHOR'S DECLARATION ..... **ii**

STATEMENT OF CONTRIBUTIONS ..... **iii**

ABSTRACT ..... **iv**

ACKNOWLEDGMENTS ..... **v**

LIST OF FIGURES ..... **viii**

LIST OF TABLES ..... **xi**

1.0 INTRODUCTION **1**

1.1 Purpose and objectives 1

1.2 Location and accessibility 2

2.0 REGIONAL AND LOCAL GEOLOGY **3**

2.1 Central Asian Orogenic Belt 3

2.2 Beishan Orogenic Collage 5

2.2.1 Liuyuan Complex *6*

2.2.2 North and South Baidunzi Complex *6*

2.3 Dunhuang Orogenic Belt 8

3.0 FIELD RELATIONSHIPS AND PETROGRAPHY **10**

3.1 Site locality 10

3.2 Lithology groups and Field Relationships 12

3.2.1 Quartz-diorite *15*

3.2.2 Quartz-monzodiorite *16*

3.2.3 Granodiorite *18*

3.3 Deformation textures 19

4.0 U-PB GEOCHRONOLOGY **22**

4.1 Analytical Techniques 22

4.2 Results 22

4.2.1 Sample 20LYS-5304b: Quartz-monzodiorite *23*

4.2.2 Sample 17LYS-5018: Quartz-diorite *23*

4.2.3 Sample 20LYS-5301b: Quartz-diorite *24*

4.2.4 Sample 20LYS-5302b: Granodiorite *24*

4.3 Comparing core and rim ages 25

4.4 Timeline Summary 32

5.0 GEOCHEMISTRY 33

5.1 Analytical Techniques 33
5.2 Normative Mineralogy 33
5.3 Major Element Oxides 35
5.4 Trace Elements 38
5.4.1 Trace Element Anomalies 41
5.5 Rare-earth Elements 43
5.5.1 Quartz-diorite 43
5.5.2 Quartz-monzodiorite 43
5.5.3 Granodiorite 43
5.6 Conserved Element Analysis 44
5.7 Geochemical affinities and tectonic setting 47
5.7.1 Quartz-diorite 47
5.7.2 Quartz-monzodiorite 47
5.7.3 Granodiorite 48
5.8 Implications of the Geochemical Data 50

6.0 SUMMARY AND DISCUSSION 51

6.1 Summary 51
6.1.1 Petrography and Field Relationships 51
6.1.2 U-Pb Geochronology 51
6.1.3 Geochemistry 52
6.2 Tectonic Implications 52
6.2.1 Current Tectonic History Model 52
6.2.2 Generation of the Nanquan Arc 53

7.0 CONCLUSIONS AND FUTURE WORK 58

7.1 Conclusions 58
7.2 Future Work 58

REFERENCES 60

APPENDIX 68

List of Figures

Figure 1: (A) Simplified geological map of the Central Asian Orogenic Belt (modified from Xiao et al, 2015). (B) Simplified geological terrane map of the Beishan Orogenic Collage (modified from Cleven, 2017). 4

Figure 2: New tectonic model depicting the closure of the Paleo-Asian Ocean and generation of the Liuyuan complex, proposed by Santos et al., (2022). 6

Figure 3: Simplified geologic map showing site locality (orange box). Note the south-dipping thrust fault that seperates the North Baidunzi Complex from the South Baidunzi Complex. Modified from van Staal et al., (2019). 8

Figure 4: Aerial photo of Nanquan Quarry pluton (circled in red dashed line). Note the thrust fault immediately to the north of the pluton, and the generally E-W lineaments of the garnet-hornblende orthogneiss country rock. Sample collection locations denoted by coloured stars. 11

Figure 5: Field relationships: (A) Net-vein texture between quartz-diorite and quartz-monzodiorite. (B) Tube-like structure. (C) Structures resembling load cast structures. (D) Irregular sharp contact between quartz-monzodiorite and quartz-diorite. (E) Gradational contact between quartz-diorite and quartz-monzodiorite. (F) Sharp intrusive contact between lineated quartz-diorite and fine-grained granodiorite. (photos taken by Shoufa Lin) 13

Figure 6: Hand sample photos: (A) Foliated quartz-diorite. (B) Non-foliated quartz-diorite. (C) Foliated quartz-monzodiorite. (D) Non-foliated quartz-monzodiorite. (E) Granodiorite. (photo E was taken by Shoufa Lin) 14

Figure 7: Photomicrographs of quartz-diorite samples: (A)Foliated sample. (B) Non-foliated sample. (C) Porphyritic sample. (D) Olivine grains in sample. (E) Clinopyroxene core surrounded by hornblende rim. (F) Interstitial hornblende. 20

Figure 8: Photomicrographs of granodiorite: (A) Inequigranular with myrmekite texture. (B) Inequigranular with coarse zoned plagioclase. 21

Figure 9: Photomicrographs of quartz-monzodiorite: (A) Weakly foliated, defined by biotite and hornblende. (B) Inequigranular. (C) Myrmekite embayment texture. (D) Quartz intergrown with hornblende and biotite. 21

Figure 10: Cathodoluminescence photographs of representative zircon grains from each dated sample. Yellow circle denotes analysis location and the calculated age is beside each analysis spot. Zircon grains from the quartz-monzodiorite sample are in the yellow rectangle, zircon grains from the quartz-diorite samples (directly from or inherited) are in the blue rectangle, and zircon grains from the granodiorite are in the green rectangle... 26
Figure 11: Geochronological data for sample 20LYS-5304 (quartz-monzodiorite). Wetherill Concordia diagram, where blue ellipses are included in age calculation and yellow ellipses are excluded due to high uranium. (A) Data from all spots. (B) Weighted mean. (C) Concordant data, excluding outliers. 27
Figure 12: Geochronological data for sample 17LYS-5018 (quartz-diorite). Wetherill Concordia diagram, where blue ellipses are included in age calculation and yellow or grey ellipses are excluded due to high uranium and being outliers, respectively. (A) Data from all spots. (B) Weighted mean. (C) Concordant data, excluded outliers. 28
Figure 13: Geochronological data for sample 20LYS-5301 (quartz-diorite). Wetherill Concordia diagram, where blue ellipses are included in age calculation and yellow or grey ellipses are excluded due to high uranium and being outliers, respectively. (A) Data from all spots. (B) Weighted mean. (C) Concordant data, excluded outliers. 29
Figure 14: Geochronological data for sample 20LYS-5302 (granodiorite). Wetherill Concordia diagram, where blue ellipses are included in age calculation and yellow or grey ellipses are excluded due to high uranium or being outliers, respectively. (A) Data from all spots. (B) Weighted mean. (C) Concordant data for inherited population, excluded outliers. (D) Concordant data for new younger population, excluded outliers. 30
Figure 15: Concordia diagrams comparing the core ages with rim ages, where yellow and grey ellipses have been excluded from the concordia calculation due to high uranium and being outliers, respectively. 20LYS-5301 is a quartz-diorite sample and 20LYS-5304 is a quartz-monzodiorite sample. (A) Concordant from rim spots from 20LYS-5301. (B) Concordant from rim spots from 20LYS-5304. (C) Concordant from core spots from 20LYS-5301. (D) Concordant from core spots from 20LYS-5304..... 31
Figure 16: Timeline showing the relative ages of zircon populations from all dated samples. The mingled quartz-diorite, quartz-monzodiorite, and inherited zircons suggest the pluton formed between ca. 275 and 266 Ma, while the granodiorite intruded ca. 261 Ma. 32

Figure 17: CIPW Normative mineralogy QAP plot. This plot was created using geochemical data, not based on mineral percentages viewed in thin section. 34
Figure 18: Major Element Harker plots for all samples 37
Figure 19: Trace element Harker plots for all samples 40
Figure 20: Trace element spider diagrams for all samples. Trace element anomaly patterns discussed in Section 5.4.1 can be seen here. 42
Figure 21: Rare-Earth Element spider diagrams of all samples 45
Figure 22: Conserved element analysis plot. The quartz-diorite and quartz-monzodiorite samples lie along a straight line that intersects at the origin, while the granodiorite does not follow the trend. 46
Figure 23: Geotectonic discrimination diagrams: 49
Figure 24: Summative diagram Scenario 1 of the formation of the Nanquan Arc. (A) The North Baidunzi Complex and South Baidunzi Complex are brought together through strike-slip movement along the fault from 277-271 Ma. (B) Northward subduction of a terrane from the Dunhuang Orogenic Belt under the South Baidunzi Complex from 273-269 Ma to create the Nanquan arc, where the quartz-diorite and quartz-monzodiorite magmas mingled to form the pluton. (C) Collision between the terrane from the Dunhuang Orogenic Belt and the South Baidunzi Complex occurred before 261 Ma, when post-collisional granodiorite dikes intruded the Nanquan Quarry pluton. 56
Figure 25: Summative diagram Scenario 2 of the formation of the Nanquan Arc. (A) Subduction of the North Baidunzi Complex under a terrane from the Dunhuang Orogenic Belt and the South Baidunzi Complex occurs from 284-275 Ma to create arc magmatism (Feng et al., 2020) (B) Subduction ceases after 275 Ma due to collision of the two terranes. Slab break-off occurs and creates Nanquan Quarry arc-like magmatism from 273-269 Ma, where the quartz-diorite and quartz-monzodiorite magmas mingled to form the pluton. (C) Post-collisional magmatism occurs around 261 Ma to create the adakitic granodiorite dike intrusions. 57

List of Tables

Table 1: Characteristics of an adakite rock defined by Defant and Drummond (1990), compared to characteristics of the granodiorite samples in this study 50
Table 2: List and general description of all samples collected 68
Table 3: Geochronological data for sample 17LYS-5018 70
Table 4: Geochronological data for sample 20LYS-5301 71
Table 5: Geochronological data for sample 20LYS-5302 72
Table 6: Geochronological data for sample 20LYS-5304 73
Table 7: Geochronological measurements on Temora 1 standard zircons 74
Table 8: Whole-rock geochemistry data for all samples 75

1.0 Introduction

For millions of years, plate tectonics have rearranged the Earth's lithosphere and orogenesis plays a major role in reworking the crust. Evidence from modern-day outcrops is often used to create tectonic models which aim to reconstruct the processes that paleo-Earth's lithosphere was subjected to. The Central Asian Orogenic Belt is the largest multi-staged Paleozoic accretionary orogen, and it hosts a variety of collages that developed during its many stages (Figure 1A). The Beishan Orogenic Collage is the southernmost part of the Central Asian Orogenic Belt and presumably the youngest (Xiao et al. 2010). The Beishan is a pivotal joining place for the surrounding orogens and cratons. In addition to connecting the Tarim and North China Cratons to the south, it also connects the Tianshan Suture (west) with the Solonker Suture (east), bridging the respective Tianshan and Mongolian-Xing'anling Orogens (Xiao et al. 2010) (Figure 1). South of the Beishan lies the Dunhuang Orogenic Belt, which is also proposed to be an accretionary orogen (Zhao et al. 2016, Feng et al. 2020) (Figure 1).

The tectonics and timing in the Beishan region are highly debated, but of crucial importance in understanding the complex history of the formation of central Asia. The final closure of the Paleo-Asian Ocean suspectedly occurred in the Beishan region, as it is the youngest section of this orogen, through the subduction and consumption of the surrounding crustal fragments. There are many sutures between petrogenetically unique terranes within Beishan and studying this area in detail is pivotal in determining when and where the last section of the Paleo-Asian Ocean finally closed. Multiple higher resolution studies are needed in this area to better define the tectonic history of each individual terrane in order to refine the proposed tectonic model that describes the end of the Central Asian Orogen. Creating this tectonic model that reconstructs the movement and interaction paleo-Earth's lithosphere and mantle in a long-lived accretionary orogen can be used to help explain the formation of Earth's largest continent.

1.1 Purpose and objectives

The Beishan Orogenic Collage is a relatively understudied area that boasts abundant outcrop exposure, important structural contacts, and well-preserved age relationships. This study aims to further define and constrain the timing of the tectonic events that occurred in the southern area of the Beishan. An unstudied multi-component pluton is located at the

southernmost edge of the Beishan, hereon referred to as the Nanquan Quarry pluton (Figure 1B, 3). Preliminary data collected during a reconnaissance work indicates this intrusion is younger than other parts of Beishan and understanding its tectonic setting may be pivotal in determining the timing and location of final closure of the Paleo-Asian Ocean. This suite of rocks provides a wealth of information that can be used to determine whether the pluton correlates to a neighbouring terrane or craton, or whether it is completely unique which could propose a new stage in the tectonic history of the Beishan.

The objectives of this study are to (1) define the tectonic setting of the Nanquan Quarry pluton, (2) constrain the timing of formation, and (3) further constrain the tectonic models that interpret the final stages of the Beishan Orogenic Collage and by association, the Central Asian Orogenic Belt. This thesis uses field relationships, petrography, geochronology data, and geochemistry data to determine the geologic history of the pluton.

1.2 Location and accessibility

The study area of this thesis is located in northwestern China, approximately 2.5 km southwest of Baidunzi, Guazhou County, Jiuquan, Gansu Province. The Nanquan Quarry pluton is approximately 1.5 km by 1 km with the coordinates of 40.82938252, 95.5774242.

Access to the general study area is available via the G30 or G312/G215 highway. There is an abandoned quarry in one area of the pluton, and as a result, there is a network of unnamed service roads that run through the study area. An off-roading four-by-four vehicle is recommended to access the Nanquan Quarry pluton.

Local topography of the area consists of low-relief rocky hills surrounded by flat, non-vegetated outwash plains that consist of modern sediment. Outcrop exposure in this area was created by both natural erosion caused by high winds and seasonal precipitation, and modern quarrying practices.

2.0 Regional and Local Geology

2.1 Central Asian Orogenic Belt

The Central Asian Orogenic Belt is the largest multi-stage accretionary orogen that developed in the Paleozoic. This expansive record of crustal reworking events is bordered by the Siberian Craton (north), the Baltica Craton (north-west), and the Tarim and North China Cratons (south) (Figure 1A). Major controversies about the formation of the Central Asian Orogenic Belt include the polarity of subduction, timing of suturing, and origin of terranes. Many models have been proposed in attempts to describe the orogen formation, including a wide single arc-subduction system named the Kipchak arc (Şengör et al. 1993, Wang et al. 2003), a series of two or three individual successive arcs (Zuo et al. 1991, Yakubchuk 2004), and a series of multiple island arcs, microcontinental blocks, and continental margin arcs (Windley et al. 2007, Wilhem et al. 2012). The latter Indonesian-type model is the most accepted and suggests that multiple subduction zones were simultaneously consuming sections of the Paleo-Asian Ocean.

The most contentious argument about the formation of this orogen is at what time the Paleo-Asian Ocean finally closed. Various authors have proposed different dates that span over 140 million years, ranging from the Silurian at 430 Ma (Wang et al. 2017a, He et al. 2018) to mid-Permian at 282 Ma (Xiao et al. 2010, Mao et al. 2012a, Santos et al. 2022a). Most of the controversy lies in the Beishan Orogenic Collage that hosts many terranes that produced ages within the 140 million year range.

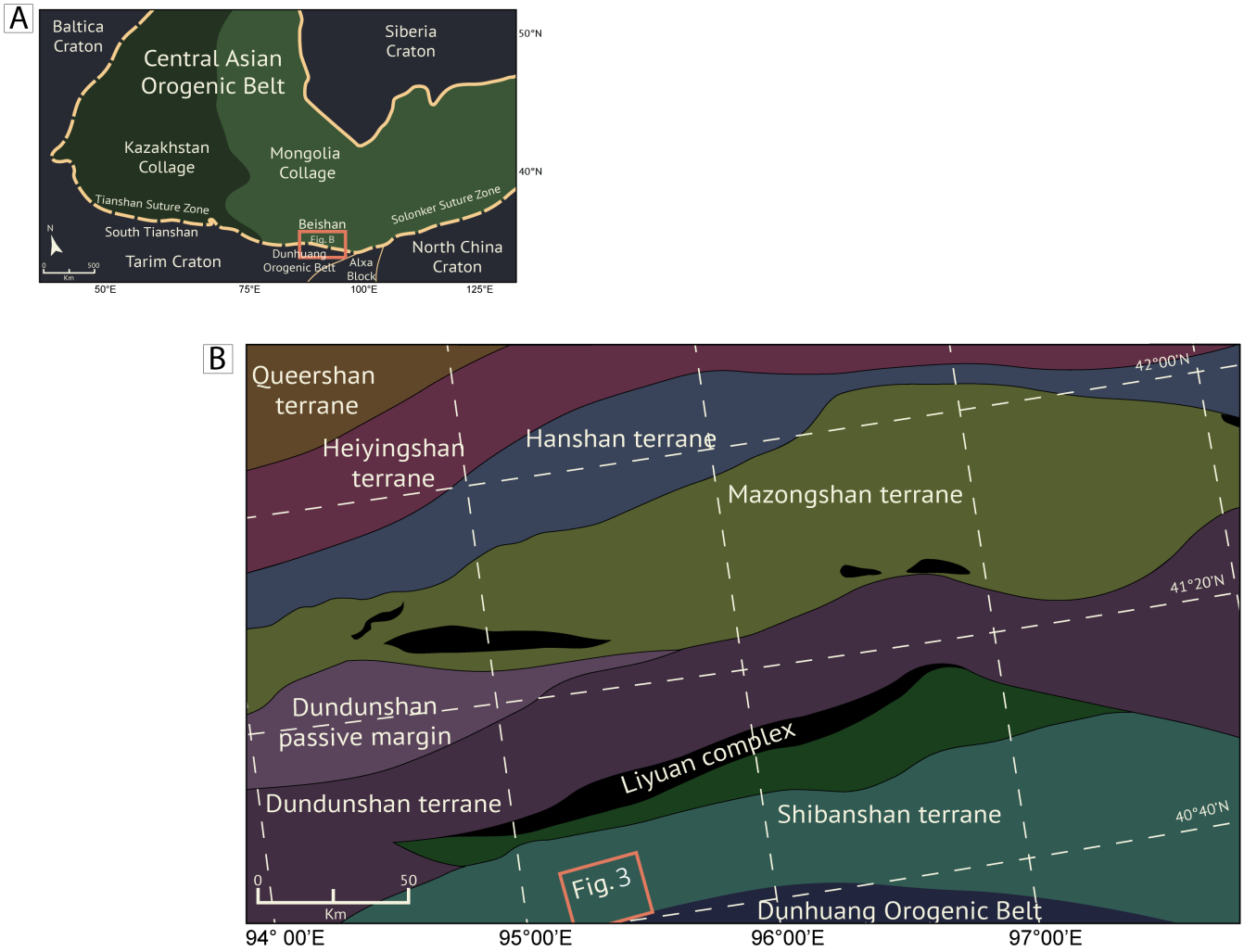

Figure 1: (A) Simplified geological map of the Central Asian Orogenic Belt (modified from Xiao et al, 2015). (B) Simplified geological terrane map of the Beishan Orogenic Collage (modified from Cleven, 2017).

2.2 Beishan Orogenic Collage

The Beishan Orogenic Collage, situated at the southern edge of the Central Asian Orogenic Belt, is presumed to be the youngest section of the orogen and is thought to represent the final stages of amalgamation (Figure 1B). It is the region that connects the Central Asian orogen with the Tarim and North China Cratons to the south, and the Tianshan orogen and Mongolia-Xing'anling orogen to the west and east, respectively. It also is bordered by the Dunhuang Orogenic Belt to the south. The Beishan is a juncture of these different systems and its geologic history could be critical in understanding the formation of these orogens, yet major controversies still exist and a consensus on the geologic history has not yet been reached (Xiao et al. 2010). Several studies have been done in the area, however, most have a very limited scope and lack the detail required to make reliable tectonic interpretations. There are very few studies that systematically map an area, resulting in widespread and sparse outcrop maps. In addition, a consistent naming system for some terranes is lacking amongst different researchers which leads to confusion.

Despite the complication and lack of thorough studies, there are two main theories that try to explain the tectonic setting of the area: intracontinental rifting, folding, and thrusting (Gao et al. 1995, Zhang and Cunningham 2012, Wang et al. 2017a, He et al. 2018), or the final closure and suturing of the Paleo-Asian Ocean (Xiao et al. 2010, Mao et al. 2012a, Tian et al. 2013, Huang et al. 2015, Santos et al. 2022b). The Beishan is composed of many distinct terranes that have experienced some degree of metamorphism, including arcs, microcontinents, basins, and ophiolites (Xiao et al. 2010). The main arc terrane units that make up the Beishan Orogenic Collage from north to south are as follows: Queershan arc, Heiyingshan arc, Hanshan arc, Mazongshan arc, Dundunshan arc, and Shibanshan arc; with various ophiolite sequences or mélange zones between these terranes (Figure 1B).

The study area for this thesis is part of a large-scale mapping project that reaches over 50 km north of the study site and has been in progress for many years. The objective of the mapping project is to better define the tectonic setting and timing of parts of the Beishan Orogenic Collage through several localized mapping areas. A multi-disciplinary approach is used to map various geologic formations in detail, including ophiolite melanges, sedimentary basins, thrust sheets, and eclogite exposures (Cleven et al. 2018, van Staal et al. 2019, de Vries 2020, Hong et al. 2022, Santos et al. 2022a). A new tectonic model that proposes the time and location of the final

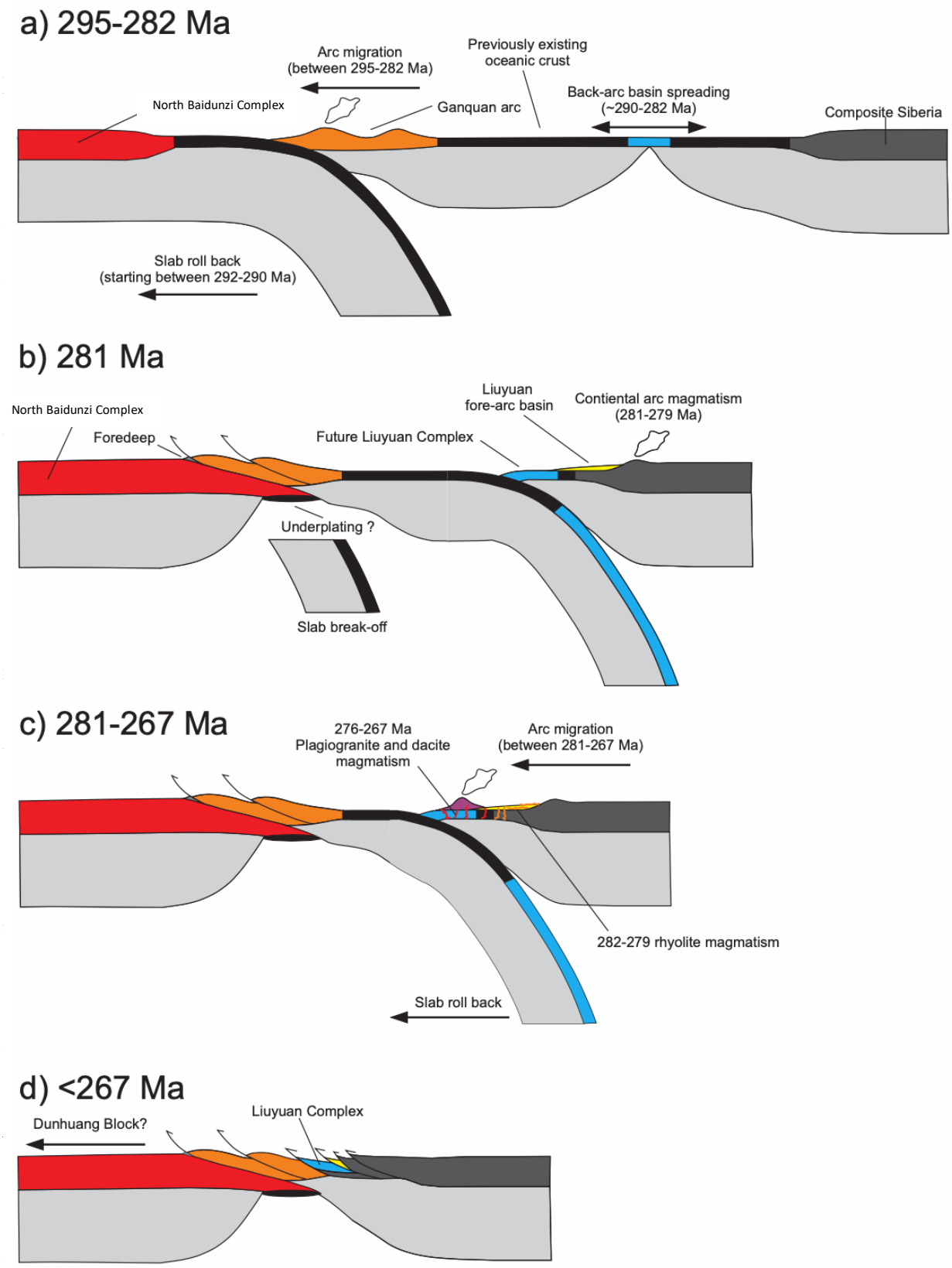

Figure 2: New tectonic model depicting the closure of the Paleo-Asian Ocean and generation of the Liuyuan complex, proposed by Santos et al., (2022).

amphibole orthogneiss, intruded by younger phases of tonalite (ca. 271 Ma), trondhjemite, and granite (van Staal et al. 2019). The border between the North Baidunzi Complex and South Baidunzi Complex is defined by a major shear zone. The rocks in the North Baidunzi Complex are completely different than the rocks found in the South Baidunzi Complex, and therefore these two complexes are interpreted to have different tectonic histories (T. Hong, personal communication, 2021). Available data from the South Baidunzi Complex is very limited and more detailed work, including this thesis, is required to better characterize this unique terrane.

To clarify, the name South Baidunzi Complex is simply a term used to refer to terrane located south of the fault that separates it from the North Baidunzi Complex. It is in no way attempting to interpret a genetic linkage with the North Baidunzi Complex that was characterized by van Staal et al. (2019).

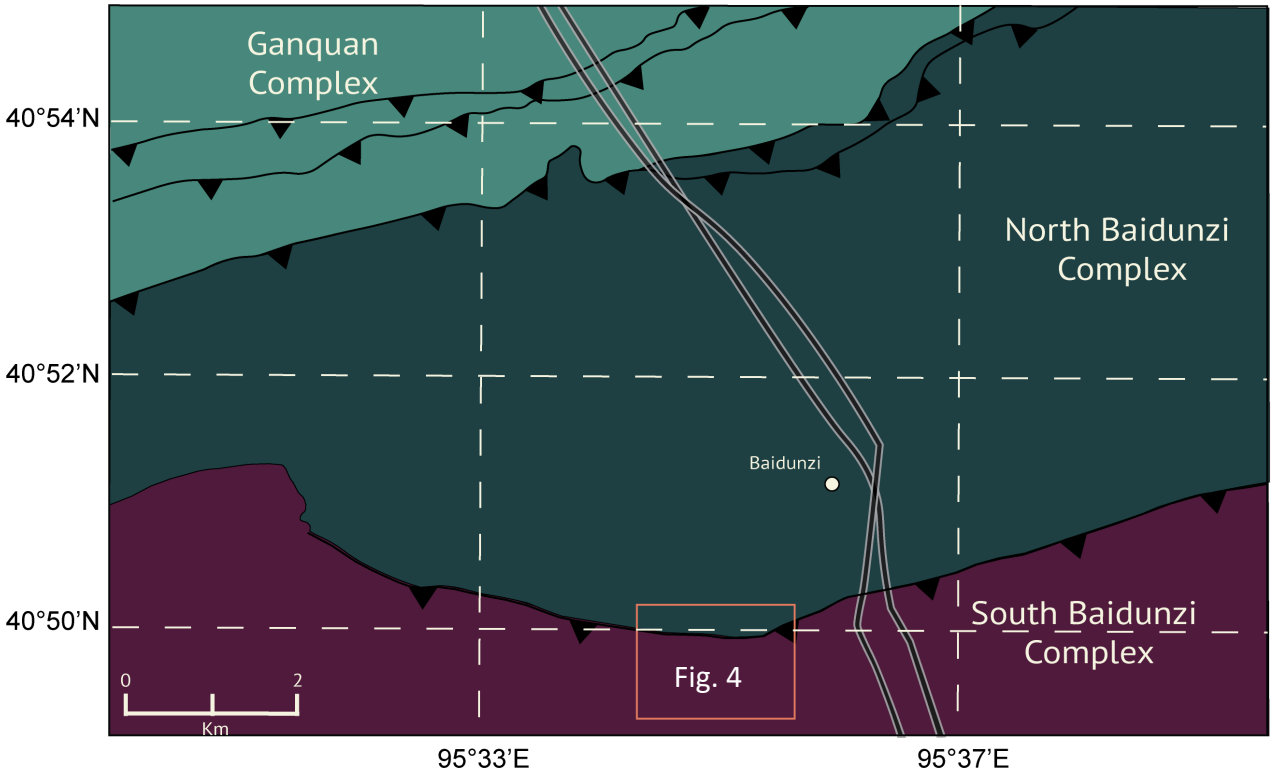

Figure 3: Simplified geologic map showing site locality (orange box). Note the south-dipping thrust fault that seperates the North Baidunzi Complex from the South Baidunzi Complex. Modified from van Staal et al., (2019).

2.3 Dunhuang Orogenic Belt

Rocks in the Dunhuang area were originally thought to be from a stable Precambrian continental block with the basements being the Tarim Craton or the North China Craton (Lu et al. 2008, Xiao et al. 2010, Zhang et al. 2013, Zong et al. 2013, Liu et al. 2015, Zhao et al. 2015). Exposed Precambrian basement rocks are limited and mostly located in central and southern parts of the Dunhuang region, whereas Paleozoic rocks are widespread and numerous, comprising up to 70% of exposed outcrop in the region (Zhao et al. 2016). Recent studies suggest that the Dunhuang Block is not a Precambrian microcontinental block, but rather, comprised of many arc terranes that were accreted via a series of subduction zones during the Paleozoic (Zhang et al. 2013, Zhao et al. 2016, 2017, Wang et al. 2017b, Feng et al. 2020, Shi et al. 2020, Gan et al. 2021). Renaming it as the Dunhuang Orogenic Belt has been proposed, as it is now interpreted to be an orogenic collage that may be associated with the closure of the southern margin of the Paleo-Asian Ocean. (Zhao et al. 2015, 2017, Feng et al. 2020, Shi et al. 2020).

The Dunhuang Orogenic Belt has evidence for at least four tectono-thermal events, with the most recent being in the late Paleozoic-early Mesozoic (Zhao et al. 2016, Feng et al. 2020). Recent research suggests that there were two distinct groups of granitoid rocks: early Permian granite and quartz-granite (284 – 275 Ma) and late Permian to middle Triassic monzogranite (255 – 238 Ma) (Feng et al. 2020). The early Permian rocks are interpreted to have been created from arc subduction-related magmatism from a subducting terrane or the southern margin of the Dunhuang Orogenic Belt (Feng et al. 2020). The late Permian-middle Triassic rocks are interpreted to be post-collisional granites following the assembly of the Beishan or Dunhuang Orogenic Belt (Feng et al. 2020). The final assembly of the Dunhuang Orogenic Belt with its neighbouring terranes is thought to have been in the middle Permian (Feng et al. 2020).

Although the Dunhuang Orogenic belt is located south of the traditional boundary of the Central Asian Orogenic Belt, it shares many similarities with the Beishan Orogenic Collage. Both collages are composed of multiple terranes of different affinities, that share a similar strike-line, that have been accreted and sutured together. The timeline of these two orogens is seemingly continuous, as both orogens have terranes that date from the Silurian to the Permian with some Precambrian microcontinental fragments (Xiao et al. 2010, Mao et al. 2012a, Zong et al. 2012, Song et al. 2013, Zhao et al. 2016, 2017, Feng et al. 2020, Gan et al. 2021, Santos et al. 2022a). Studying the southern corridor of the Beishan is critical in defining the differences between the Beishan Orogenic Collage and the Dunhuang Orogenic Belt, and whether the Dunhuang region is simply a southern extension of the Central Asian Orogenic Belt.

3.0 Field Relationships and Petrography

3.1 Site locality

The Nanquan Quarry pluton is located just south of the steep south-dipping thrust fault that separates the North Baidunzi Complex from the South Baidunzi Complex, and it appears to be confined to the southern side of the fault (Figure 2, 4). It has a slightly ellipsoidal shape, with the E-W semi-major axis measuring approximately 1.5 km and its N-S semi-major axis approximately 0.8 km. The satellite image shows that the pluton is dark grey to black, suggesting it is mesocratic to melanocratic. In the satellite image, the pluton area appears to be the same colour throughout, suggesting it may be composed of a single composition. It is surrounded by garnet-hornblende orthogneiss with lineaments trending E-NE (van Staal et al. 2019).

Twenty samples were collected in or near an abandoned quarry (40.82964861, 95.58719502) (Appendix; Table A1). The quarry has limited fresh outcrop that exposes the cross-cutting relationships between the different rock types. Relationships between lithologies are well preserved in many places. Sampling techniques prioritized collecting a sample suite that was representative of the various lithologies and textures present. The samples collected show all the variations seen at the outcrop, including the different lithologies, varying grain sizes, varying amounts of deformation, and cross-cutting, intrusive, and mingling relationships. All twenty samples were made into thin sections at the Heibei Geology and Mineral Resources Bureau Langfang Laboratory. The thin sections were analyzed using standard transmitted light microscopy.

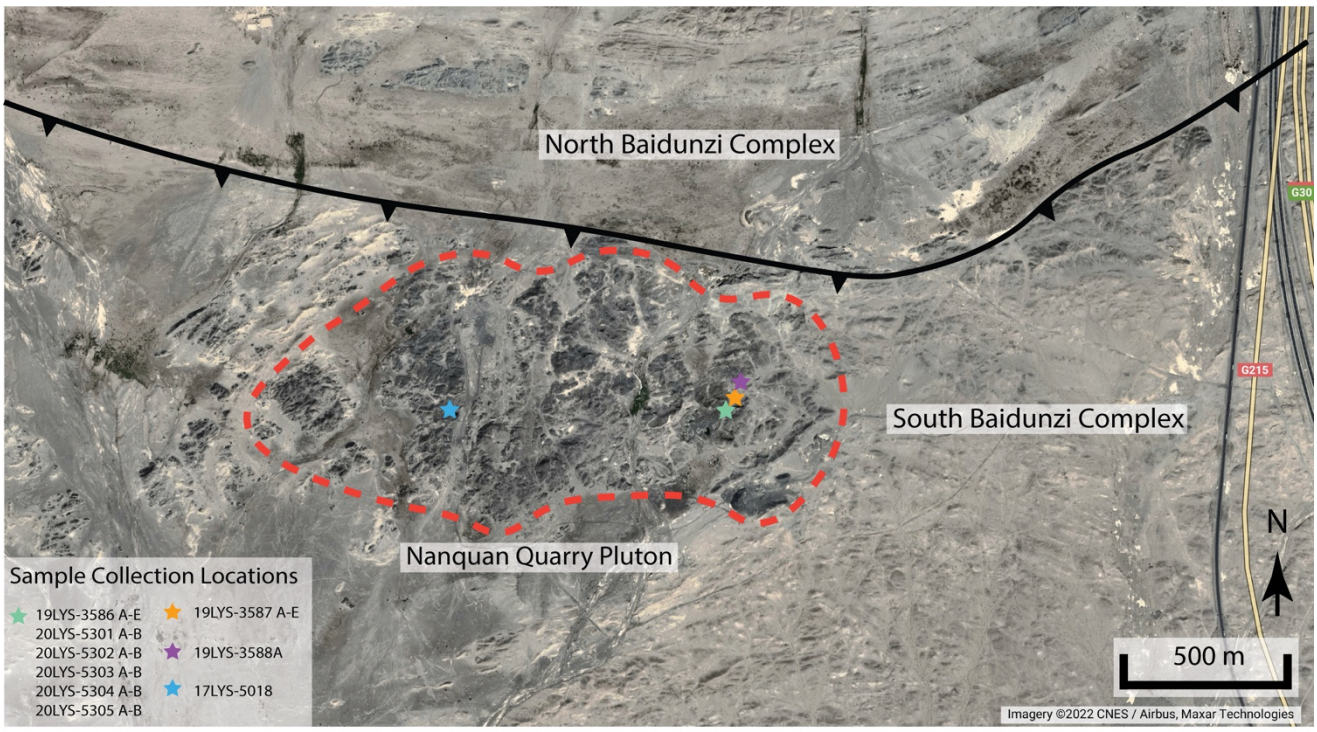

Figure 4: Aerial photo of Nanquan Quarry pluton (circled in red dashed line). Note the thrust fault immediately to the north of the pluton, and the generally E-W lineaments of the garnet-hornblende orthogneiss country rock. Sample collection locations denoted by coloured stars.

3.2 Lithology groups and Field Relationships

The Nanquan Quarry pluton is not homogenous, but rather a mixture of two lithologies: quartz-diorite and quartz-monzodiorite. The rock names have been selected using a quartz-alkali feldspar-plagioclase diagram and are based on the best representation of the modal mineralogy observed in the samples in thin section and hand sample. Both lithologies have varying amounts of deformation, ranging from undeformed to strongly foliated and lineated. At the outcrop scale there is a higher proportion of the quartz-diorite than quartz-monzodiorite. The majority of contacts between these two lithologies are irregular, but both irregular sharp and irregular gradational contacts are present. Types of irregular sharp contacts include net-vein complexes, tube structures, and contacts resembling sedimentary load casts and flame structures (Figure 5A - D). Gradational contacts are less common but show a zone of mixing of the two lithologies (Figure 5E). No defined chill margins are present. The nature of these irregular contacts suggests that both magmas were mush when they interacted. The mingled unit of quartz-diorite and quartz-monzodiorite is crosscut by a granodiorite dike. The dike is undeformed and crosscuts the foliation and lineations in the quartz-diorite (Figure 5F).

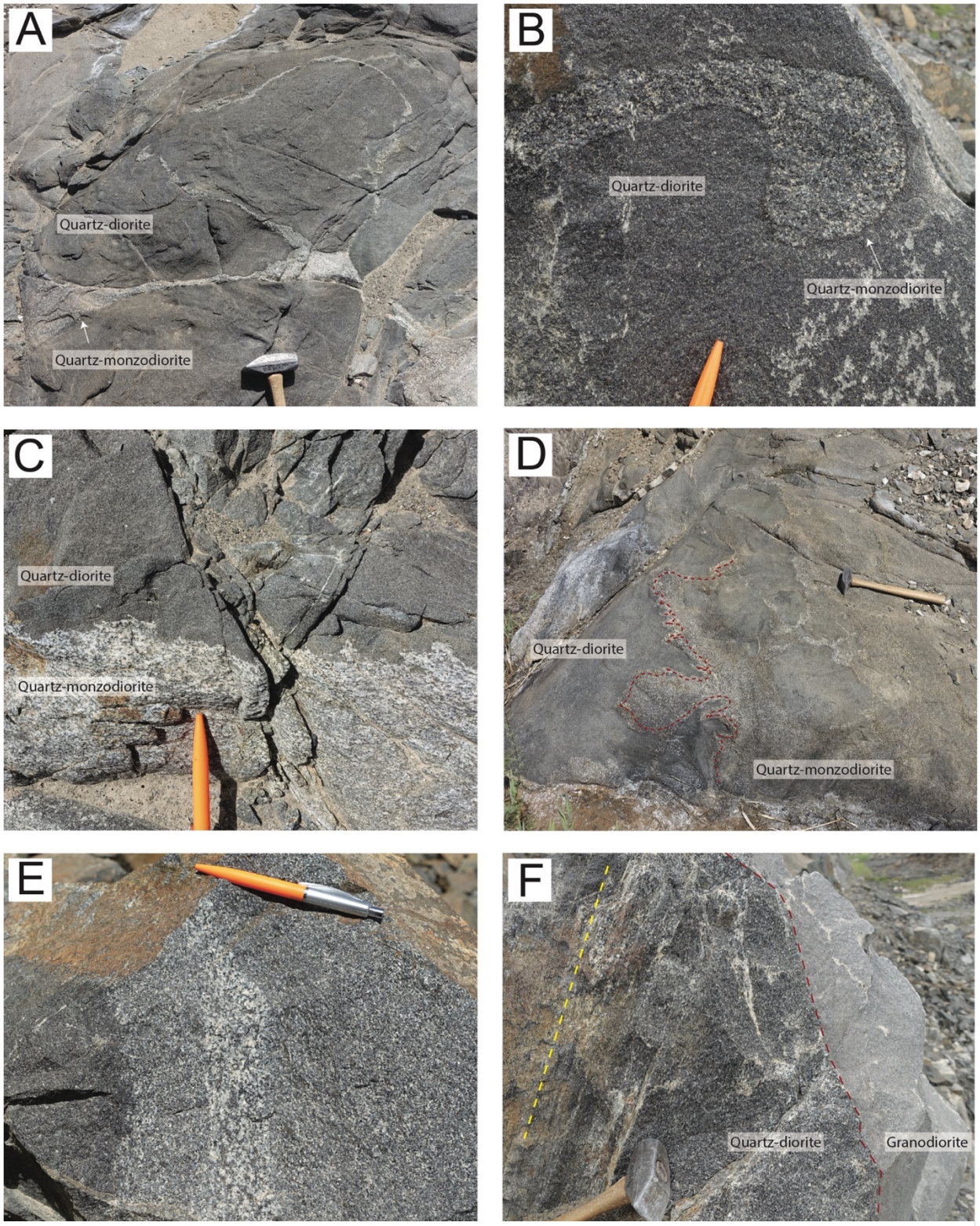

Figure 5: Field relationships: (A) Net-vein texture between quartz-diorite and quartz-monzodiorite. (B) Tube-like structure. (C) Structures resembling load cast structures. (D) Irregular sharp contact between quartz-monzodiorite and quartz-diorite. (E) Gradational contact between quartz-diorite and quartz-monzodiorite. (F) Sharp intrusive contact between lineated quartz-diorite and fine-grained granodiorite. (photos taken by Shoufa Lin)

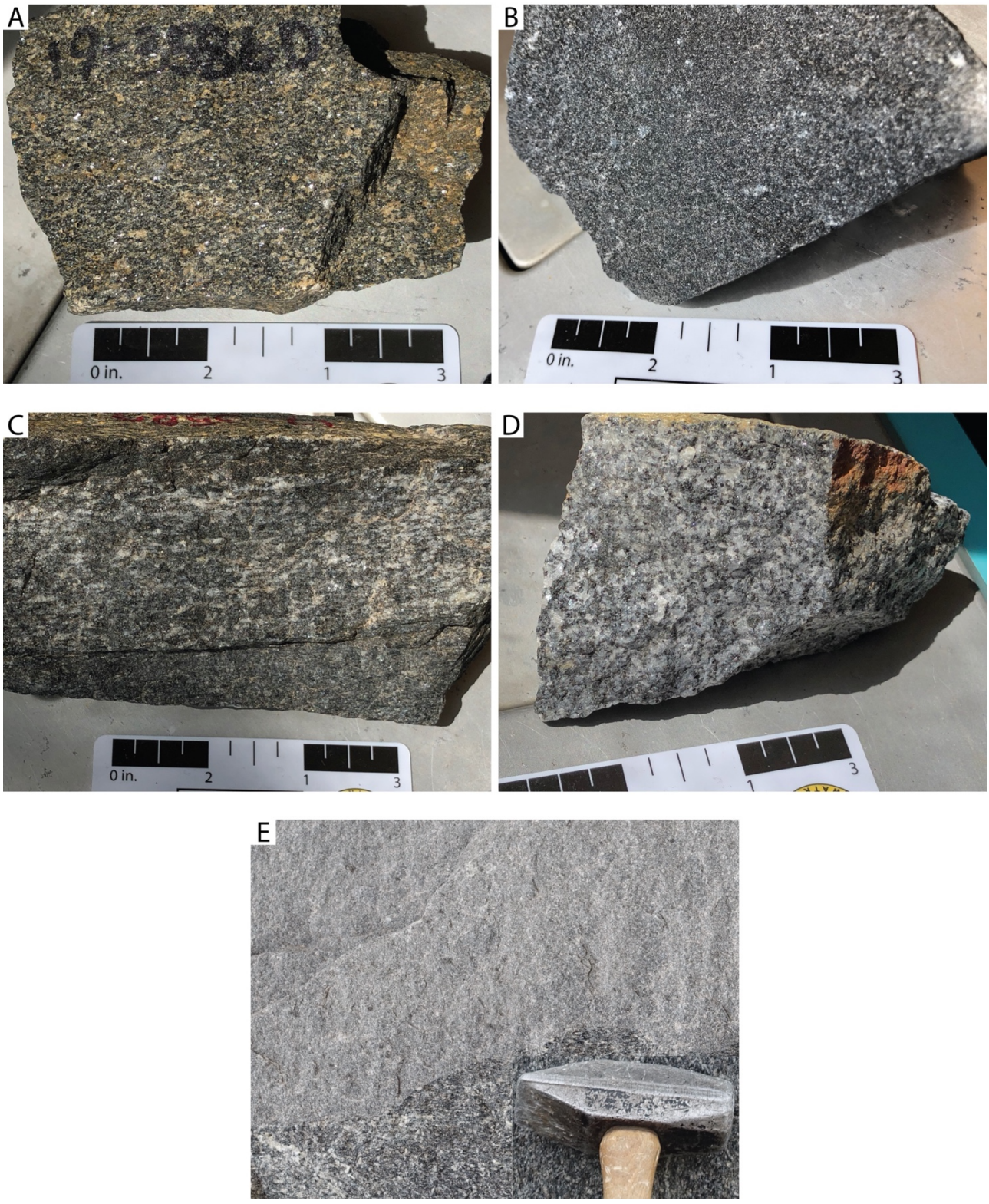

Figure 6: Hand sample photos: (A) Foliated quartz-diorite. (B) Non-foliated quartz-diorite. (C) Foliated quartz-monzodiorite. (D) Non-foliated quartz-monzodiorite. (E) Granodiorite. (photo E was taken by Shoufa Lin)

3.2.1 Quartz-diorite

The quartz-diorite unit is the dominant lithology in the Nanquan Quarry pluton. The thirteen samples that comprise this group are dark grey, fine to coarse grained, and equigranular with a few being porphyritic with plagioclase phenocrysts. This unit has a range of composition with few samples being gabbro to diorite and most samples being quartz-diorite. This group will be referred to as quartz-diorite for brevity. The mineralogy of this group includes of hornblende (20-55%), plagioclase (20-40%), quartz (10-20%), and biotite (5-15%). A few samples had corroded clinopyroxene cores surrounded by a hornblende rim (Figure 7E). Two of these samples also contain olivine grains (less than 5%) (Figure 7D). Accessory minerals include opaque phases + apatite ± zircon ± monazite ± titanite ± rutile. Hornblende is the dominant mafic mineral, and plagioclase is the dominant felsic mineral. The grain sizes vary from fine to coarse, and the texture varies between equigranular hypidiomorphic, inequigranular, and locally porphyritic. The samples with porphyritic texture have very coarse plagioclase phenocrysts with a medium-grained matrix comprised of plagioclase, hornblende, biotite, and quartz (Figure 8C). The amount of deformation varies from undeformed with no foliation to strongly deformed with a well-defined foliation (Figure 7A-B).

Hornblende occurs predominantly as subhedral grains in equigranular and inequigranular samples, and is present in the matrix of porphyritic samples. It also occurs as an interstitial phase associated with cumulate plagioclase grains (Figure 7F). It predominantly has green to brown pleochroism, but a few samples exhibit green to blue pleochroism. A few samples show compositionally zoned hornblende with brown cores and green rims (Figure 7E). Very few samples show alteration of hornblende to tremolite. If the sample has a foliation, the hornblende grains are elongated with the foliation and may wrap around the phenocryst if the sample is porphyritic.

Plagioclase occurs as many different morphologies within this lithology group. Plagioclase occurs as subhedral grains in both equigranular and inequigranular rocks. In porphyritic rocks, plagioclase occurs as coarse subhedral to euhedral phenocrysts and as fine-grained polygonal grains in the matrix (Figure 7C). Coarser grains commonly have inclusions of biotite + opaques ± clinopyroxene ± quartz. Saussurite and/or sericite alteration is widespread, with intensity varying between samples. Small grains of zoisite are also common.

Biotite has pale brown to red-brown pleochroism and forms subhedral to euhedral grains commonly associated with hornblende. Inclusions of zircon in biotite are typical, and biotite also occurs as inclusions in plagioclase grains. A few thin sections show biotite altering to chlorite along the edges of the mineral grain. If the sample has a foliation, biotite grains are elongated along the foliation.

Quartz is anhedral and predominantly occurs as an interstitial phase between other mineral grains. It also occurs as intergrowths with other minerals including hornblende and plagioclase and is also commonly found as small inclusions in these minerals.

In the two samples where olivine is present, the olivine grains are less than 1 mm in diameter and are subhedral. These two samples also have the lowest modal percent of quartz in the rock. Olivine grains are commonly associated with hornblende, plagioclase, and biotite. Hornblende locally forms reaction rims around the olivine grain.

About half of the samples have a small amount of clinopyroxene. It is commonly found as mesh-like pattern or micro-net-vein-like texture with hornblende (Figure 7E). It is also found as remnants of a core that is completely surrounded by a hornblende rim (Figure 7E). Clinopyroxene grains are present as groundmass grains in very few cases. Small clinopyroxene grains are rarely present as inclusions in plagioclase and hornblende grains.

The opaque phase is present in all samples but the amount varies between samples from trace amounts up to 10%. It is potentially a magnesium, iron, or titanium oxide, likely ilmenite. It occurs as lines of small blebs commonly associated with mafic minerals, typically with a highly fractured alteration rim around it. It is also commonly found as small inclusions within plagioclase grains. Zircon and monazite grains are fine and show no preferred mineral associations within the rock. A few zircon grains were euhedral and showed pyramidal terminations. Titanite grains are euhedral to subhedral and are found up to 1 mm in size and are commonly found near aggregates of mafic minerals. Fine euhedral apatite crystals are found throughout the whole thin section and show no preferred association to other minerals.

3.2.2 Quartz-monzodiorite

Five samples make up the quartz-monzodiorite group. They are medium to light grey, medium to coarse grained, inequigranular, and few are porphyritic with plagioclase phenocrysts. Deformation observed in hand sample is either undeformed or strongly deformed (Figure 6C-D). The most prominent texture is inequigranular, with coarse plagioclase grains surrounded by a

fine to medium mosaic-like matrix of plagioclase + quartz + biotite. This unit is composed of plagioclase (40-50%), quartz (20-25%), biotite (10-20%), hornblende (trace-20%), and alkali feldspar (trace-15%). Accessory minerals include opaques + apatite + zircon ± titanite ± rutile ± monazite. Amount of deformation varies from undeformed with no foliation to strongly deformed with a well-defined foliation.

Plagioclase exists as both subhedral coarse grains and in the fine to medium granoblastic matrix. The coarser subhedral grains of plagioclase often exhibit a high amount of saussurite and sericite alteration in the centre of the grain, and a lower amount at the grain boundaries. Zoisite alteration spots are also common. Compositional zoning shown by oscillatory zoning and/or concentric extinction bands are typical.

Quartz has many morphologies in this unit. It is most commonly interstitial grains or medium anhedral to subhedral grains. It is also found as polygonal triple-junction grains or as inclusions and intergrowths with hornblende and/or plagioclase.

Biotite occurs as an interstitial phase between plagioclase and quartz grains. In foliated samples, biotite forms subhedral grains up to 2 mm that align with the foliation. It has light brown to red-brown pleochroism and often contains zircon inclusions.

Hornblende exists either as anhedral grains intergrown with quartz and plagioclase or as an interstitial phase. It has green to brown-green pleochroism and is commonly associated with biotite. Half of the samples in this group have trace amounts of clinopyroxene which are almost always intergrown with or located beside hornblende. The hornblende grains align with the foliation if present.

Half of the samples in this group have a small modal proportion of medium grained microcline grains. The grain boundaries are irregular and embayments of myrmekite texture are often found at the boundary of a plagioclase and microcline grain (Figure 8C).

The opaque phase typically occurs in spotty linear trends, occupying voids along a fracture in the rock, or associated with aggregates of mafic minerals. It is potentially a magnesium, iron, or titanium oxide, likely ilmenite. It has highly fractured alteration rims around the grain and in a few instances, complete replacement has occurred. Small grains that occur at the border between hornblende, biotite, plagioclase, or quartz are typical.

Myrmekite texture is present in all samples of this group. This texture can be found as embayments at the edges of microcline grains, or in parts of the groundmass that are completely

felsic (Figure 8C). This texture is found in areas of the thin section where there is no indication of pressure shadows, suggesting this is texture developed through magmatic processes.

3.2.3 Granodiorite

The two samples that make up the granodiorite group are light grey, fine to medium grained, and lack a foliation (Figure 6E). The main texture is inequigranular with medium grained subhedral plagioclase grains and fine-grained matrix comprised of mostly plagioclase, quartz, and biotite. The main minerals that comprise this unit are plagioclase (40-45%), quartz (30-35%), biotite (15-20%), and microcline (10-15%). Accessory minerals include apatite + zircon + titanite ± rutile ± monazite.

There are two populations of plagioclase: medium grained subhedral grains and fine-grained matrix grains (Figure 9B). Saussurite alteration in the coarser grains is typical, especially in the cores. Sericite alteration is also common, particularly in the finer grained population. Compositionally zoned grains that exhibit concentric extinction are typical (Figure 9B). Microcline grains are typically subhedral, but most edges of the grain became irregular and embayed. Myrmekite texture is abundant, commonly found in little rounded pockets corroding or consuming the microcline grain (Figure 9A). It is also found randomly throughout the groundmass of the rock in areas with abundant quartz and plagioclase. It appears to be produced through magmatic processes, as it is not associated with pressure shadows.

Quartz occurs as subhedral to anhedral grains and is commonly found as inclusions in plagioclase and biotite. It is also found as an interstitial phase, especially between plagioclase grains.

Biotite has pale brown to red-brown pleochroism and occurs as subhedral grains with no preferred orientation. Zircon inclusions are typical.

Trace amounts of hornblende and clinopyroxene are present and are typically associated with biotite. Trace amounts of a magnesium, iron, or titanium oxide opaque phase, likely ilmenite, are present in small blebs throughout the thin section, however most are severely or completely altered. Zircon is abundant and commonly found as inclusions in biotite. Euhedral to subhedral grains of titanite are present, with the coarser grains occasionally having opaque inclusions.

3.3 Deformation textures

The amount of deformation varies between lithology types. Based on the samples collected, the quartz-diorite and quartz-monzodiorite have experienced more deformation than the granodiorite (Figure 6-9). Approximately half of the samples from both the quartz-diorite and quartz-monzodiorite have a foliation defined by biotite and hornblende. The granodiorite samples showed no preferential orientation of minerals.

All samples in the quartz-diorite and quartz-monzodiorite units show signs of dynamic recrystallization in the matrix. Common deformation textures found in plagioclase include undulose extinction, deformation twins, triple junction polygonal grains, and localized bulging recrystallization. Deformation textures in quartz include undulose extinction, triple junction polygonal grains, localized bulging, and sub-grain rotation. The granodiorite samples showed limited undulose extinction and deformation twins in feldspar grains, and undulose extinction with localized bulging in few quartz grains.

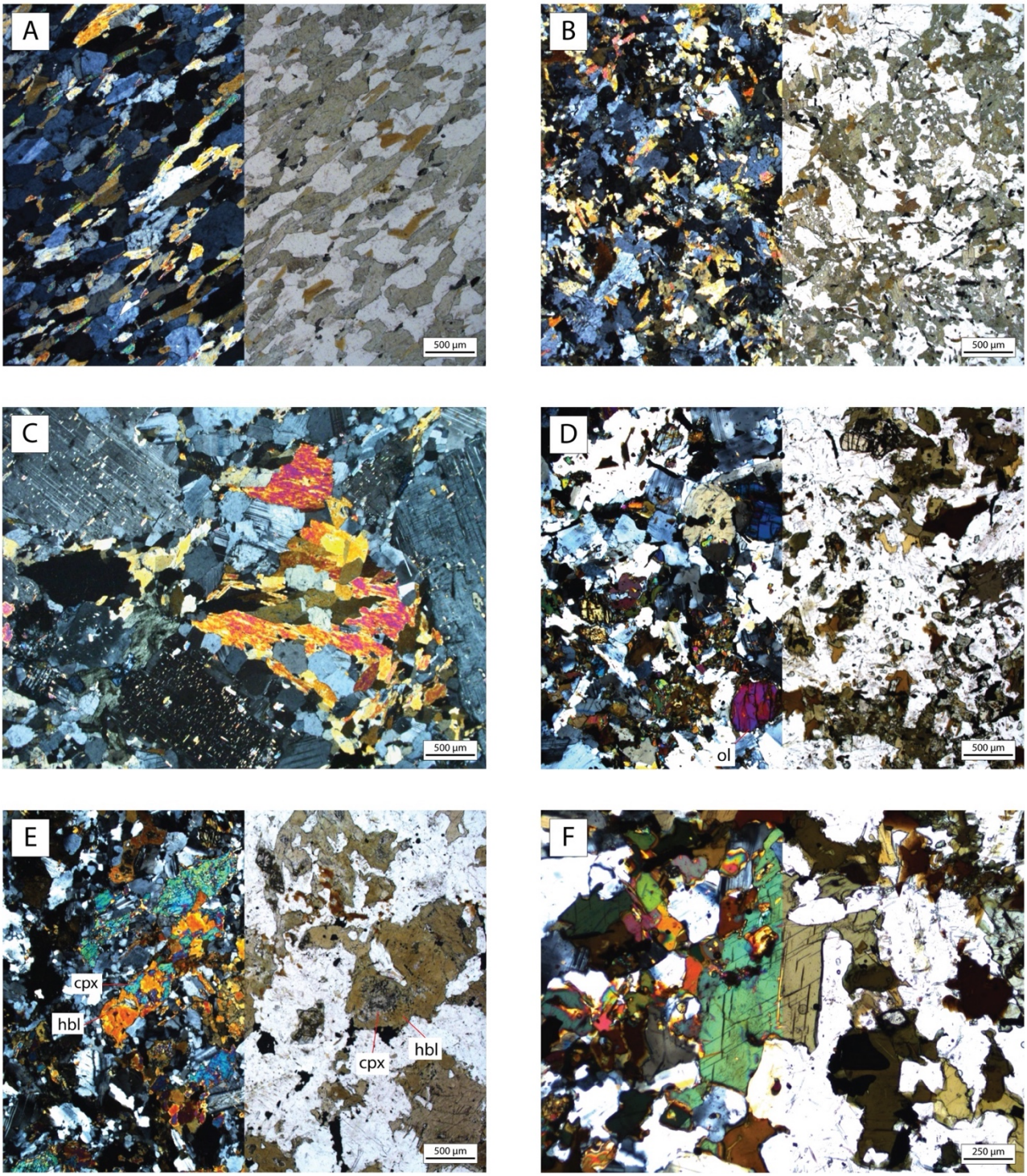

Figure 7: Photomicrographs of quartz-diorite samples: (A)Foliated sample. (B) Non-foliated sample. (C) Porphyritic sample. (D) Olivine grains in sample. (E) Clinopyroxene core surrounded by hornblende rim. (F) Interstitial hornblende.

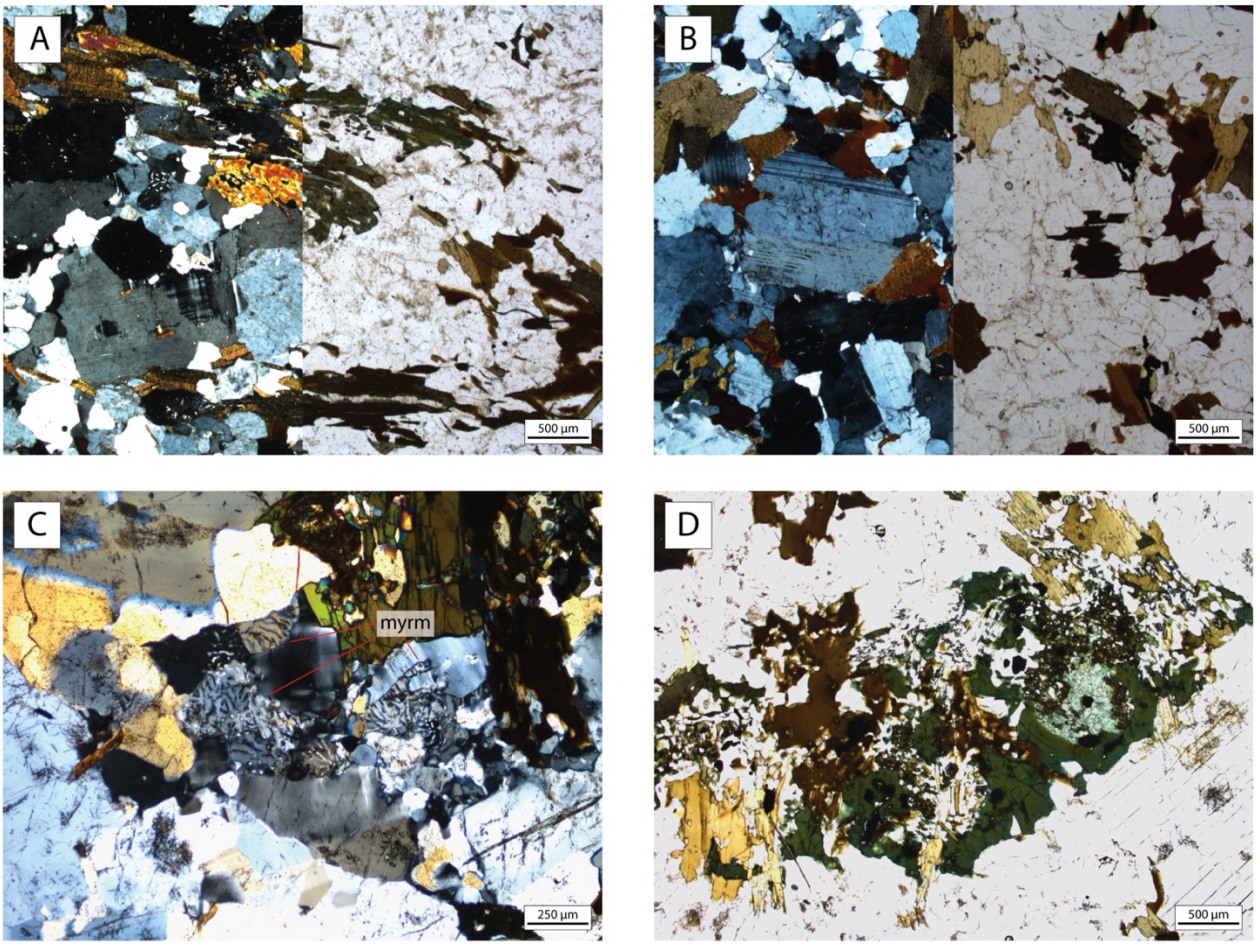

Figure 9: Photomicrographs of quartz-monzodiorite: (A) Weakly foliated, defined by biotite and hornblende. (B) Inequigranular. (C) Myrmekite embayment texture. (D) Quartz intergrown with hornblende and biotite.

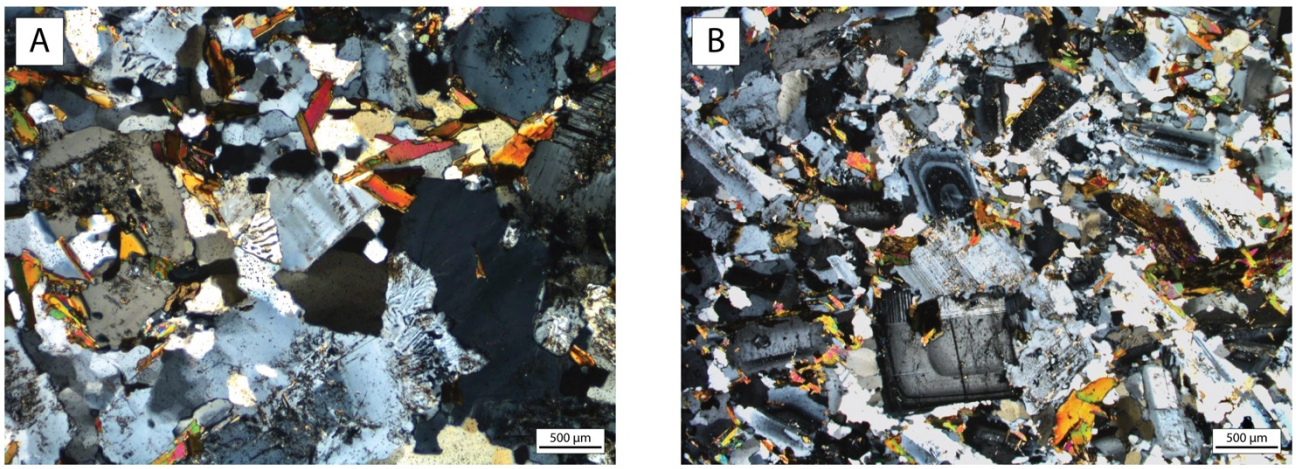

Figure 8: Photomicrographs of granodiorite: (A) Inequigranular with myrmekite texture. (B) Inequigranular with coarse zoned plagioclase.

4.0 U-Pb Geochronology

4.1 Analytical Techniques

U-Th-Pb isotopic data of zircon crystals from each sample were analyzed using the sensitive high-resolution ion microprobe-II (SHRIMP-II) (see Appendix; Table 3-6). Samples were processed at the Beijing SHRIMP Center in the Chinese Academy of Geological Sciences. Zircon grains were separated and mounted in epoxy with chips of TEMORA 1 zircon standard (417 Ma; Black et al. 2003). The epoxy mounts were then polished to expose grain interiors. A cathodoluminescence (CL) system was used to photograph the grains to characterize the domains and avoid complex internal structures. The analytical procedures followed are detailed in Compston et al. 1992, Claoué-Long et al. 1995, Williams 1997, Nelson 1998.

Calibration of U was based on zircon standard M257 (834 ± 15 ppm U; (Nasdala et al. 2008). Interelement fractionation ion emission of zircon was corrected relative to the zircon standard TEMORA 1 (417 Ma; (Black et al. 2003)), which were rerun between every three or four analyses. The analytical routine followed Kröner et al. 2012 and Song et al. (2002) using a 20 μm spot diameter. Many grains had fracturing or inclusions, and these spots were avoided when selecting analysis spots.

Age calculations were performed using the IsoplotRgui v 4.2 (Vermeesch 2018) and Squid programs and the IUGS-recommended decay constants (Steiger and Jäger 1977). The errors of individual analyses and uncertainties in ages are given at 1-sigma level, while the weighted mean age of populations are given at the 95% confidence level. Analytical data are given in the Appendix and plotted on concordia diagrams with 2 sigma ellipses. Concordia diagrams were created using IsoplotRgui v 4.2 (Vermeesch 2018).

4.2 Results

Four samples were collected and dated with SHRIMP, aiming to define the age of each lithology and constrain the timing of magmatism. Complete isotopic data and sample locations are reported in Appendix; Table 2-7. Results from the four samples are summarized here.

High amounts of uranium in the zircon is correlated to high amounts of radiation locked in the crystal structure that can potentially cause damage to it, leading to lead loss, which can

produce an unreliable age (Andersen et al. 2019). One zircon with a core-rim structure from this study (described in detail in section 4.2.1) produced a date for the core that is younger than the date produced for the rim. The core has a high uranium concentration (>900 ppm), and we suspect that this age discrepancy was due to the high uranium concentration in the core. Some other spots with high uranium concentration also yield relatively young apparent dates. As a result, all spots from all samples that yielded a uranium concentration of >900 ppm have been excluded from age calculations.

4.2.1 Sample 20LYS-5304b: Quartz-monzodiorite

Sample 20LYS-5304 is a coarse-grained equigranular quartz-monzodiorite. Zircon grains from this sample are subhedral, relatively equidimensional with an average aspect ratio of 1.5:1, and range in size from 70 to 250 μm. Cathodoluminescence images show dark, unzoned, irregular-shaped cores surrounded by oscillatory zoned rims (Figure 10). A few grains showed irregular fracturing, and small to medium, black, subrounded inclusions are typical.

Fifteen analyses produced a range in $^{206}Pb/^{238}U$ ages from 262 Ma to 274 Ma. One specific zircon hosted two analysed spots: one on the rim (spot 11) and one on the core (spot 12). The spot on the core yielded an age that was younger than the spot on the rim by a difference of 12 Ma, which is inconsistent with the process of crystallizing a core-rim structure. The core spot had very high uranium concentration (943 ppm) relative to the rim (414 ppm). The core spot was excluded from the concordia age calculation due to high uranium concentration and suspected lead loss, along with three other high uranium analyses from the sample. Our best estimation for the age of crystallization is based on a concordant group of eleven zircon grains, yielding a concordia age of 269 ± 2 Ma (MSWD = 1.1) (Figure 11C).

4.2.2 Sample 17LYS-5018: Quartz-diorite

Sample 17LYS-5018 is a fine to medium-grained equigranular quartz-diorite. Zircon grains in this sample are subhedral with an aspect ratio of about 1.75:1, ranging in size from 75 to 300 μm. Cathodoluminescence images revealed that many grains had dark non-zoned cores with irregular boundaries, surrounded by an oscillatory zoned rim (Figure 10). Most grains had one or more small to medium, subrounded, black inclusions. A few grains had pyramidal terminations.

Fifteen spot analyses produced a range in $^{206}Pb/^{238}U$ ages from 266 Ma to 285 Ma. One spot has been excluded from the concordia age calculation because it was an outlier with an age of 286 ± 5 Ma. The remaining fourteen spots yielded a concordia age of 270 ± 3 Ma (MSWD = 0.92) (Figure 12C). This age is the best estimate for the crystallization age of this quartz-diorite sample.

4.2.3 Sample 20LYS-5301b: Quartz-diorite

Sample 20LYS-5301b is a weakly foliated medium-grained porphyritic quartz-diorite. Zircon grains in this sample display similar morphology to those of 17LYS-5018. The grains were subhedral, relatively equidimensional with an aspect ratio of 1.5:1, and range in size from 75 to 375 μm. Cathodoluminescence images revealed that many grains had a dark unzoned core with irregular edges, surrounded by an oscillatory zoned rim (Figure 10). A few grains showed minor fracturing and small to medium, black, subrounded inclusions are widespread.

Fifteen spot analyses showed a range in $^{206}Pb/^{238}U$ ages from 225 Ma to 284 Ma. Three spots were excluded from the concordia age calculation as they were outliers with ages 285 ± 4 Ma, 261 ± 4 Ma, and 225 ± 10 Ma. Two spots were excluded from the age calculation due to high uranium. The remaining ten spots yielded a concordia age of 273 ± 2 Ma (MSWD = 1) (Figure 13C). This is the best estimate for the crystallization age of this quartz-diorite sample.

4.2.4 Sample 20LYS-5302b: Granodiorite

Sample 20LYS-5302 is from a medium grained equigranular granodiorite dike. It was collected from the same outcrop as the quartz-diorite sample 20LYS-5301, where the granodiorite dike intrudes the quartz-diorite (Figure 5F). The zircon grains in this sample show two different morphologies. One group of grains, hereon referred to as Group I, display subhedral to euhedral grains ranging in size from 25 to 130 μm, with an aspect ratio of 4.5:1. Cathodoluminescence images reveal continuous oscillatory zoning from the centre to the edge of the grain, with most grains showing pyramidal terminations (Figure 10). The zircons in this population lack fracturing and are generally free of inclusions. The second group of grains, referred to as Group II, are subhedral with a range in size from 20 to 150 μm. The grains have an aspect ratio of 1.75:1. Cathodoluminescence images reveal dark, unzoned cores with irregular edges, surrounded by an oscillatory zoned rim. A few of the grains showed fracturing and many

of them contained small to medium, black, subrounded inclusions. Group II zircon grains appear similar to those from sample 17LYS-5018, 20LYS-5301, or 20LYS-5304. Group I zircon grains are more abundant than Group II.

In Group I, ten analyses produced a range in $^{206}Pb/^{238}U$ ages from 221 Ma to 278 Ma. One analysis has been excluded from the concordia calculation because it was an outlier with an age of 278 ± 4 Ma. The remaining nine analyses in this group yield a concordia age of 262 ± 3 Ma (MSWD = 1.6, n=9/10) (Figure 14D). This population is interpreted to be the best estimate for crystallization age of the granodiorite intrusion.

In Group II, five analyses produced a range in $^{206}Pb/^{238}U$ ages from 263 Ma to 284 Ma. They yield a concordia age of 270 ± 3 Ma (MSWD = 1.4, n=5/5) (Figure 14C). This age is identical within error to the ages of the quartz-diorite described above, and the population is interpreted to be inherited from the quartz-diorite (sample 20LYS-5301) intruded by the granodiorite dike. This interpretation is supported by the similar zircon morphology between the two samples.

4.3 Comparing core and rim ages

The zircon morphology for sample 5301 (quartz-diorite) and 5304 (quartz-monzodiorite) are very similar to one another. Both samples have zircons with low aspect ratios that show dark cores with irregular boundaries surrounded by a magmatic crystallization rim. These two rock types are interpreted to have been produced during the same magmatic event due to matching unique zircon morphology and magma mingling field relationships.

To determine if the core and rim were crystallized during different events, the data collected from core spots were plotted separately from the data collected from the rims for each sample. As seen in Figure 15, the data from the cores cannot be statistically separated from the rims. Therefore, the cores and the rims are interpreted to have been crystallized during the same magmatic event. As such, the crystallization age for each sample was determined based on all the collected data. Cathodoluminescence images show that the edges of the cores have been resorbed and new zircon was crystallized around the core. Although there is no statistical difference in age, there is still evidence for different stages of crystallization during this magmatic event.

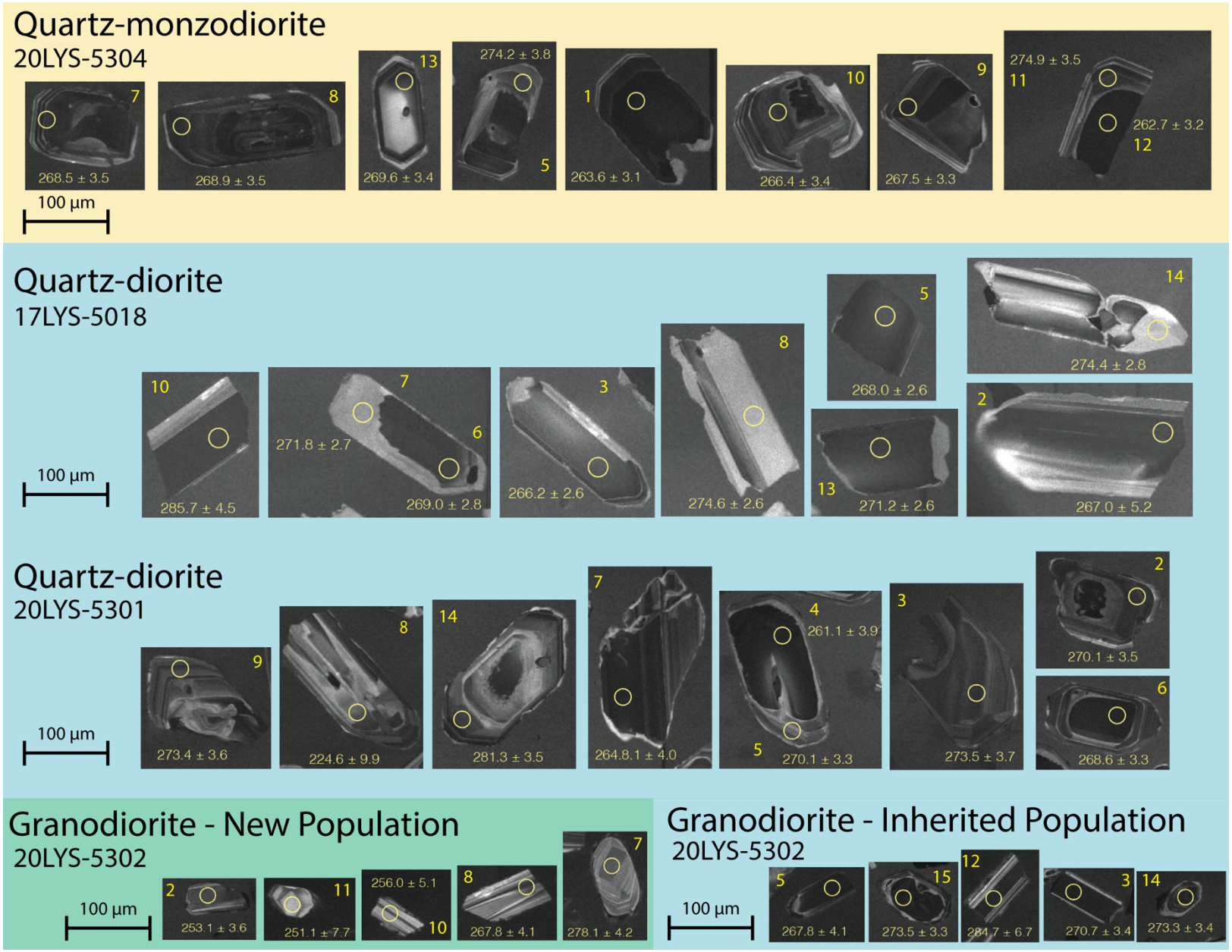

Figure 10: Cathodoluminescence photographs of representative zircon grains from each dated sample. Yellow circle denotes analysis location and the calculated age is beside each analysis spot. Zircon grains from the quartz-monzodiorite sample are in the yellow rectangle, zircon grains from the quartz-diorite samples (directly from or inherited) are in the blue rectangle, and zircon grains from the granodiorite are in the green rectangle.

Quartz-monzodiorite

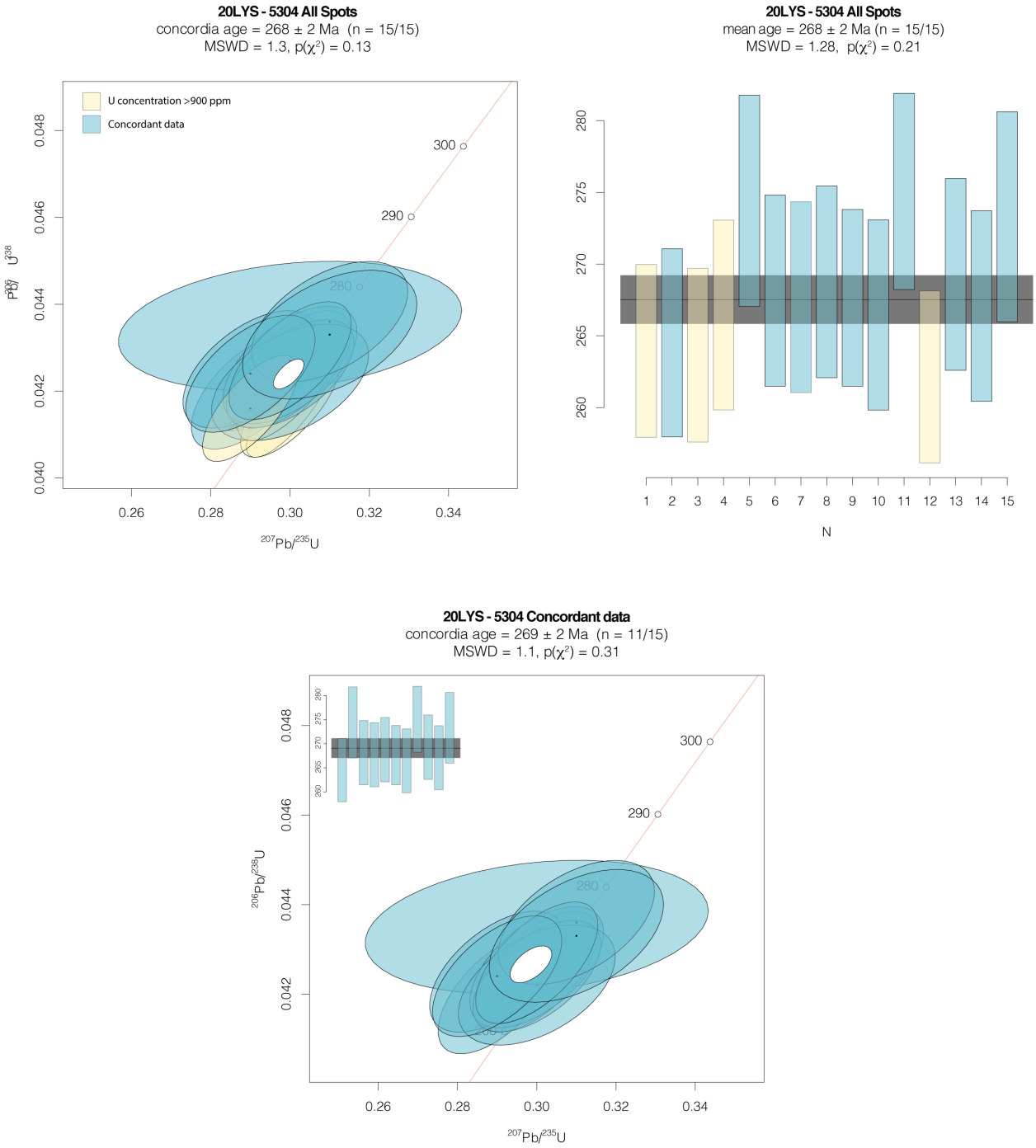

Figure 11: Geochronological data for sample 20LYS-5304 (quartz-monzodiorite). Wetherill Concordia diagram, where blue ellipses are included in age calculation and yellow ellipses are excluded due to high uranium. (A) Data from all spots. (B) Weighted mean. (C) Concordant data, excluding outliers.

Quartz-diorite

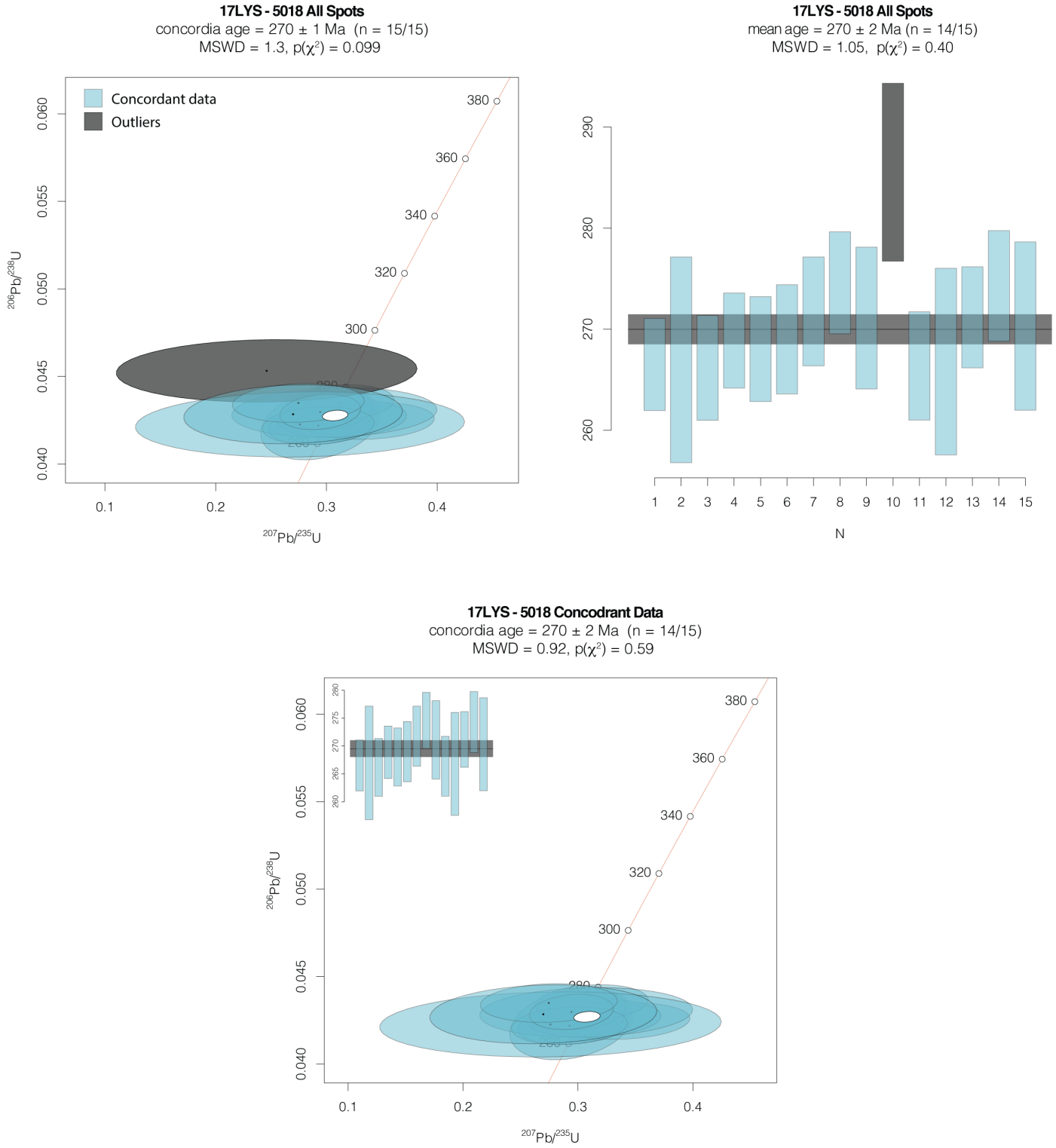

Figure 12: Geochronological data for sample 17LYS-5018 (quartz-diorite). Wetherill Concordia diagram, where blue ellipses are included in age calculation and yellow or grey ellipses are excluded due to high uranium and being outliers, respectively. (A) Data from all spots. (B) Weighted mean. (C) Concordant data, excluded outliers.

Quartz-diorite

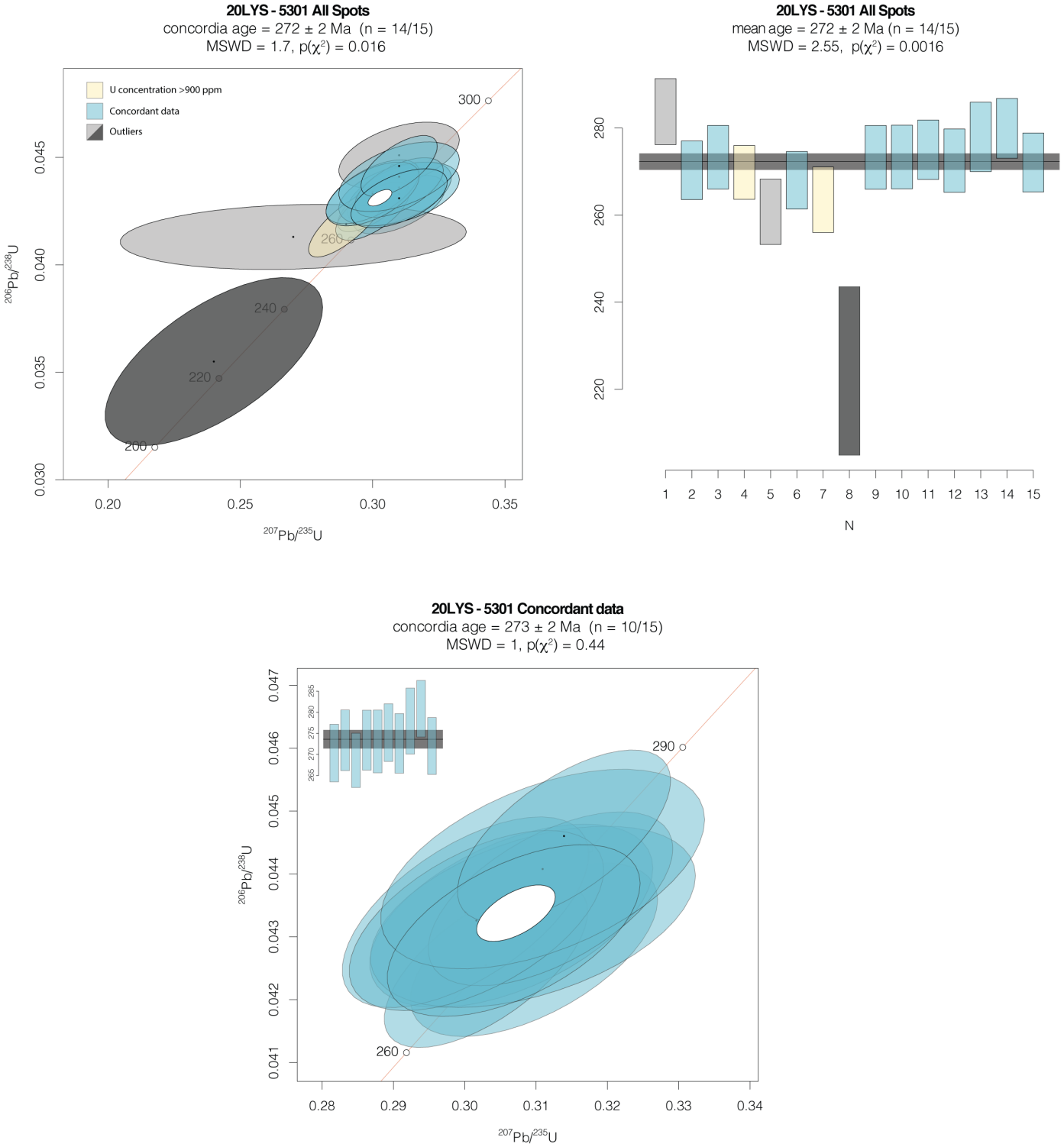

Figure 13: Geochronological data for sample 20LYS-5301 (quartz-diorite). Wetherill Concordia diagram, where blue ellipses are included in age calculation and yellow or grey ellipses are excluded due to high uranium and being outliers, respectively. (A) Data from all spots. (B) Weighted mean. (C) Concordant data, excluded outliers.

Granodiorite

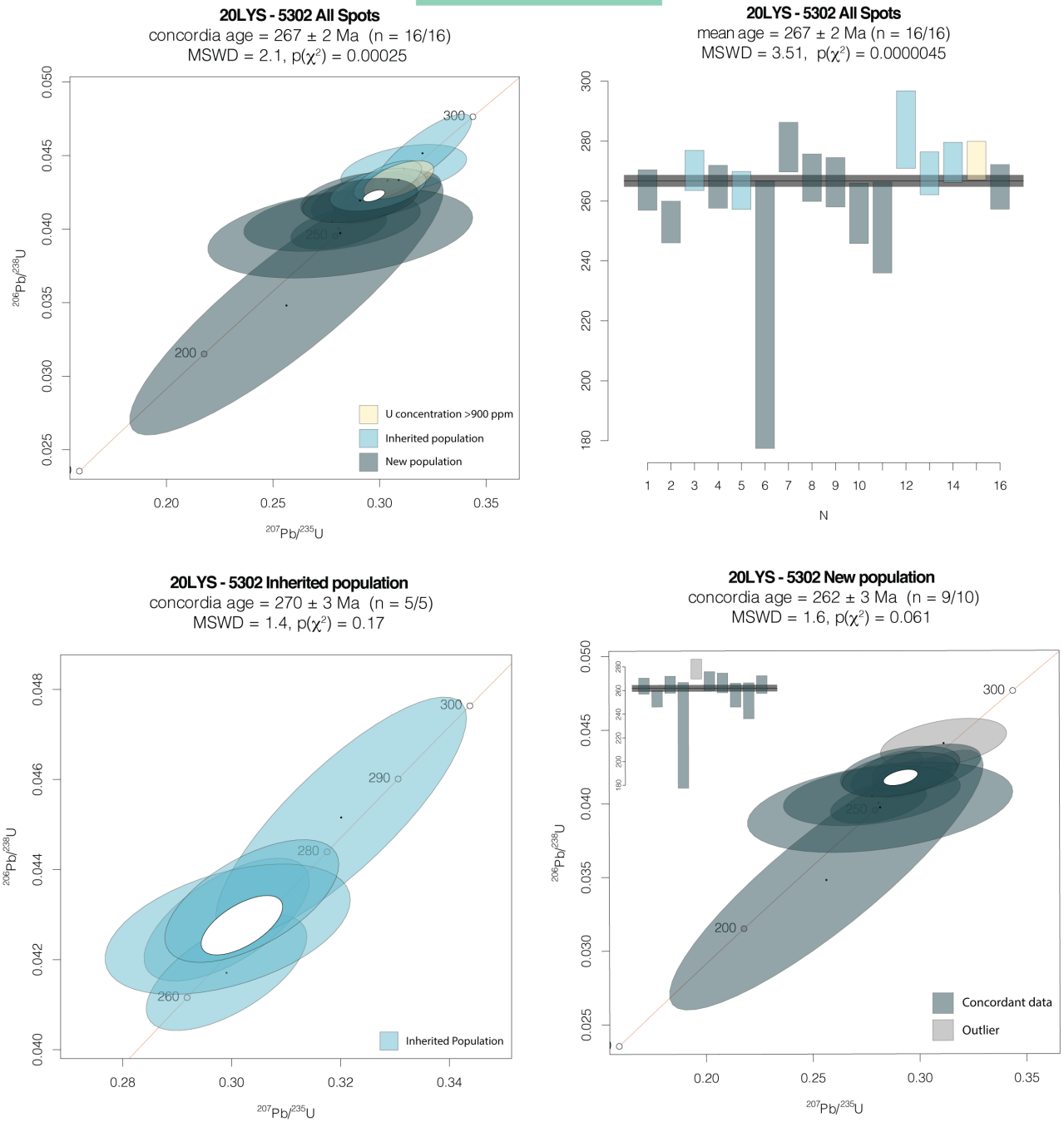

Figure 14: Geochronological data for sample 20LYS-5302 (granodiorite). Wetherill Concordia diagram, where blue ellipses are included in age calculation and yellow or grey ellipses are excluded due to high uranium or being outliers, respectively. (A) Data from all spots. (B) Weighted mean. (C) Concordant data for inherited population, excluded outliers. (D) Concordant data for new younger population, excluded outliers.

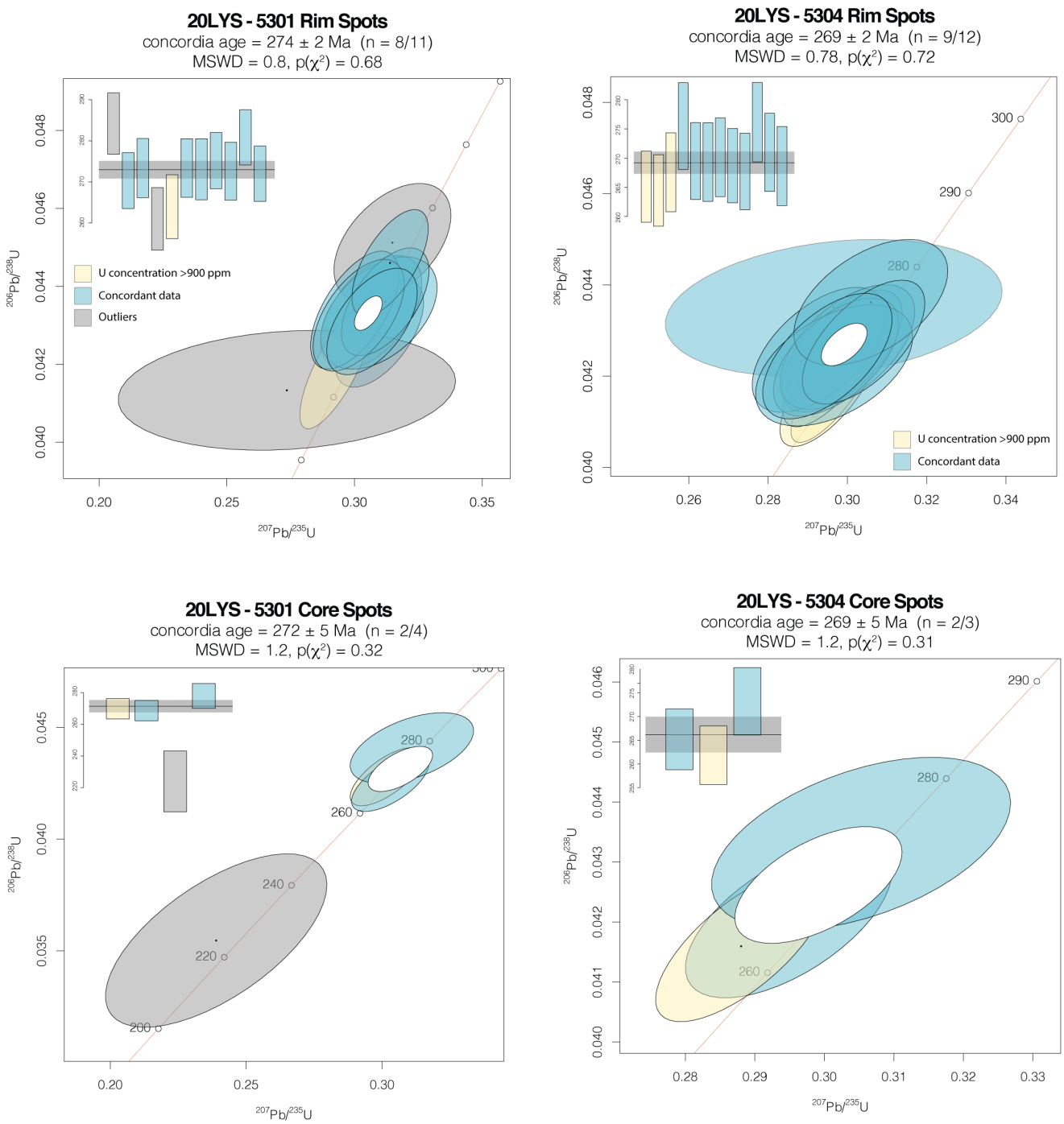

Figure 15: Concordia diagrams comparing the core ages with rim ages, where yellow and grey ellipses have been excluded from the concordia calculation due to high uranium and being outliers, respectively. 20LYS-5301 is a quartz-diorite sample and 20LYS-5304 is a quartz-monzodiorite sample. (A) Concordant from rim spots from 20LYS-5301. (B) Concordant from rim spots from 20LYS-5304. (C) Concordant from core spots from 20LYS-5301. (D) Concordant from core spots from 20LYS-5304

4.4 Timeline Summary

The pluton mainly consists of quartz-diorite and quartz-monzodiorite. The range of crystallization age (including uncertainty) for this intrusion is from 276 Ma to 267 Ma. The granodiorite dike intrudes into the pluton. It has a crystallization age (including uncertainty) from 265 Ma to 259 Ma. Based on the available data, the quartz-diorite and quartz-monzodiorite magmatism ceased before the granodiorite magmatism commenced (Figure 16).

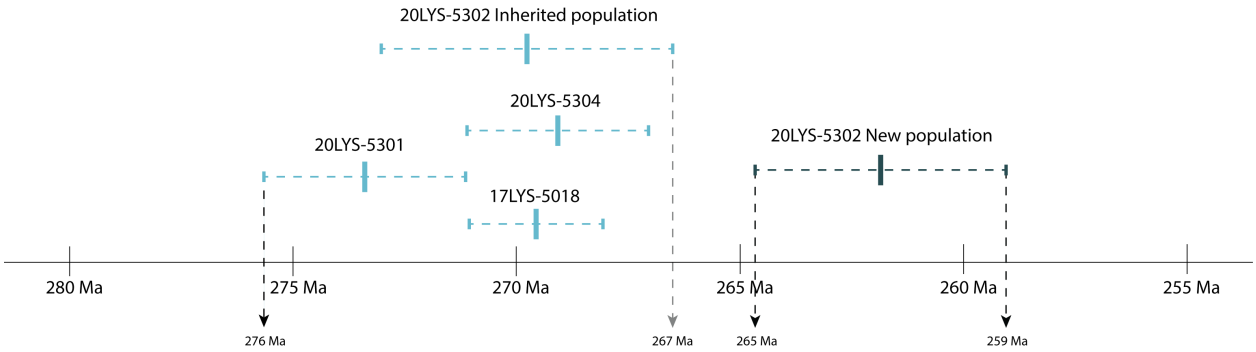

Figure 16: Timeline showing the relative ages of zircon populations from all dated samples. The mingled quartz-diorite, quartz-monzodiorite, and inherited zircons suggest the pluton formed between ca. 275 and 266 Ma, while the granodiorite intruded ca. 261 Ma.

5.0 Geochemistry

Whole-rock chemical data are available for all 20 samples discussed in this study. The most numerous sample lithology is quartz-diorite (n=13), followed by quartz-monzodiorite (n=5), and finally granodiorite (n=2). This chapter provides a description of the major, trace, and rare-earth elements for each lithology group and a brief discussion of their implications. A full report of all chemical data is available in the Appendix; Table 8.

5.1 Analytical Techniques

A total of 20 samples were sent to ALS Chemex Co. Ltd. in Guangzhou, China for geochemical analysis. The samples were processed and analyzed for major, trace, and REE elements using inductively coupled plasma – mass spectrometry (ICP-MS) and inductively coupled plasma – atomic emission spectroscopy (ICP-AES).

Each sample was crushed until ≥ 70% would pass through a 2 mm sieve. A portion of the crushed material was then pulverized until ≥ 85% would pass through a 75 µm sieve. The pulverized samples were then mixed with a lithium borate flux and heated to 1000 °C in an inert crucible to fuse a homogenous product. The sample was then digested in an aqua regia solution before ICP analysis. For quality control, randomly selected samples ran as pulp duplicates to verify the quality of the output data. For quality assurance, international standards and blanks were used to monitor the quality of the process. No problems were detected in the analytical procedure or results. Based on the analysis of these measures, the geochemical data used in this thesis is considered fit for purpose.

5.2 Normative Mineralogy

The CIPW normative mineralogy was calculated and plotted on a QAP classification diagram (Figure 17). All samples plotted in fields near the plagioclase corner. These four fields in the plagioclase corner of the QAP diagram normally have two or more rock types in the same field: one is gabbro, or a derivative of; and the other is a diorite, or a derivative of. Based on the modal mineralogy seen in thin section and hand sample (abundance of hornblende + plagioclase + quartz, and absence of pyroxene), diorite derivatives have been selected as a more representative name for the samples. The geochemical normative names are fairly consistent with the names given based on modal mineralogy.

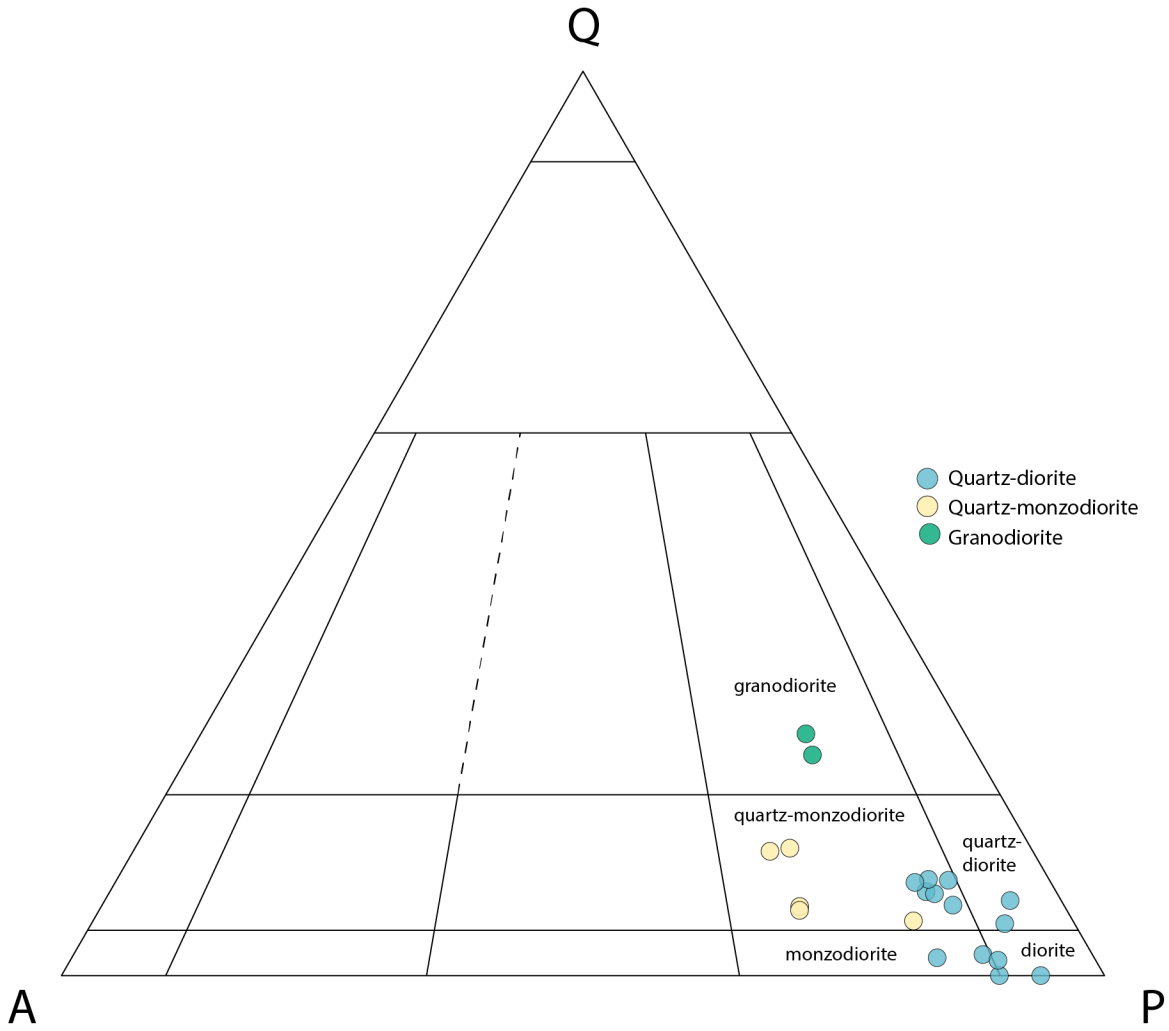

Figure 17: CIPW Normative mineralogy QAP plot. This plot was created using geochemical data, not based on mineral percentages viewed in thin section.

5.3 Major Element Oxides

Silica values for all samples range between 48 and 68 wt%. The quartz-diorite samples had the lowest SiO_2 values, ranging between 48 and 54 wt%. Quartz-monzodiorite had moderate silica abundance, ranging from 58 to 62 wt%. The granodiorite samples are characterized by highest amount of silica, about 66 to 68 wt%. Increasing silica values between lithology groups corresponds to the increasing modal felsic mineralogy.

There is no apparent correlation between alumina and silica. There is very little variation in amount of Al_2O_3 between sample groups. The quartz-diorite samples have the highest amount of variation, ranging from 14.39 to 21.3 wt%. Quartz-monzodiorite samples have the highest average, ranging from 16.29 to 19.05 wt%, and the granodiorite samples are 15.89 to 16.36 wt%. This relationship could relate to modal abundance of biotite, which is fairly consistent throughout all the samples.

CaO shows a negative correlation with silica. Concentrations are highest in the quartz-diorite samples, varying from 7.35 to 11.1 CaO wt%. The quartz-monzodiorite and granodiorite are much lower at 3.05 to 3.9 wt% and 3.33 to 3.61 wt%, respectively. Na_2O has a positive correlation with silica. Abundance in the quartz-diorite samples ranges from 3.13 to 4.37 wt%, and the quartz-monzodiorite samples range from 4.63 5.86 wt%. The concentration in the granodiorite unit is 4.4 wt%. Like Na_2O, there is a positive correlation of K_2O with silica abundance, excluding the granodiorite samples. The lowest amount of K_2O is found in the quartz-diorite samples, with values ranging from 0.53 to 1.47 wt%, whereas the highest amount is found in the quartz-monzodiorite with values of 2.24 to 3.85 wt%. The granodiorite samples range from 2.35 to 2.41 wt%. These relationships correspond to the proportion of plagioclase and alkali feldspar between each lithology. Higher proportions of plagioclase are found in the quartz-diorite and quartz-monzodiorite, where alkali feldspar abundance is minimal. In the granodiorite, however, there is a higher amount of alkali feldspar in addition to plagioclase. These rocks have experienced greenschist facies alteration, and therefore potassium and sodium may have been mobilized and concentrations may not be reliable.

MgO shows a negative correlation with silica abundance. The quartz-diorite unit has significantly higher MgO than the other two groups, ranging from 3.88 to 6.84 wt%. The higher concentrations likely correlate to higher abundance of hornblende and biotite. The quartz-

monzodiorite and granodiorite samples have much lower values of 1.28 to 1.62 wt% and 1.28 to 1.59 wt%, respectively. This lower MgO value is consistent with the lower abundance of hornblende and biotite found in these samples. Total iron, expressed as Fe_2O_3 also has a negative correlation with silica. It ranges from 3.3 to 13.5 wt%, with the highest concentration in the quartz-diorite (6.76 to 13.25 wt%), followed by quartz-monzodiorite (5.57 to 7.93 wt%), and finally the granodiorite samples (3.3 to 3.5 wt%). Fe_2O_3 uniformly decreases between lithology groups, which corresponds to a gradual modal decrease in mafic minerals and oxides.

Like MgO and Fe_2O_3, MnO has a negative correlation with silica abundance. Quartz-diorite samples had the highest concentrations, ranging from 0.11 to 0.21 wt%, followed by quartz-monzodiorite at 0.06 to 0.13 wt%, and finally granodiorite at 0.05 wt%. The decrease in MnO as the lithologic units become more felsic corresponds with the decrease in modal abundance of mafic minerals and oxides.

TiO_2 has a negative correlation with silica. In the quartz-diorite samples, TiO_2 values vary from 1.15 to 2.87 wt%. This is higher than the values of the quartz-monzodiorite at 0.92 to 1.1 wt% and the granodiorite at 0.6 to 0.68 wt%. This decreasing trend is consistent with the higher abundance of Fe-Ti oxide observed in the quartz-diorite, compared with the lower abundance in the quartz-monzodiorite and granodiorite.

Phosphorous does not appear to have a correlation with silica abundance, however the quartz-diorite samples show the most variation in amount of P_2O_5, ranging from 0.15 to 0.36 wt%. Although comparable to one another, granodiorite samples have slightly higher amounts at 0.18 to 0.20 wt%, than the quartz-monzodiorite samples at 0.13 to 0.17 wt%. Apatite is plentiful in all the samples, but highest abundance is typically in the quartz-diorite samples.

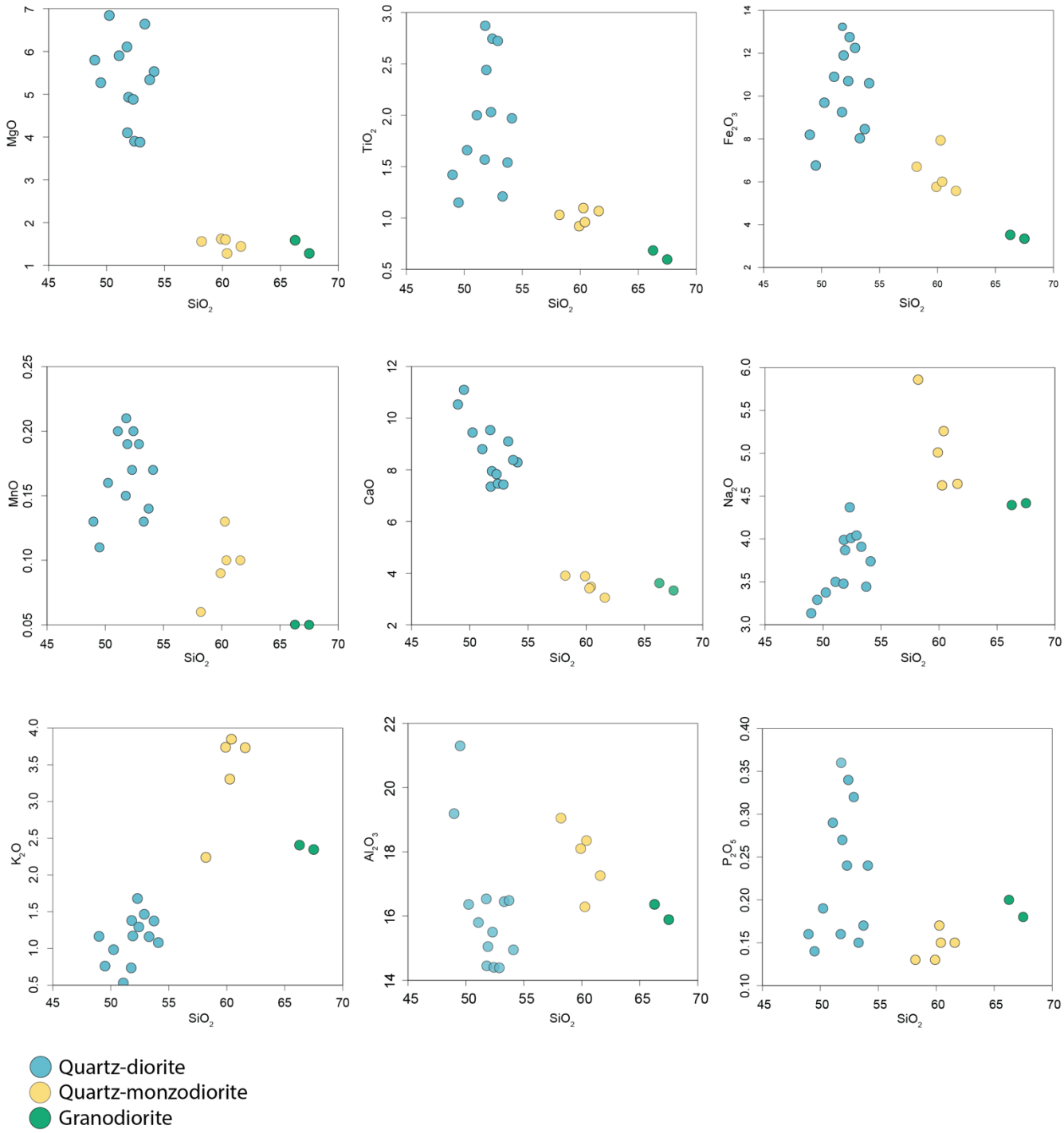

Figure 18: Major Element Harker plots for all samples

5.4 Trace Elements

Similar to the major oxides, trace elements that partition into mafic minerals show a negative correlation with SiO_2. Scandium concentrations are highest in the quartz-diorite samples at 16 to 36 ppm, followed by quartz-monzodiorite and granodiorite at 6.0 to 18.2 ppm and 6.37 to 7.26 ppm, respectively. This trend correlates to hornblende and clinopyroxene abundance, in which Sc is commonly associated. Yttrium and samarium also are taken in by hornblende and follow similar trends to one another; negative correlations with silica, with concentrations overlapping among different lithologies. The quartz-diorite group has Y and Sm concentrations of 21 to 58 ppm and 3 to 10 ppm, respectively. Quartz-monzodiorite samples have a Y concentration of 22 to 41 ppm and Sm concentrations of 5 to 8 ppm. The granodiorite samples have an average Y and Sm concentration of 10.31ppm and 3.58 ppm, respectively.

Many trace elements show a positive correlation between the quartz-diorite and quartz-monzodiorite, but the granodiorite does not follow this trend. Zirconium has a positive correlation with silica abundance between the quartz-diorite and quartz-monzodiorite. The former samples are much lower ranging from 92 to 327 ppm, whereas the latter samples are much higher ranging from 514 to 728 ppm. The concentration in the granodiorite samples range from 219 to 235 ppm and do not lie on trend with the other lithologies. Uranium concentrations follow a similar trend with higher concentrations in the quartz-monzodiorite than that of quartz-diorite, 1.24 to 1.93 ppm and 0.38 to 0.97, respectively. Granodiorite samples have U concentrations of 1.38 to 1.42 ppm. Thorium has a positive correlation with silica abundance, with the highest concentration in the granodiorite, followed by the quartz-monzodiorite, and finally the quartz-diorite.

Rubidium shows a positive correlation with silica abundance. The quartz-diorite samples range from 10 to 45 ppm, quartz-monzodiorite ranges from 39 to 54 ppm, and the granodiorite samples average at 57 ppm. Strontium shows the opposite with a negative correlation with silica abundance. Sr concentration ranges in the quartz-diorite samples from 221 to 358 ppm and the quartz-monzodiorite samples range from 203 to 250 ppm. The granodiorites, however, have almost twice as much Sr, with values of 452 to 485 ppm. Rubidium commonly substitutes into alkali feldspars and strontium substitutes into plagioclase. Comparing these two elements can indicate the relative proportion of these two minerals in the samples, as the ratio Rb/Sr is

sensitive to modal proportions. The Rb/Sr ratio shows a positive correlation with silica abundance. This relationship of the quartz-diorite and quartz-monzodiorite is consistent with the ratio of alkali feldspar/plagioclase observed in thin section. This ratio does not reflect the modal proportion of these minerals for the granodiorite samples, however, due to the anomalously high Sr concentration skewing the ratio. These elements are highly mobile, and the data for these elements may not be reliable since the rocks have experienced greenschist facies alteration.

Niobium in quartz-diorite ranges from 2.41 to 7.3 ppm, and from 7.9 to 10.47 ppm in the quartz-monzodiorite. Sample 19LYH-3586A is an Nb outlier at 4.9 ppm. The granodiorite samples lie off trend with a concentration of 4.89 to 5.06 ppm. Similar to Nb, Ta shows a range of values that overlap between lithology groups. The lower end of the range is in the quartz-diorite samples at 0.18 to 1.4 ppm, while the quartz-monzodiorite has 0.5 to 1.8 ppm. The granodiorite samples average at 0.41 ppm.

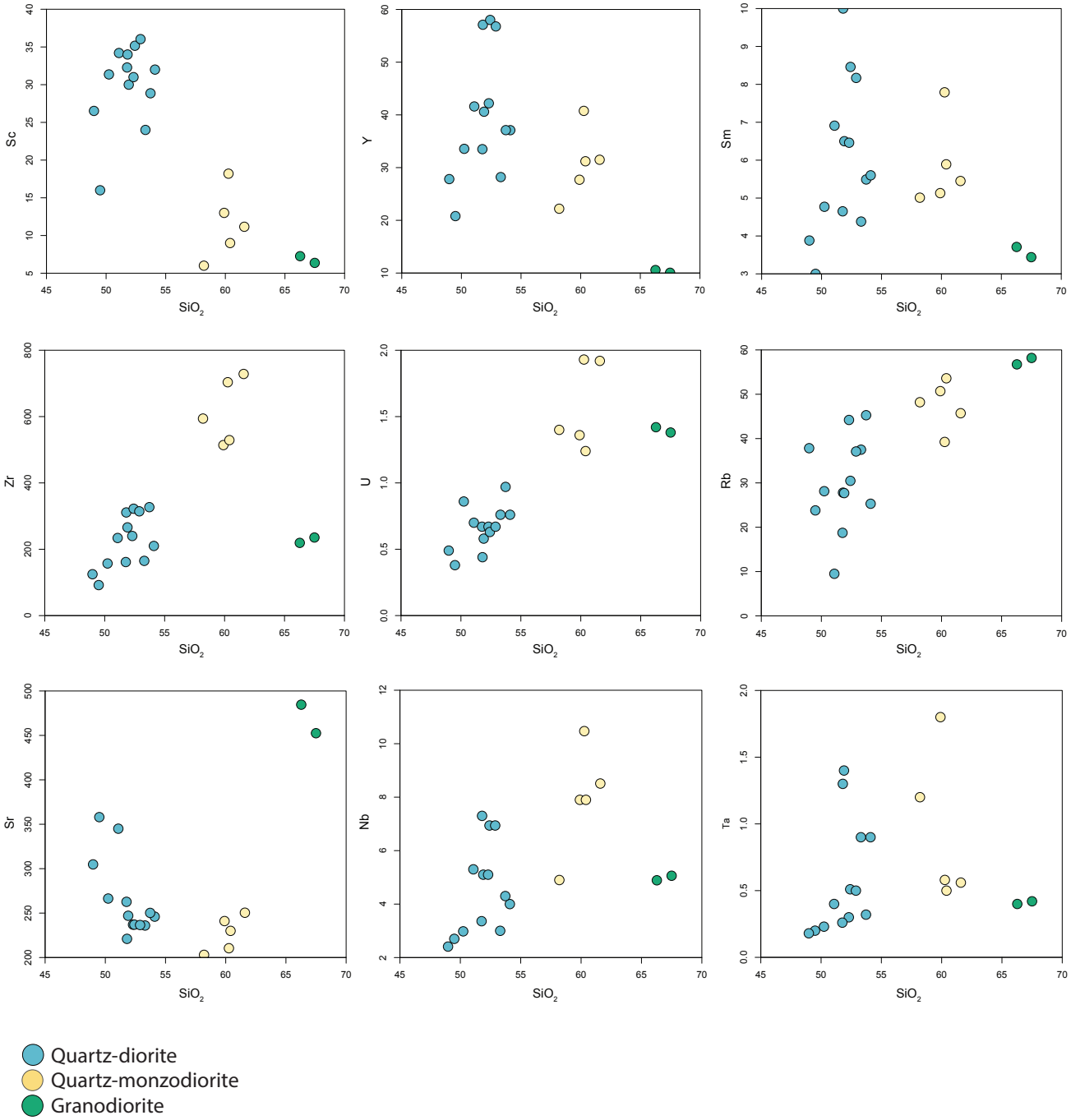

Figure 19: Trace element Harker plots for all samples

5.4.1 Trace Element Anomalies

The niobium anomaly, expressed as $Nb^{*}=Nb_N/(K_N \bullet La_N)^{0.5}$, is very similar in the quartz-diorite and quartz-monzodiorite. The quartz-diorite samples range from 0.19 to 0.39, and the quartz-monzodiorite samples range from 0.18 to 0.27. Granodiorite has the lowest Nb* with an average of 0.15. Typical Nb* values for a continental arc are 0.2 – 0.5 (Schmidt and Jagoutz 2017).

The zirconium anomaly, expressed as $Zr^{*}=Zr_N/(Nd_N \bullet Sm_N)^{0.5}$, shows a positive correlation with silica, except for the granodiorite samples. The quartz-diorite samples range from 1.09 to 2.13, while the quartz-monzodiorite samples are 3.08 to 4.57. The average Zr* value for the granodiorite samples is 1.87. Typical primitive calc-alkaline arc rocks have Zr* values of 0.6 – 1.4 (Schmidt and Jagoutz 2017). The high anomaly value seen in these samples may be due to magma differentiation or crustal contamination.

The lead anomaly, expressed as $Pb^{*}=Pb_N/(Ce_N \bullet Nd_N)^{0.5}$, follows a positive trend with silica saturation, aside from granodiorite. The quartz-monzodiorite samples range from 2.88 to 5.26, while the quartz-diorite samples range from 0.691 to 3.01. The granodiorite samples have an average Pb* value of 3.50. Primitive arc magmas typically have a positive Pb anomaly relative to normalized REE abundances (Schmidt and Jagoutz 2017).

Unlike Zr* and Pb*, the titanium anomaly, expressed as $Ti^{*}=Ti_N/(Gd_N \bullet Tb_N)^{0.5}$ shows a negative correlation with silica. The quartz-diorite samples range from 0.70 to 0.97, while the quartz-monzodiorite samples range from 0.39 to 0.66. The granodiorite samples have an average Ti* of 0.738. All arcs have a global primitive average of 0.95 ± 0.05 (Schmidt and Jagoutz 2017). The below average values seen in these samples may be caused by magma evolution, crustal differentiation, or titanium being in a residual phase.

The strontium anomaly, expressed as $Sr^{*}=Sr_N/(Ce_N \bullet Nd_N)^{0.5}$, follows a negative trend with silica saturation, aside from the granodiorite samples. The granodiorite samples have anomalously high Sr, with an average Sr* value of 17.87, while the quartz-diorite and quartz-monzodiorite samples have values ranging from 11.22 to 18.18 and 9.06 to 11.60, respectively. Primitive arc magmas typically have a positive strontium anomaly with respect to normalized REE concentrations (Schmidt and Jagoutz 2017)

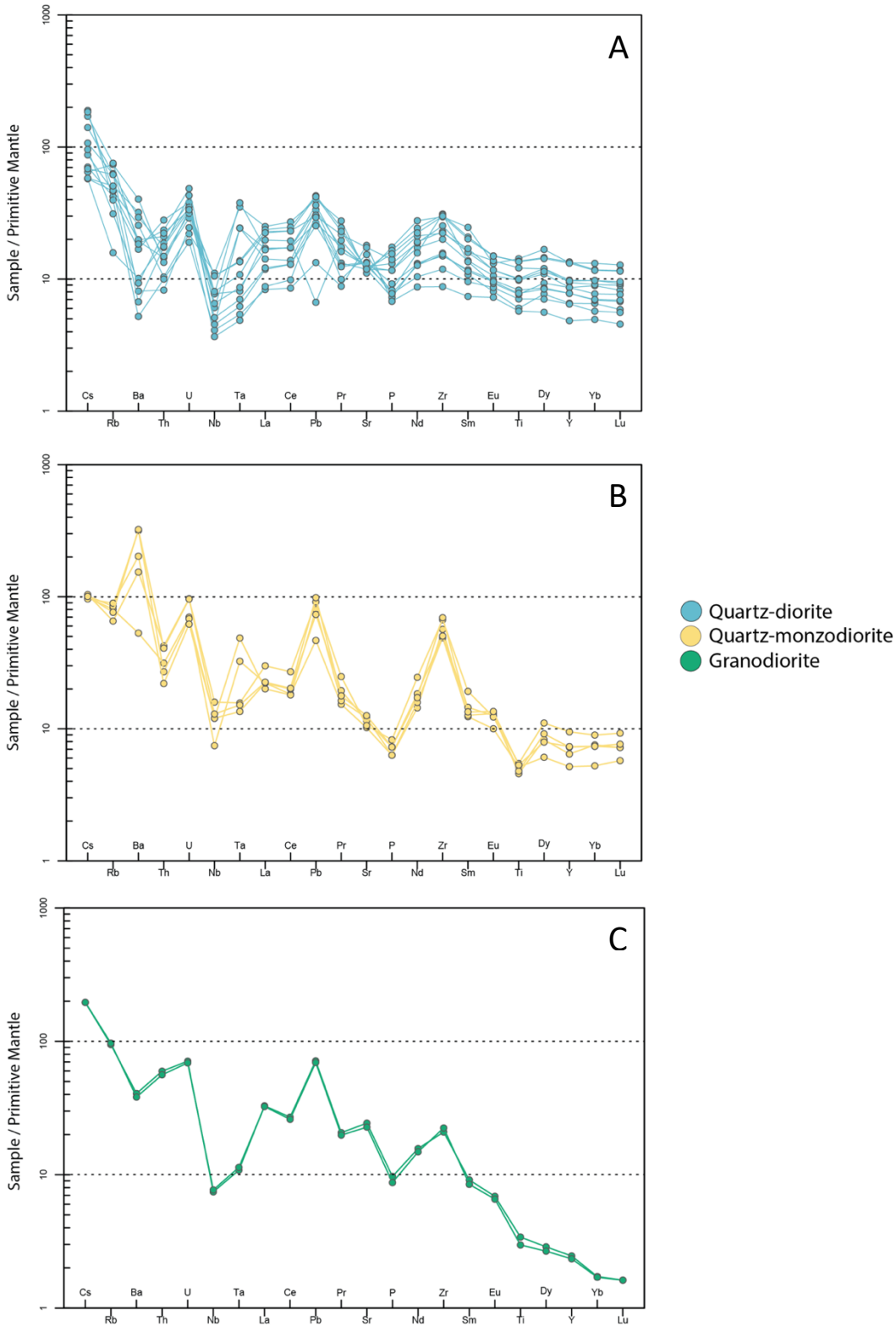

Figure 20: Trace element spider diagrams for all samples. Trace element anomaly patterns discussed in Section 5.4.1 can be seen here.

5.5 Rare-earth Elements

5.5.1 Quartz-diorite

The primitive mantle (Mcdonough and Sun 1995) normalized rare-earth element (PM-REE) patterns for the quartz-diorite samples are relatively flat stacked series, indicating the samples could be related to each other through fractionation (Figure 18). There is a slight enrichment in light rare-earth elements (LREE) relative to heavy rare-earth elements (HREE) with an average La_N/Yb_N value of 1.92. The LREE pattern is flat with an average La_N/Sm_N value of 1.14. The middle rare earth elements are only slightly enriched compared to the HREE with an average Gd_N/Yb_N value of 1.44, suggesting the absence of garnet in the magma source. For all but two samples negative Eu anomaly is present in the more evolved samples, with Eu/Eu* values ranging from 0.58 to 0.93, which suggests plagioclase fractionation. The total REE value ranges from 50 ppm in the most primitive sample to 108 ppm in the most fractionated sample. No correlation is apparent between total REE and silica abundance.

5.5.2 Quartz-monzodiorite

The quartz-monzodiorite PM-REE pattern is similar to that of quartz-diorite, but shows slightly higher LREE. The average La_N/Yb_N value is 3.27, showing a steeper negative slope than the quartz-diorite (Figure 18). The LREE are slightly enriched compared to the MREE with an average La_N/Sm_N value of 1.63, indicating there is a slight enrichment in the source. An average Gd_N/Yb_N value of 1.44 indicates the absence of garnet in the restite. The Eu/Eu* values range from 0.72 to 1.13, with the most primitive samples showing slight positive anomaly, suggesting plagioclase accumulation; while the more fractionated samples show a negative anomaly, suggesting plagioclase depletion. The total REE value ranges from 90 ppm in the most primitive sample to 139 ppm in the most fractionated sample. There is no correlation with total REE and silica abundance.

5.5.3 Granodiorite

The PM-REE plot for the granodiorite samples is vastly different from the other two lithologies (Figure 18). There is a strong LREE enrichment with an average La_N/Yb_N value of 19.07. There is a strong MREE enrichment relative to HREE, indicated by the average Gd_N/Yb_N value of 2.90. The strong LREE and MREE enrichment relative to HREE, suggesting

garnet was present in the restite. No Eu anomalies are present in this unit. The average total REE value is 101 ppm.

5.6 Conserved Element Analysis

Conserved element analysis involves comparing elements that do not experience material transfer when a rock undergoes a compositional change (Stanley and Pearce 1990, Stanley 2020). If a suite of rocks was produced from the same magma source, the ratio of conserved element masses will remain consistent, even if the rocks have experienced addition or removal of material such as mineral fractionation or accumulation (Nicholls 1988, Stanley and Pearce 1990). Correlation of conserved elements can be used to determine if the rocks in a suite are comagmatic, so long as the elements do not have similar geochemical affinities and do not experience coherent mobility (Stanley 2020).

A variety of major elements and trace elements were plotted against each other for the whole dataset to test for conserved elements. TiO_2 and P_2O_5 were identified as candidates for conserved elements, as they define a coherent array that plots thought the origin on a scatter plot. They also have different chemical affinities, and therefore do not display coherent mobility. As seen in Figure 22, the quartz-diorite and quartz-monzodiorite samples fall on a liner trend that passes through the origin, with the slope being equal to the conserved element ratio. This means these two lithologies share a common conserved ratio of TiO_2 and P_2O_5. The granodiorite samples do not lie on this trendline, meaning the conserved element ratio is different for the granodiorite samples. This suggests that the quartz-diorite and quartz-monzodiorite are cogenetic and the granodiorite does not share the same magma source.

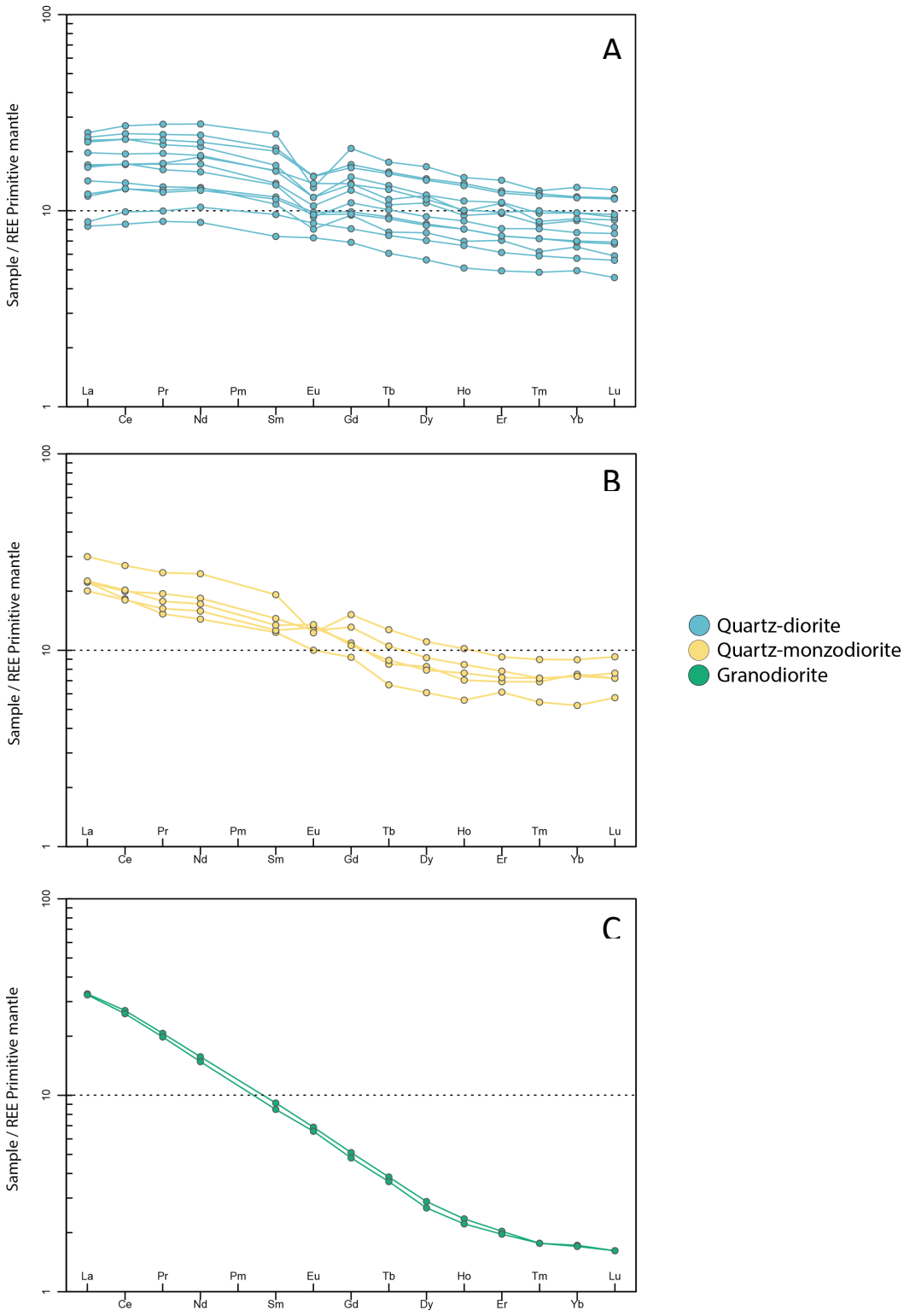

Figure 21: Rare-Earth Element spider diagrams of all samples

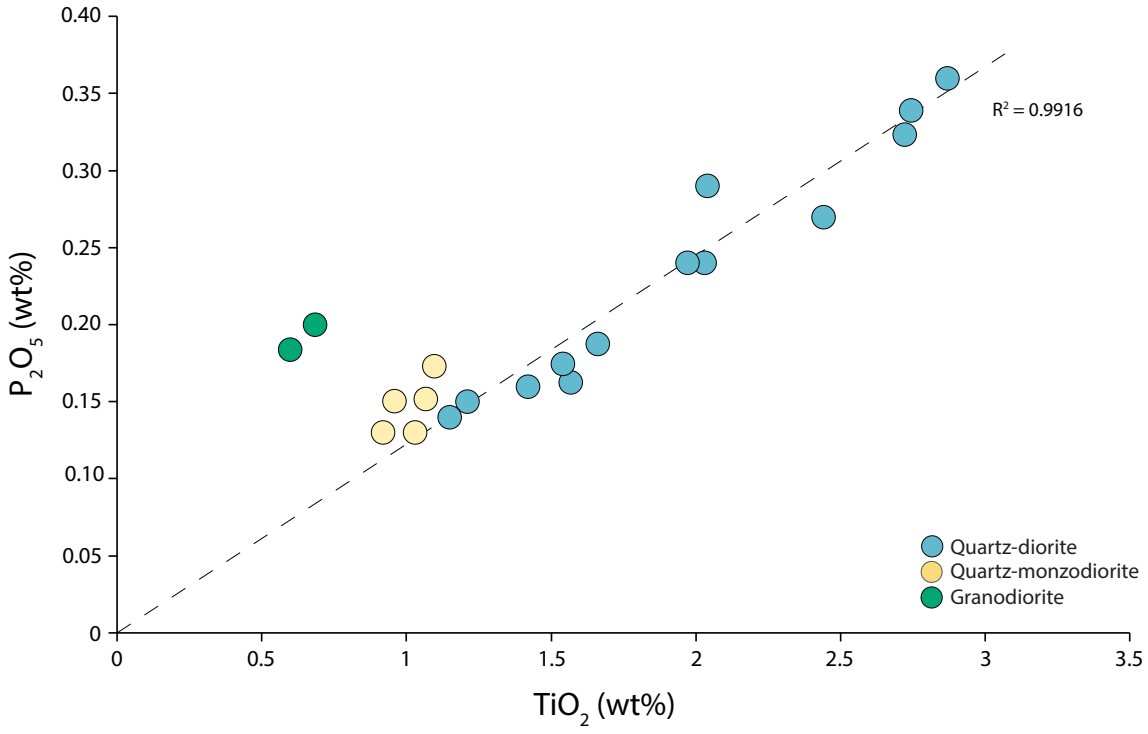

Figure 22: Conserved element analysis plot. The quartz-diorite and quartz-monzodiorite samples lie along a straight line that intersects at the origin, while the granodiorite does not follow the trend.

5.7 Geochemical affinities and tectonic setting

5.7.1 Quartz-diorite

All samples plot in the calc-alkaline field in the centre of the diagram, close to the transitional line between calc-alkaline and tholeiite series on the AFM diagram by Irvine and Baragar (1971) (Figure 23A). They are metaluminous (Shand 1943) and within the arc field on the discrimination diagram of Hildebrand and Whalen (2014) (Figure 23B). On the diagram of Harris et al. (1986), samples are distributed between the volcanic arc field and the within plate field (Figure 23C). This range of source region classification is typical of collisional magmas, as the collision process is dynamic and the signature may change through the evolution of the collision (Harris et al. 1986). Similarly, most samples plot in the volcanic arc granite field on a Pearce et al. (1984) discrimination diagram, with a few samples overlapping into the within plate granite field (Figure 23D). This diagram was intended for use with granitic rocks, so interpretations made using this discrimination plot should be used with caution, as these samples are more intermediate in composition. On the Cabanis and Lecolle (1989) diagram, most samples plot in the orogenic field, with a few samples plotting on the divide between orogenic and late- to post- orogenic (Figure 23E). Overall, the geochemical signature of the quartz-diorite samples suggest that this magma formed in an orogenic volcanic arc setting.

5.7.2 Quartz-monzodiorite

All samples plot in the left-centre of the calc-alkaline field, close to the "A-F" axis on the AFM diagram by Irvine and Baragar (1971) (Figure 23A). They plot near the division line between metaluminous and peraluminous (Shand 1943) and are within the arc field on the discrimination diagram of Hildebrand and Whalen (2014) (Figure 23B). On the diagram of Harris et al. (1986), most samples plot in the volcanic arc field on the diagram, with one sample plotting in the within plate field (Figure 23C). Similarly, these samples plot in the volcanic arc granite field on the discrimination diagram of Pearce et al. (1984) (Figure 23D). This diagram was intended for use with granitic rocks, so interpretations about this lithology group should be made with caution, as these samples are more intermediate in composition. On the Cabanis and Lecolle (1989) diagram, most of the samples plot in the late- to post- orogenic field, with one sample plotting in the orogenic field (Figure 23E). In general, the geochemical signature of the quartz-monzodiorite is consistent with an orogenic volcanic arc setting.

5.7.3 Granodiorite

Both samples plot in the lower left corner of the calc-alkaline field on the AFM diagram by Irvine and Baragar (1971), close to the "A" corner (Figure 23A). They plot near the division line between metaluminous and peraluminous (Shand 1943) and within the slab failure field on the discrimination diagram of Hildebrand and Whalen (2014) (Figure 23B). Both samples plot in the volcanic arc field on the diagram of Harris et al. (1986) (Figure 23C). Similarly, both samples plot in the volcanic arc granite field on a Pearce et al. (1984) discrimination diagram (Figure 23D). On the Cabanis and Lecolle (1989) diagram, these samples plot near the La/10 corner due to the anomalously high La and low Y concentrations (Figure 23E). The geochemical signature of the granodiorite is consistent with a late- to post- collision environment, as it plots in the either the volcanic arc field or in the post-collisional field of several diagrams.

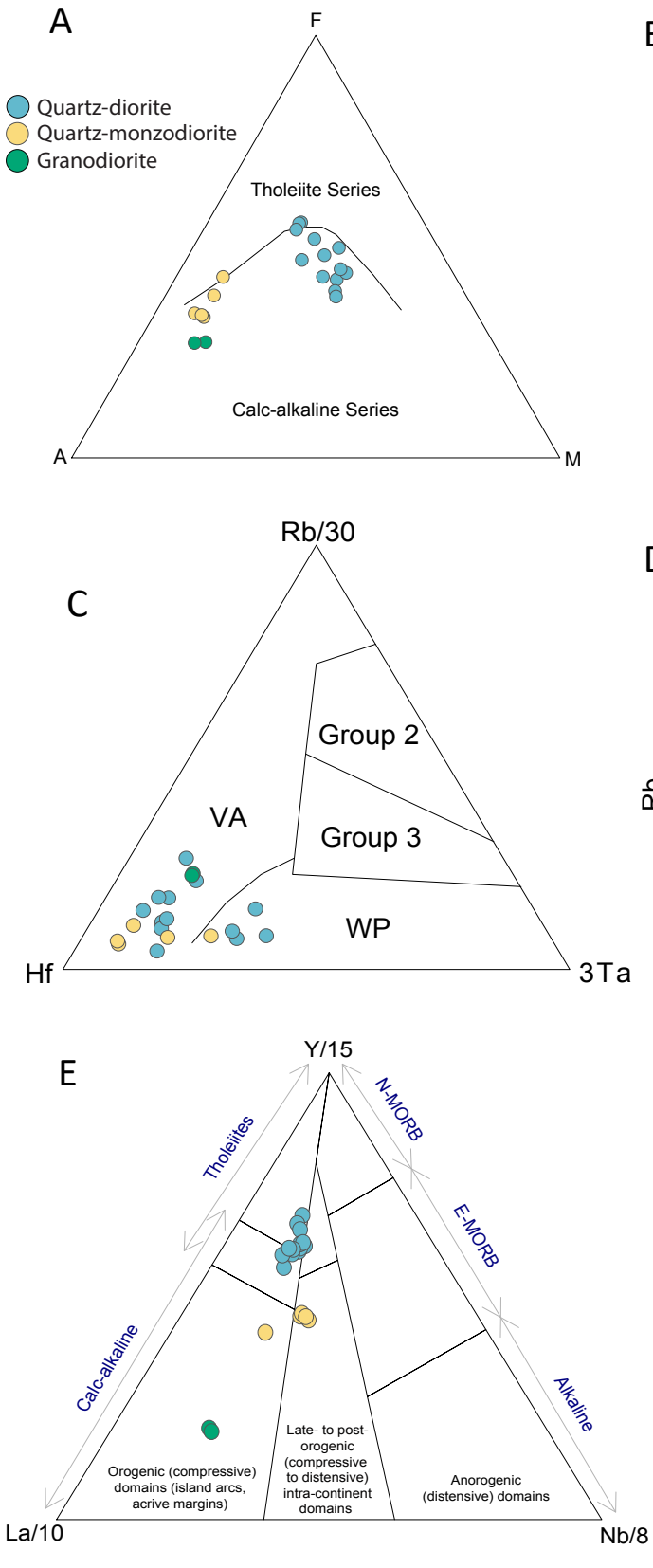

Figure 23: Geotectonic discrimination diagrams:

(A) AFM diagram after Irvine and Baragar (1971).
(B) Slab failure vs arc diagram after Hildebrand and Whalen (2014).
(C) Rb-Hf-Ta triangular plot after Harris et al. (1986).
(D) Rb-(Y+Nb) discrimination diagram after Pearce et al. (1984).
(E) Y/15-La/10-Nb/8 plot after Cabanis and Lecolle (1989).

5.8 Implications of the Geochemical Data

The quartz-diorite and quartz-monzodiorite have differing bulk geochemistry, REE patterns, and trace element signatures, but seem to share a tectonic setting affinity and conserved element ratios. This suggests they formed coevally in the same arc setting. The variations within a lithology group may be explained by fractionation, as the samples show parallel stacked REE patterns, and the stronger anomalies are present in the more fractionated samples.

Only two samples comprise the granodiorite group, and the samples were collected from the same location. There may be greater geochemical variations within the granodiorite unit that have not been identified due to the limited sample set. However, the granodiorite samples do have distinctly different geochemical characteristics compared to the quartz-diorite and quartz-monzodiorite. These samples closely resemble the geochemical characteristics of adakite rocks. Adakite rocks are differentiated using a group of unique geochemical parameters outlined in Table 1. If a sample has all the outlined characteristics, it can be geochemically distinguished as an adakite magma instead of a normal calc-alkaline arc magmas (Richards and Kerrich 2007). As seen in Table 1, the granodiorite samples meet all criteria of an adakitic rock.

Table 1: Characteristics of an adakite rock defined by Defant and Drummond (1990), compared to characteristics of the granodiorite samples in this study

Adakite geochemical parameter (Defant and Drummond, 1990)	Average for granodiorite samples (this study)
>56 wt% SiO_2	67 wt%
>15 wt% Al_2O_3	16 wt%
Usually <3 wt% MgO	1.4 wt%
High Sr (≥400 ppm)	469 ppm
Low Y (≤18 ppm)	10 ppm
Low Yb (≤1.9 ppm)	0.76 ppm
High Sr/Y ratio (≥20)	45 ppm
High La/Yb ratio (≥20)	28 ppm

6.0 Summary and Discussion

6.1 Summary

6.1.1 Petrography and Field Relationships

As discussed in Section 3 above, there are three main lithologies that comprise this pluton: quartz-diorite, quartz-monzodiorite, and granodiorite. The quartz-diorite and quartz-monzodiorite are mingled together and form most of the intrusion which is located near the margin of a major fault. It is likely that the mingling magma ascended through the crust via the pre-existing fault.

In thin section, both the quartz-diorite and quartz-monzodiorite show a unique igneous texture of clinopyroxene cores surrounded by hornblende rims. This mineralogical change records a hydration crystallization process, which requires the magma to contain upwards of 5% water (Grove et al. 2002, Beard et al. 2004). This hydration texture associated with the presence of other anhydrous minerals such as plagioclase and quartz is commonly found in mafic to intermediate plutons related to arc settings (Beard et al. 2004). One quartz-diorite sample contained a few olivine grains. The presence of olivine and the remnant clinopyroxene cores suggests that this magma composition initially may have been of more mafic gabbroic composition prior to magma hydration. It is possibly that the magmas became enriched in fluids as they ascended through the pre-existing fault, causing this hydration reaction to occur.

6.1.2 U-Pb Geochronology

Two quartz-diorite samples yielded U-Pb zircon ages of 269.53 ± 1.51 Ma and 273.43 ± 2.24 Ma, respectively. The quartz-monzodiorite yielded an age of 269.08 ± 2.03 Ma. These ages are interpreted to be the crystallization age of each sample, respectively. The U-Pb ages of the two lithologies overlap within error. The three samples had similar zircon morphologies, exhibiting coarse equidimensional grains with dark corroded cores surrounded by oscillatory zoned rims. This suggests that the zircon grains from both lithologies crystallized in the same magma chamber. Based on this data, it is interpreted that a singular magma source experienced crystallization differentiation, producing the quartz-diorite and quartz-monzodiorite magmas coevally. These two cogenetic magmas then interacted and partially mixed as they ascended through the crust in a mingling magma setting.

The granodiorite produced two different zircon groups. Group I zircons had a higher aspect ratio and had continuous oscillatory zoning throughout the entire grain. They yielded a U-Pb age of 261.85 ± 2.82 Ma, interpreted to be the crystallization age of the granodiorite. Group II zircons had a lower aspect ratio and showed a dark corroded core surrounded by an oscillatory zoned rim. They yielded an age of 269.76 ± 3.25 Ma. Both the morphology and concordia age of Group II zircons match that of the quartz-diorite and quartz-monzodiorite mingled pluton. Therefore, Group II zircons are interpreted to be inherited from the mingled pluton that the granodiorite dike crosscuts.

6.1.3 Geochemistry

The geochemical signatures of the quartz-diorite and quartz-monzodiorite suggest that they are cogenetic and formed coevally in a continental arc setting. The chemical signature of the granodiorite is consistent with a late- to post-collisional setting. The granodiorite samples also possess a set of unique geochemical parameters that define adakite-type rocks, which can be used to interpret the type of magma source. Adakite rocks are commonly considered to be caused by partial slab melting in the presence of garnet and absence of plagioclase (Martin 1999). However, previous studies have shown that these chemical characteristics may be produced in several scenarios including: melting of thickened lower crust, subducted continental crust, or juvenile oceanic crust; abnormally hot melting of old, hydrated, oceanic crust; melting of garnet amphibolite rocks or eclogites; or fractional crystallization and assimilation (Defant and Drummond 1990, Martin 1999, Chung et al. 2003, Gao et al. 2004, Macpherson et al. 2006, Richards and Kerrich 2007, Moyen 2009, Bea 2012). Each of these scenarios produce slightly different geochemical characteristics that can be difficult to discern from each other. The granodiorite group in this study is very limited and does not have the potential to show the various characteristics used to differentiate these magma production scenarios. More data is required to geochemically predict which scenario created these rocks.

6.2 Tectonic Implications

6.2.1 Current Tectonic History Model

The location and timing of the final closure of the Paleo-Asian Ocean has been a heated debate amongst researchers. The most recent model proposed by Santos et al. (2022) suggests that the final vestige of the ocean closed at the site of the Liuyuan Complex (Figure 2). Back-arc

basin spreading occurred between Composite Siberia and the Ganquan arc from 295 – 282 Ma due to slab roll back. Northward subduction under Composite Siberia flipped the system from back-arc basin to forearc setting around 281 Ma, consuming the oceanic crust, and closing the basin. The Liuyuan ophiolite was then thrust against the Ganquan arc-related Permian sediments to the south by 279 Ma. This model proposes that the last vestige of the Paleo-Asian Ocean was closed at this location by 279 Ma.

6.2.2 Generation of the Nanquan Arc

The ca. 270 Ma Nanquan Quarry pluton with arc affinity adds a new phase to an already tectonically complex region. The Nanquan Quarry arc is younger and petrogenetically different than all other terranes found in the local area and is separated from the other terranes by an extensive thrust fault. This intrusion is unique from all other local terranes and marks a new tectonic phase to the southern Beishan geologic history. However, conclusions from this limited data set should be used with caution, as it is collected from only one pluton. This area is not extensively mapped in detail and has limited available data in the literature. It is assumed that this pluton is part of a suite of arc rocks that are representative of an event that may have occurred for a longer timespan than 273 to 269 Ma, as recorded by this thesis.

Based on the surrounding geology, there are two scenarios in which this arc could have been developed:

1. North-dipping subduction of a terrane from the Dunhuang Orogenic Belt under the South Baidunzi Complex (Figure 24).
2. South-dipping subduction between the North Baidunzi Complex and the South Baidunzi Complex (Figure 25).

The emplacement of this pluton seems to have been structurally controlled by the steeply south-dipping fault located just north of the intrusion. The semi-major axis of this elongated pluton is oriented sub-parallel to the fault, and the close proximity to the fault line suggests that the pluton may have used the active fault as a path of least resistance during its ascent through the crust. As mentioned in Clemens (2005), granitoid magmas are typically less dense than the surrounding crust and the buoyancy allows the magma to rise, typically through pre-existing or newly created fractures or fault. The deformation in the shear zone between the North Baidunzi Complex (north) and the South Baidunzi Complex (south) was from ca. 277 to 271 Ma (Hong, T.

and Lin, S., unpublished data, personal communication), and the pluton has an age of ca. 273 to 269 Ma. Therefore, the pluton is late syn- or post-kinematic with the fault.

Scenario 1 requires movement along the fault to bring the North and South Baidunzi Complexes together. According to Xiao et al. (2018), dextral movement occurred in the Beishan-Dunhuang region from 295 to 225 Ma, which could have been responsible for bringing the North and South Baidunzi Complexes together. According to the age relationships between the arc magmatism and fault deformation, magmatism and deformation would need to be occurring simultaneously. A collision of the Dunhuang terrane with the South Baidunzi Complex may have triggered thrust movement on the pre-existing fault. However, this is unlikely as the steeply dipping fault would be mechanically difficult to reactivate as a thrust fault because thrust motion is inefficient in a sub-vertical structure.

The arc signature in the Nanquan Quarry pluton could have been from arc magmatism, or arc-like magmatism produced from slab break-off. If it was arc-like magmatism, one would expect to see true arc rocks to the north that slightly pre-date the Nanquan Quarry pluton, however no such rocks have been identified. If they were produced by true arc magmatism, one would expect to see similar rocks emplaced on the north side of the thrust fault in the North Baidunzi Complex as well, however no such rocks have been identified. It is possible that there are similar rocks further to the south, and the Nanquan Quarry pluton marks the northern-most boundary of this intrusive arc complex. It is also possible that more plutons exist laterally along the fault, outside the mapping area of this study.

If Scenario 1 was correct, the Dunhuang terrane may have the following features: a higher metamorphic grade than the South Baidunzi Complex, as it would have been the down-going slab; a passive margin sequence; different country rock or basement than the South Baidunzi Complex; and rocks with a post-collisional metamorphic age of post-269 Ma, after the Nanquan Quarry pluton crystallized. The suture zone between the South Baidunzi Complex and Dunhuang terrane has yet to be located.

Scenario 2 suggests that the magmatism which created the Nanquan Quarry pluton could have been arc magmatism, or arc-like magmatism produced from slab break-off which may have been triggered shortly after a collision occurred. If the Nanquan Quarry pluton was formed from an arc, the magmatism would need to be occurring syntectonically with the deformation in the fault that separates the North and South Baidunzi Complexes. If the pluton was formed from

arc-like magmatism related to slab break-off, then one would expect to see true arc magmatism emplaced south of the South Baidunzi Complex, somewhere in the Dunhuang terrane, that pre-dates the Nanquan Quarry pluton. One mylonitic quartz-rich granite sample in Feng et al. (2020) has a magmatic age of 275 ± 4 Ma with a continental arc signature, interpreted to be from a north-dipping subduction zone occurring from 284 to 275 Ma (Feng et al. 2020). This granite may be formed from this proposed south-dipping subduction zone, rather than the north-dipping subduction zone as interpreted in their published work. If that is the case, that would suggest that south-dipping subduction ended at around 275 Ma, which would be the onset of the collision between the Dunhuang terrane and the North Baidunzi Complex. As subduction verged northward, the South Baidunzi Complex located on leading edge of the terrane, is thrust onto the North Baidunzi Complex. Slab break-off occurs, and arc-like magmatism produced the Nanquan Quarry pluton simultaneously as deformation occurs in the thrust fault. This scenario also suggests that the South Baidunzi Complex is part of the Dunhuang terrane, which would mean the two terranes may share a common basement.

The Nanquan Quarry arc and South Baidunzi Complex may be part of the Beishan, but also may belong to the Dunhuang Orogenic Belt, which may just be an extension of the Beishan of Central Asian Orogenic Belt, as proposed by Feng et al. (2020). Based on the available data, there are two possible models for the tectonic setting that created the Nanquan Quarry arc (Figure 24 and 25).

This study offers new data that unlocked a new tectonic phase in the Beishan Orogenic Collage. We propose that the generation of the Nanquan Quarry arc may mark the location of the last vestige of the Paleo-Asian Ocean, which may have closed ca. 10 million years later than previous models suggest.

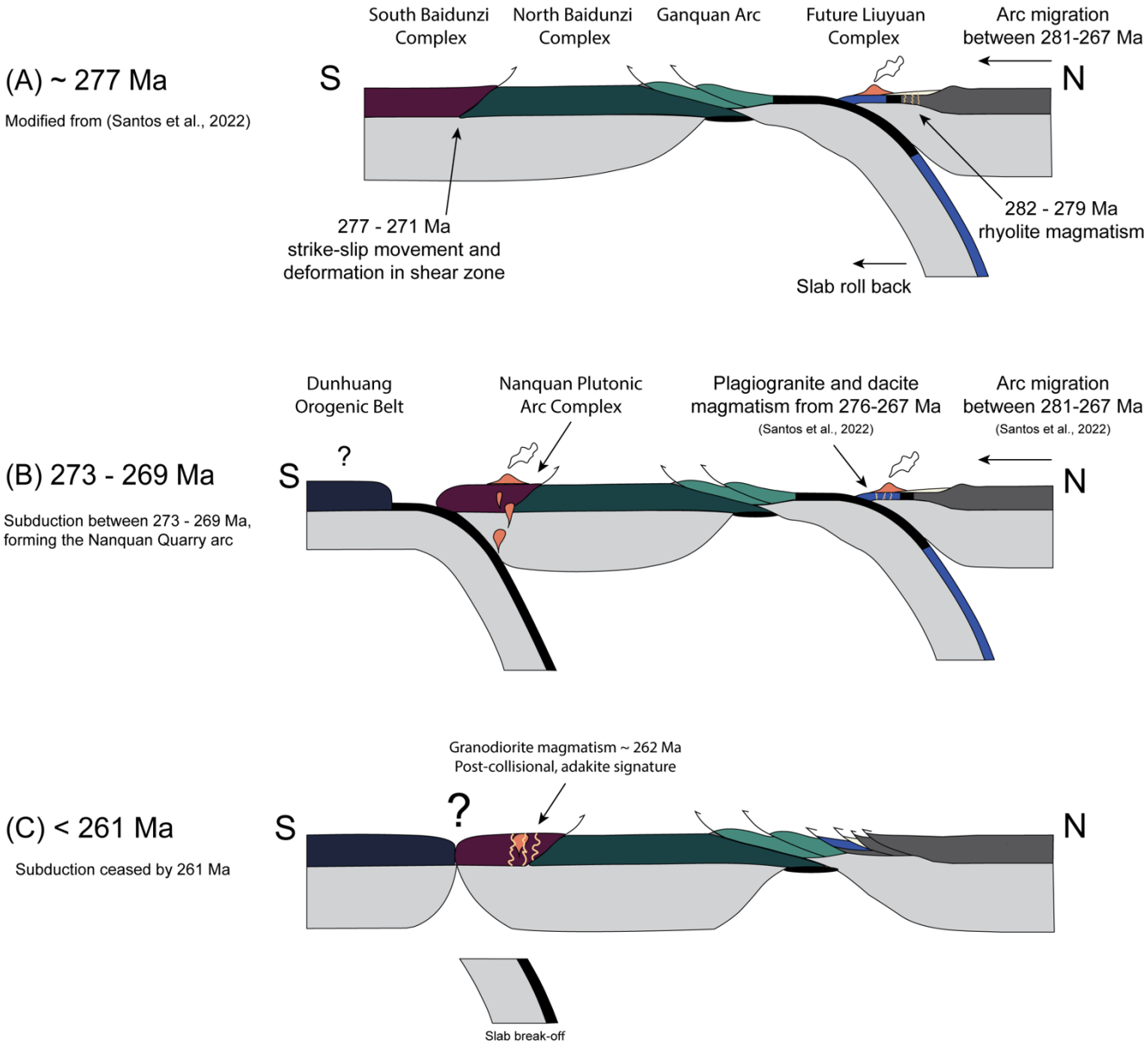

Figure 24: Summative diagram Scenario 1 of the formation of the Nanquan Arc. (A) The North Baidunzi Complex and South Baidunzi Complex are brought together through strike-slip movement along the fault from 277-271 Ma. (B) Northward subduction of a terrane from the Dunhuang Orogenic Belt under the South Baidunzi Complex from 273-269 Ma to create the Nanquan arc, where the quartz-diorite and quartz-monzodiorite magmas mingled to form the pluton. (C) Collision between the terrane from the Dunhuang Orogenic Belt and the South Baidunzi Complex occurred before 261 Ma, when post-collisional granodiorite dikes intruded the Nanquan Quarry pluton.

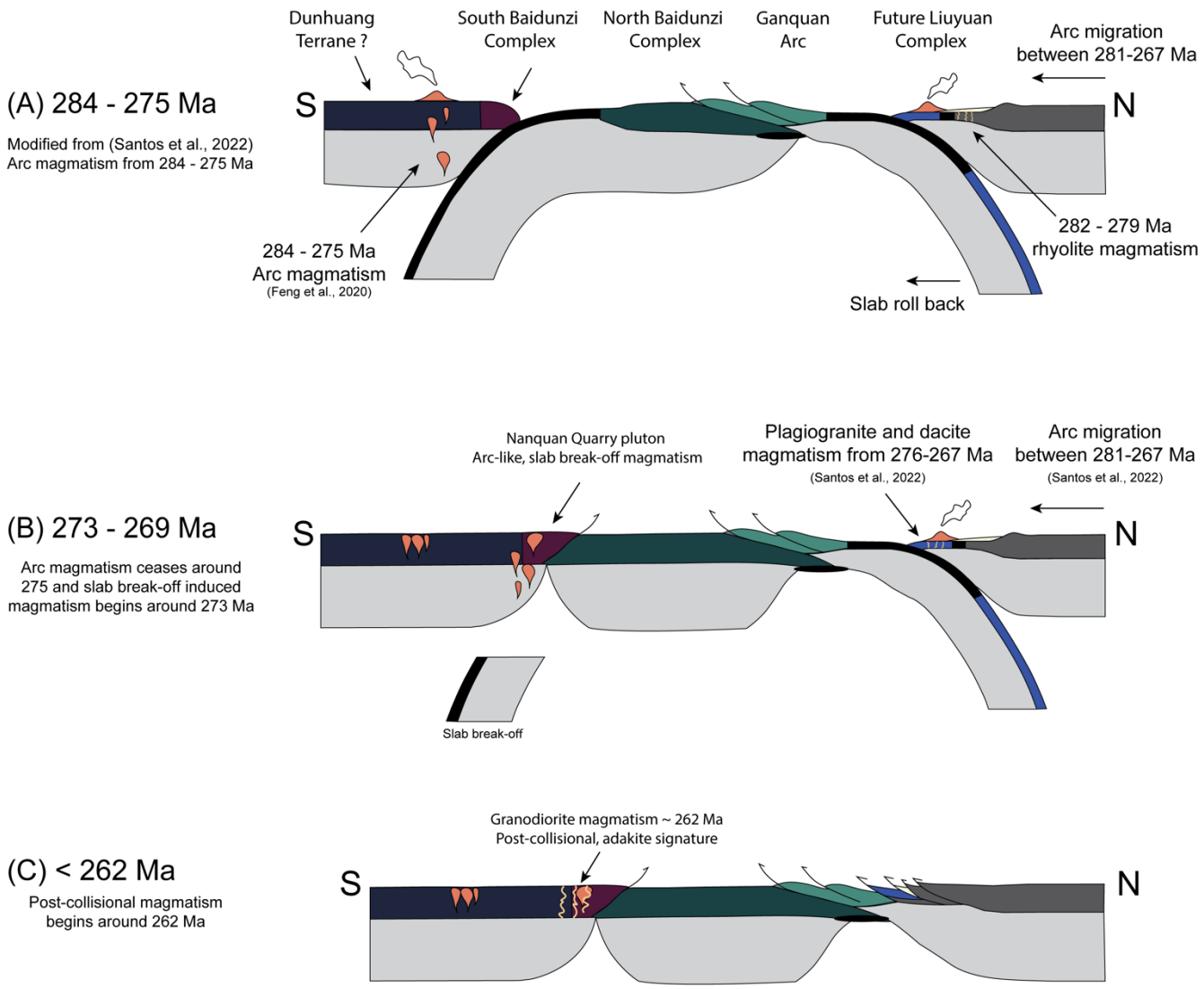

Figure 25: Summative diagram Scenario 2 of the formation of the Nanquan Arc. (A) Subduction of the North Baidunzi Complex under a terrane from the Dunhuang Orogenic Belt and the South Baidunzi Complex occurs from 284-275 Ma to create arc magmatism (Feng et al., 2020) (B) Subduction ceases after 275 Ma due to collision of the two terranes. Slab break-off occurs and creates Nanquan Quarry arc-like magmatism from 273-269 Ma, where the quartz-diorite and quartz-monzodiorite magmas mingled to form the pluton. (C) Post-collisional magmatism occurs around 261 Ma to create the adakitic granodiorite dike intrusions.

7.0 Conclusions and Future Work

7.1 Conclusions

The Nanquan Quarry pluton is an intrusive suite comprised of quartz-diorite mingled with quartz-monzodiorite, intruded by a granodiorite dike. The quart-diorite and quartz-monzodiorite have interpreted crystallization ages of ca. 270 Ma, while the granodiorite dike has an interpreted crystallization age of ca. 261 Ma. The quartz-diorite and quartz-monzodiorite have geochemical signatures that resemble a continental arc setting, while the granodiorite has a post-collisional and adakite signature.

Based on the petrographic, geochronological, and geochemical data presented in this thesis along with other available data, the following conclusions may be reached:

1. The Nanquan Quarry pluton formed from continental arc subduction zone. Arc or arc-like magmatism occurred from ca. 273-269 Ma, and post-collisional magmatism began ca. 261 Ma.
2. Based on the available data, the Nanquan Quarry arc formed in either a north-dipping subduction zone between a terrane from the Dunhuang Orogenic Belt and the South Baidunzi Complex, or a south-dipping subduction zone between the North Baidunzi Complex and the South Baidunzi Complex.
3. The final vestige of the Paleo-Asian Ocean was open ca. 10 million years later than currently proposed. The final closure may be associated with the Nanquan Quarry arc, however more data is required.

7.2 Future Work

The general tectonic setting and timing of this pluton has been documented by this thesis, but further research is required to better understand how this intrusion relates to the regional tectonics occurring in the area. Detailed structural mapping of the region would prove beneficial for the following:

1. Determine the size, extent, and polarity of the subduction zone that created the Nanquan Quarry Arc.

2. Determine how the South Baidunzi Complex is related to the Dunhuang Orogenic Belt by thoroughly mapping the area and locating a suture zone that connects these two terranes.
3. Investigate by which mechanism the adakite-like magma was produced.
4. Develop a more thorough tectonic model by creating a complete cross section through Beishan Orogenic Collage and the Dunhuang Orogenic Belt
5. Expand on the tectonic evolution model of the Central Asian Orogenic Belt with a more thorough understanding of the youngest part of the orogen by better constraining the final closure of the Paleo-Asian Ocean.

References

Andersen, T., Elburg, M.A., and Magwaza, B.N. 2019. Sources of bias in detrital zircon geochronology: Discordance, concealed lead loss and common lead correction. Earth-Science Reviews, **197**: 102899. Elsevier. doi:10.1016/j.earscirev.2019.102899.

Bea, F. 2012. The sources of energy for crustal melting and the geochemistry of heat-producing elements. Lithos, **153**: 278–291. Elsevier B.V. doi:10.1016/j.lithos.2012.01.017.

Beard, J.S., Ragland, P.C., and Rushmer, T. 2004. Hydration crystallization reactions between anhydrous minerals and hydrous melt to yield amphibole and biotite in igneous rocks: Description and implications. Journal of Geology, **112**: 617–621. doi:10.1086/422670.

Black, L.P., Kamo, S.L., Allen, C.M., Aleinikoff, J.N., Davis, D.W., Korsch, R.J., and Foudoulis, C. 2003. TEMORA 1: A new zircon standard for Phanerozoic U-Pb geochronology. Chemical Geology, **200**: 155–170. doi:10.1016/S0009-2541(03)00165-7.

Chung, S.L., Liu, D., Ji, J., Chu, M.F., Lee, H.Y., Wen, D.J., Lo, C.H., Lee, T.Y., Qian, Q., and Zhang, Q. 2003. Adakites from continental collision zones: Melting of thickened lower crust beneath southern Tibet. Geology, **31**: 1021–1024. doi:10.1130/G19796.1.

Claoué-Long, J.C., Compston, W., Roberts, J., and Fanning, C.M. 1995, January 1. Two Carboniferous Ages: A Comparison of Shrimp Zircon Dating with Conventional Zircon Ages and 40Ar/39Ar Analysis. SEPM Society for Sedimentary Geology. doi:10.2110/pec.95.04.0003.

Clemens, J.D. 2005. Granites and granitic magmas: Strange phenomena and new perspectives on some old problems. Proceedings of the Geologists' Association, **116**: 9–16. The Geologists' Association. doi:10.1016/S0016-7878(05)80013-6.

Cleven, N.R., Lin, S., Xiao, W., Davis, D.W., and Davis, B. 2018. Successive arc accretion in the southern Central Asian orogenic belt, NW China: Evidence from two Paleozoic arcs with offset magmatic periods. Bulletin of the Geological Society of America, **130**: 537–557. doi:10.1130/B31434.1.

Compston, W., Williams, I.S., Kirschvink, J.L., Zichao, Z., and Guogan, M.A. 1992. Zircon U-Pb ages for the Early Cambrian time-scale. Journal of the Geological Society, **149**: 171–184.

doi:10.1144/gsjgs.149.2.0171.

Defant, M.J., and Drummond, M.S. 1990. Derivation of some modern arc magmas by melting of young subducted lithosphere. Nature, **347**: 662–665.

Feng, L., Lin, S., Li, L., Davis, D.W., Song, C., Li, J., Ren, S., Han, X., Ge, Y., and Lu, K. 2020. Constraints on the tectonic evolution of the southern central Asian orogenic belt from early Permian–middle Triassic granitoids from the central Dunhuang orogenic belt, NW China. Journal of Asian Earth Sciences, **194**: 104283. Elsevier. doi:10.1016/j.jseaes.2020.104283.

Gan, B., Diwu, C., Wu, L., and Wang, T. 2021. Geochronology, geochemistry, and Sr-Nd-Pb-Hf isotopes of the late Paleozoic Dongshuigou composite pluton in the Dunhuang Block, southernmost Central Asian Orogen: Petrogenesis and implications for crustal growth. Lithos, **384**–**385**: 105970. Elsevier B.V. doi:10.1016/j.lithos.2021.105970.

Gao, J., He, G., Li, M., Xiao, X., Tang, Y., Wang, J., and Zhao, M. 1995. The mineralogy, petrology, metamorphic PTDt trajectory and exhumation mechanism of blueschists, south Tianshan, northwestern China. Tectonophysics, **250**: 151–168. doi:10.1016/0040-1951(95)00026-6.

Gao, S., Rudnick, R.L., Yuan, H.L., Liu, X.M., Liu, Y.S., Xu, W.L., Ling, W.L., Ayers, J., Wang, X.C., and Wang, Q.H. 2004. Recycling lower continental crust in the North China craton. Nature, **432**: 892–897. doi:10.1038/nature03162.

Grove, T., Parman, S., Bowring, S., Price, R., and Baker, M. 2002. The role of an H2O-rich fluid component in the generation of primitive basaltic andesites and andesites from the Mt. Shasta region, N California. Contributions to Mineralogy and Petrology, **142**: 375–396. doi:10.1007/s004100100299.

Harris, N.B.W., Pearce, J.A., and Tindle, A.G. 1986. Geochemical characteristics of collision-zone magmatism. Geological Society Special Publication,: 67–81.

He, Z.Y., Klemd, R., Yan, L.L., and Zhang, Z.M. 2018. The origin and crustal evolution of microcontinents in the Beishan orogen of the southern Central Asian Orogenic Belt. Earth-Science Reviews, **185**: 1–14. Elsevier. doi:10.1016/j.earscirev.2018.05.012.

Hildebrand, R.S., and Whalen, J.B. 2014. Arc and Slab-failure Magmatism in Cordilleran Batholiths II - The Cretaceous Peninsular Ranges Batholith of Southern and Baja California. Geoscience Canada,

41: 399–458.

Hong, T., van Staal, C.R., and Lin, S. 2019. Evolution of the southern Beishan Orogenic Collage, NW China: implications for the closure of the Paleo-Asian Ocean. *In* GAC-MAC-IAH Quebec 2019 May 12-15. pp. 111–112.

Hong, T., van Staal, C.R., and Lin, S. 2022. Evolving Permian arc magmatism associated with slab rollback in the southern Beishan Orogen Collage, Central Asian orogenic belt, NW China. *In* GAC-MAC-IAH Halifax 2022 May 15-18. p. 114. Available from https://www.researchgate.net/publication/269107473_What_is_governance/link/548173090cf22525dcb61443/download%0Ahttp://www.econ.upf.edu/~reynal/Civil wars_12December2010.pdf%0Ahttps://think-asia.org/handle/11540/8282%0Ahttps://www.jstor.org/stable/41857625.

Huang, B.T., He, Z.Y., Zhang, Z.M., Klemd, R., Zong, K.Q., and Zhao, Z.D. 2015. Early Neoproterozoic granitic gneisses in the Chinese Eastern Tianshan: Petrogenesis and tectonic implications. Journal of Asian Earth Sciences, **113**: 339–352. Elsevier Ltd. doi:10.1016/j.jseaes.2014.08.021.

Irvine, T.N., and Baragar, W.R.A. 1971. A Guide to the Chemical Classification of the Common Volcanic Rocks. Canadian Journal of Earth Sciences, **8**: 523–548. doi:10.1139/e71-055.

Kröner, A., Alexeiev, D. V., Hegner, E., Rojas-Agramonte, Y., Corsini, M., Chao, Y., Wong, J., Windley, B.F., Liu, D., and Tretyakov, A.A. 2012. Zircon and muscovite ages, geochemistry, and Nd-Hf isotopes for the Aktyuz metamorphic terrane: Evidence for an Early Ordovician collisional belt in the northern Tianshan of Kyrgyzstan. Gondwana Research, **21**: 901–927. International Association for Gondwana Research. doi:10.1016/j.gr.2011.05.010.

Liu, Q., Zhao, G., Sun, M., Eizenhöfer, P.R., Han, Y., Hou, W., Zhang, X., Wang, B., Liu, D., and Xu, B. 2015. Ages and tectonic implications of Neoproterozoic ortho- and paragneisses in the Beishan Orogenic Belt, China. Precambrian Research, **266**: 551–578. Elsevier B.V. doi:10.1016/j.precamres.2015.05.022.

Lu, S., Li, H., Zhang, C., and Niu, G. 2008. Geological and geochronological evidence for the Precambrian evolution of the Tarim Craton and surrounding continental fragments. Precambrian Research, **160**: 94–107. doi:10.1016/j.precamres.2007.04.025.

Macpherson, C.G., Dreher, S.T., and Thirlwall, M.F. 2006. Adakites without slab melting: High pressure differentiation of island arc magma, Mindanao, the Philippines. Earth and Planetary Science Letters, **243**: 581–593. doi:10.1016/j.epsl.2005.12.034.

Mao, Q., Xiao, W., Windley, B.F., Han, C., Qu, J., Ao, S., Zhang, J., and Guo, Q. 2012a. The Liuyuan complex in the Beishan, NW China: A Carboniferous-Permian ophiolitic fore-arc sliver in the southern Altaids. Geological Magazine, **149**: 483–506. doi:10.1017/S0016756811000811.

Mao, Q., Xiao, W., Windley, B.F., Han, C., Qu, J., Ao, S., Zhang, J., and Guo, Q. 2012b. The Liuyuan complex in the Beishan, NW China: A Carboniferous-Permian ophiolitic fore-arc sliver in the southern Altaids. Geological Magazine, **149**: 483–506. doi:10.1017/S0016756811000811.

Martin, H. 1999. Adakitic magmas: Modern analogues of Archaean granitoids. Lithos, **46**: 411–429. doi:10.1016/S0024-4937(98)00076-0.

Mcdonough, W.F., and Sun, S.S. 1995. The composition of the Earth '. **2541**.

Moyen, J.F. 2009. High Sr/Y and La/Yb ratios: The meaning of the "adakitic signature." Lithos, **112**: 556–574. Elsevier B.V. doi:10.1016/j.lithos.2009.04.001.

Nasdala, L., Hofmeister, W., Norberg, N., Martinson, J.M., Corfu, F., Dörr, W., Kamo, S.L., Kennedy, A.K., Kronz, A., Reiners, P.W., Frei, D., Kosler, J., Wan, Y., Götze, J., Häger, T., Kröner, A., and Valley, J.W. 2008. Zircon M257 - A homogeneous natural reference material for the ion microprobe U-Pb analysis of zircon. Geostandards and Geoanalytical Research, **32**: 247–265. doi:10.1111/j.1751-908X.2008.00914.x.

Nelson, D.R. 1998. Compilation of SHRIMP U-Pb Zircon Geochronology Data, 1997. Geological Survey of Western Australia. Available from https://books.google.ca/books?id=oaY_AQAACAAJ.

Nicholls, J. 1988. The statistics of Pearce element diagrams and the Chayes closure problem. Contributions to Mineralogy and Petrology, **99**: 11–24. doi:10.1007/BF00399361.

Pearce, J.A., Harris, N.B.W., and Tindle, A.G. 1984. Trace element discrimination diagrams for the tectonic interpretation of granitic rocks. Journal of Petrology, **25**: 956–983. doi:10.1093/petrology/25.4.956.

Richards, J.P., and Kerrich, R. 2007. Special Paper: Adakite-Like Rocks: Their Diverse Origins and

Questionable Role in Metallogenesis. Economic Geology, **102**: 537–576.

Santos, G.S., Hong, T., van Staal, C.R., Bedard, J., and Lin, S. 2022a. Permian back-arc basin formation and arc migration in the southern Central Asian Orogenic Belt, NW China. Geological Journal Short Cumunications,.

Santos, G.S., Hong, T., van Staal, C.R., Bedard, J., and Lin, S. 2022b. Back-arc basin formation at the last stages of the Paleo-Asian Ocean evolution, Central Asian Orogenic Belt: A new tectonic framework based on evidence from the Liuyuan Complex and surrounding units, NW China. *In* GAC-MAC-IAH Halifax 2022 May 15-18. p. 195.

Schmidt, M.W., and Jagoutz, O. 2017. The global systematics of primitive arc melts. Geochemistry, Geophysics, Geosystems, **18**: 2817–2854. doi:10.1002/2016GC006699.

Şengör, A.M.C., Natal'In, B.A., and Burtman, V.S. 1993. Evolution of the Altaid tectonic collage and Palaeozoic crustal growth in Eurasia. Nature, **364**: 299–307. doi:10.1038/364299a0.

Shand, S.J. 1943. Classic A/CNK vs A/NK plot for discriminating metaluminous, peraluminous and peralkaline compositions. New York., Hafner publishing co.

Shi, M., Hou, Q., Wu, C., Yan, Q., Wang, H.Y.C., Cheng, N., Zhang, Q.W.L., and Li, Z.M.G. 2020. Paleozoic Sanweishan arc in the northern Dunhuang region, NW China: The Dunhuang block is a Phanerozoic orogen, not a Precambrian block. Journal of Asian Earth Sciences, **194**: 103954. Elsevier. doi:10.1016/j.jseaes.2019.103954.

Song, D., Xiao, W., Han, C., Li, J., Qu, J., Guo, Q., Lin, L., and Wang, Z. 2013. Progressive accretionary tectonics of the Beishan orogenic collage, southern Altaids: Insights from zircon U-Pb and Hf isotopic data of high-grade complexes. Precambrian Research, **227**: 368–388. Elsevier B.V. doi:10.1016/j.precamres.2012.06.011.

van Staal, C.R., Hong, T., Lin, S., and Ji, W. 2019. Bedrock Geology: Baidunzi Area. doi:10.35080/data.C.2021.P01.

Stanley, C.R. 2020. Molar element ratio analysis of lithogeochemical data: a toolbox for use in mineral exploration and mining. Geochemistry: Exploration, Environment, Analysis, **20**: 233–256. doi:https://doi.org/10.1144/geochem2019-033.

Stanley, C.R., and Pearce, T.H. 1990. A Paradigm for Testing Hypotheses. **71**: 1–6.

Steiger, R.H., and Jäger, E. 1977. Subcommission on Geochronolgy: convention on the use of decay constants in geo- and cosmochronology. Earth and Planetary Science Letters, **36**: 359–362. doi:https://doi.org/10.1016/0012-821X(77)90060-.

Tian, Z., Xiao, W., Shan, Y., Windley, B., Han, C., Zhang, J., and Song, D. 2013. Mega-fold interference patterns in the beishan orogen (nw china) created by change in plate configuration during permo-triassic termination of the altaids. Journal of Structural Geology, **52**: 119–135. Elsevier Ltd. doi:10.1016/j.jsg.2013.03.016.

Vermeesch, P. 2018. IsoplotR: A free and open toolbox for geochronology. Geoscience Frontiers, **9**: 1479–1493. Elsevier Ltd. doi:10.1016/j.gsf.2018.04.001.

de Vries, J. 2020. A structural-metamorphic approach to deciphering the exhumation of the Gubaoquan eclogite in the Beishan Orogenic Collage, NW China. University of Waterloo. Available from https://uwspace.uwaterloo.ca/handle/10012/16655.

Wang, Y., Luo, Z., Santosh, M., Wang, S., and Wang, N. 2017a. The Liuyuan Volcanic Belt in NW China revisited: Evidence for Permian rifting associated with the assembly of continental blocks in the Central Asian Orogenic Belt. Geological Magazine, **154**: 265–285. doi:10.1017/S0016756815001077.

Wang, Z., Sun, S., Li, J., Hou, Q., Qin, K., Xiao, W., and Hao, J. 2003. Paleozoic tectonic evolution of the northern Xinjiang, China: Geochemical and geochronological constraints from the ophiolites. Tectonics, **22**: n/a-n/a. doi:10.1029/2002tc001396.

Wang, Z.M., Han, C.M., Xiao, W.J., and Sakyi, P.A. 2017b. Paleozoic subduction-related magmatism in the Duobagou area, Dunhuang block: Constrained by zircon U-Pb geochronology and Lu-Hf isotopes and whole-rock geochemistry of metaigneous rocks. Lithosphere, **9**: 1012–1032. doi:10.1130/L688.1.

Wilhem, C., Windley, B.F., and Stampfli, G.M. 2012. The Altaids of Central Asia: A tectonic and evolutionary innovative review. Earth-Science Reviews, **113**: 303–341. doi:10.1016/j.earscirev.2012.04.001.

Williams, I.S. 1997, January 1. U-Th-Pb Geochronology by Ion Microprobe. Society of Economic

Geologists. doi:10.5382/Rev.07.01.

Windley, B.F., Alexeiev, D., Xiao, W., Kröner, A., and Badarch, G. 2007. Tectonic models for accretion of the Central Asian Orogenic Belt. Journal of the Geological Society, **164**: 31–47. doi:10.1144/0016-76492006-022.

Xiao, W., Windley, B.F., Han, C., Liu, W., Wan, B., Zhang, J., Ao, S., Zhang, Z., and Song, D. 2018. Late Paleozoic to early Triassic multiple roll-back and oroclinal bending of the Mongolia collage in Central Asia. Earth-Science Reviews, **186**: 94–128. doi:10.1016/j.earscirev.2017.09.020.

Xiao, W.J., Mao, Q.G., Windley, B.F., Han, C.M., Qu, J.F., Zhang, J.E., Ao, S.J., Guo, Q.Q., Cleven, N.R., Lin, S.F., Shan, Y.H., and Li, J.L. 2010. Paleozoic multiple accretionary and collisional processes of the Beishan orogenic collage. American Journal of Science, **310**: 1553–1594. doi:10.2475/10.2010.12.

Yakubchuk, A. 2004. Architecture and mineral deposit settings of the Altaid orogenic collage: A revised model. Journal of Asian Earth Sciences, **23**: 761–779. doi:10.1016/j.jseaes.2004.01.006.

Zhang, J., and Cunningham, D. 2012. Kilometer-scale refolded folds caused by strike-slip reversal and intraplate shortening in the Beishan region, China. Tectonics, **31**. doi:10.1029/2011TC003050.

Zhang, J., Yu, S., Gong, J., Li, H., and Hou, K. 2013. The latest Neoarchean-Paleoproterozoic evolution of the Dunhuang block, eastern Tarim craton, northwestern China: Evidence from zircon U-Pb dating and Hf isotopic analyses. Precambrian Research, **226**: 21–42. Elsevier B.V. doi:10.1016/j.precamres.2012.11.014.

Zhao, Y., Sun, Y., Diwu, C., Guo, A.L., Ao, W.H., and Zhu, T. 2016. The Dunhuang block is a Paleozoic orogenic belt and part of the Central Asian Orogenic Belt (CAOB), NW China. Gondwana Research, **30**: 207–223. International Association for Gondwana Research. doi:10.1016/j.gr.2015.08.012.

Zhao, Y., Sun, Y., Diwu, C., Zhu, T., Ao, W., Zhang, H., and Yan, J. 2017. Paleozoic intrusive rocks from the Dunhuang tectonic belt, NW China: Constraints on the tectonic evolution of the southernmost Central Asian Orogenic Belt. Journal of Asian Earth Sciences, **138**: 562–587. Elsevier Ltd. doi:10.1016/j.jseaes.2017.02.037.

Zhao, Y., Sun, Y., Yan, J., and Diwu, C. 2015. The Archean-Paleoproterozoic crustal evolution in the

Dunhuang region, NW China: Constraints from zircon U-Pb geochronology and in situ Hf isotopes. Precambrian Research, **271**: 83–97. Elsevier B.V. doi:10.1016/j.precamres.2015.10.002.

Zong, K., Liu, Y., Zhang, Z., He, Z., Hu, Z., Guo, J., and Chen, K. 2013. The generation and evolution of Archean continental crust in the Dunhuang block, northeastern Tarim craton, northwestern China. Precambrian Research, **235**: 251–263. Elsevier B.V. doi:10.1016/j.precamres.2013.07.002.

Zong, K.Q., Zhang, Z.M., He, Z.Y., Hu, Z.C., Santosh, M., Liu, Y.S., and Wang, W. 2012. Early Palaeozoic high-pressure granulites from the Dunhuang block, northeastern Tarim Craton: Constraints on continental collision in the southern Central Asian Orogenic Belt. Journal of Metamorphic Geology, **30**: 753–768. doi:10.1111/j.1525-1314.2012.00997.x.

Zuo, G., Zhang, S., He, G., and Zhang, Y. 1991. Plate tectonic characteristics during the early paleozoic in Beishan near the Sino-Mongolian border region, China. Tectonophysics, **188**: 385–392. doi:10.1016/0040-1951(91)90466-6.

Appendix

Table 2: List and general description of all samples collected

Samples	Location	Lithology	Grain Size	Texture	Deformation	Other
17LYS-5018	40.82938252 N 95.5774242 E	Quartz-diorite	Fine to medium	Inequigranular	Non-foliated	Clinopyroxene remnant core with hornblende rim. Hornblende zones from brown core to green rim pleochroism.
19LYH-3586B	40.82934978 N 95.5868946 E	Quartz-diorite	Fine	Inequigranular, porphyritic	Weakly foliated	Hornblende and quartz intergrowth
19LYH-3586D	40.82934978 N 95.5868946 E	Quartz-diorite	Medium to coarse	Sub-equigranular	Weakly foliated	Many small inclusions in hornblende
19LYH-3586E	40.82934978 N 95.5868946 E	Quartz-diorite	Fine to medium	Porphyritic	Weakly foliated	Quartz intergrowth with hornblende
19LYH-3587A	40.82964861 N 95.5871950 E	Quartz-diorite	Medium	Equigranular	Strongly foliated	Some coarse plagioclase phenocrysts
19LYH-3587B	40.82964861 N 95.5871950 E	Quartz-diorite	Fine	Porphyritic	Non-foliated	Mafic inclusions in plagioclase phenocryst. Euhedral zircons.
19LYH-3588A	40.83016975 N 95.5873975 E	Quartz-diorite	Medium to very coarse	Porphyritic	Strongly foliated	Many inclusions in plagioclase and hornblende
20LYS-5301A	40.82934978 N 95.5868946 E	Quartz-diorite	Medium	Inequigranular, porphyritic	Strongly foliated and lineated	Plagioclase phenocrysts with polygonal quart, plagioclase, and xenoliths overgrowth. Clinopyroxene remnant core with hornblende rim.
20LYS-5301B	40.82934978 N 95.5868946 E	Quartz-diorite	Medium to coarse	Inequigranular	Strongly foliated and lineated	Hornblende intergrown with quartz. Clinopyroxene remnant core with hornblende rim.
20LYS-5303A	40.82934978 N 95.5868946 E	Quartz-diorite	Medium to very coarse	Equigranular	Strongly foliated	One very coarse phenocryst of plagioclase, foliation goes around it. Interstitial hornblende.
20LYS-5303B	40.82934978 N 95.5868946 E	Quartz-diorite	Fine to medium	Equigranular	Non-foliated	Few very coarse plagioclase phenocrysts. Clinopyroxene remnant core with hornblende rims. Hornblende zoning, brown to green/blue pleochroism

20LYS-5305A	40.82934978 N 95.5868946 E	Quartz-diorite	Medium	Equigranular	Non-foliated	Interstitial biotite. Many inclusions in plagioclase. Trace amount of olivine present.
20LYS-5305B	40.82934978 N 95.5868946 E	Quartz-diorite	Medium to coarse	Inequigranular	Non-foliated	Plagioclase rimmed by hornblende with pyroxene reaction rim between. Interstitial hornblende and biotite between plagioclase cumulate grains.
19LYH-3586A	40.82934978 N 95.5868946 E	Quartz-monzodiorite	Medium to coarse	Inequigranular	Non-foliated	Zircon inclusions in plagioclase. Interstitial hornblende and biotite. Myrmekite texture
19LYH-3586C	40.82934978 N 95.5868946 E	Quartz-monzodiorite	Medium to coarse	Inequigranular, porphyritic	Strongly foliated	Myrmekite texture. Zircon inclusions in plagioclase.
19LYH-3587C	40.82964861 N 95.5871950 E	Quartz-monzodiorite	Medium to coarse	Inequigranular, porphyritic	Strongly foliated	Myrmekite texture
20LYS-5304A	40.82934978 N 95.5868946 E	Quartz-monzodiorite	Medium to coarse	Inequigranular	Non-foliated	Myrmekite texture. Interstitial hornblende. Minor amount of clinopyroxene remnant core hornblende rim. Compositional zoned plagioclase.
20LYS-5304B	40.82934978 N 95.5868946 E	Quartz-monzodiorite	Medium to coarse	Inequigranular	Non-foliated	Myrmekite texture. Quartz mesh texture in hornblende and biotite. Minor amount of clinopyroxene remnant core hornblende rim.
20LYS-5302A	40.82934978 N 95.5868946 E	Granodiorite	Medium to coarse	Inequigranular	Non-foliated	Myrmekite texture. Zircon inclusions in biotite with halos. Compositional zoning in plagioclase.
20LYS-5302B	40.82934978 N 95.5868946 E	Granodiorite	Medium to coarse	Inequigranular	Non-foliated	Myrmekite texture. Zircon inclusions in biotite with halos. Compositional zoning in plagioclase

Table 3: Geochronological data for sample 17LYS-5018

Spot	U (ppm)	Th (ppm)	$^{232}Th/^{238}U$	$^{206}Pb_c$ %	(1) $^{207}Pb^*/^{235}U$	±%	Total $^{238}U/^{206}Pb$	±%	(1) $^{207}Pb^*/^{206}Pb^*$	±%	(1) $^{206}Pb/^{238}U$ Age	±	(1) $^{207}Pb/^{206}Pb$ Age	±	% Discordant
17LYS5018-A1	729	612	0.87	0.21	0.315	3.6	23.65	0.88	0.0541	3.5	267.0	±2.7	374	± 78	29
17LYS5018-A2	454	293	0.67	1.16	0.294	7.5	23.37	2.0	0.0505	7.2	269.0	±5.9	217	±170	-23
17LYS5018-A3	570	382	0.69	0.73	0.293	6.3	23.55	0.96	0.0504	6.3	268.2	±2.9	212	±140	-25
17LYS5018-A4	661	532	0.83	0.24	0.3172	3.0	23.43	0.91	0.0540	2.8	269.5	±2.9	373	± 64	28
17LYS5018-A5	459	356	0.80	--	0.339	7.0	23.58	1.0	0.0579	6.9	267.5	±3.1	528	±150	49
17LYS5018-A6	550	458	0.86	0.68	0.314	7.6	23.31	0.95	0.0535	7.5	272.0	±3.1	348	±170	23
17LYS5018-A7	516	402	0.80	0.64	0.304	5.1	23.07	0.99	0.0513	5.0	274.4	±3.1	253	±110	-8
17LYS5018-A8	729	602	0.85	0.55	0.312	6.4	22.85	0.89	0.0520	6.3	277.5	±2.8	286	±150	4
17LYS5018-A9	297	170	0.59	1.30	0.307	12	22.98	1.2	0.0519	12	274.0	±3.5	280	±280	3
17LYS5018-A10	334	198	0.61	5.55	0.246	23	20.84	1.2	0.0394	22	297.1	±4.8	-392	±590	173
17LYS5018-A11	465	317	0.71	0.87	0.293	7.1	23.50	1.0	0.0503	7.0	268.0	±3.0	209	±160	-27
17LYS5018-A12	227	124	0.56	1.86	0.276	22	23.22	1.3	0.047	22	269.4	±4.2	69	±520	-289
17LYS5018-A13	652	613	0.97	0.83	0.294	5.1	23.08	0.92	0.0497	5.0	276.5	±3.4	180	±120	-51
17LYS5018-A14	643	534	0.86	1.59	0.275	8.9	22.63	0.92	0.0458	8.8	280.3	±3.5	-13	±210	2284
17LYS5018-A15	157	99	0.65	2.41	0.270	15	22.78	1.5	0.0457	15	273.6	±4.8	-19	±360	1548

(1) Common Pb corrected using measured ^{204}Pb.

Underlined data: excluded due to being outliers

Table 4: Geochronological data for sample 20LYS-5301

Spot	U (ppm)	Th (ppm)	$^{232}Th/^{238}U$	$^{206}Pb_c$ %	(1) $^{207}Pb^*/^{235}U$	±%	Total $^{238}U/^{206}Pb$	±%	(1) $^{207}Pb^*/^{206}Pb^*$	±%	(1) $^{206}Pb/^{238}U$ Age	±	(1) $^{207}Pb/^{206}Pb$ Age	±	% Discordant
20LYS-5301-1	228	80	0.36	0.15	0.3149	3.0	22.13	1.4	0.0506	2.6	284.5	±3.8	223	± 61	-28
20LYS-5301-2	495	192	0.40	0.11	0.3097	2.3	23.34	1.3	0.05249	1.9	270.1	±3.5	307	± 43	12
20LYS-5301-3	340	166	0.50	0.11	0.3065	2.6	23.05	1.4	0.0513	2.3	273.5	±3.7	254	± 52	-7
~~**20LYS-5301-4**~~	~~1014~~	~~748~~	~~0.76~~	~~0.05~~	~~0.3015~~	~~1.8~~	~~23.36~~	~~1.2~~	~~0.05110~~	~~1.3~~	~~270.1~~	~~±3.3~~	~~245~~	~~± 30~~	~~-10~~
20LYS-5301-5	203	86	0.44	2.04	0.274	9.9	23.70	1.4	0.0480	9.8	261.1	±3.9	99	±230	-164
20LYS-5301-6	762	529	0.72	0.05	0.3030	1.9	23.49	1.3	0.05165	1.5	268.6	±3.3	270	± 33	0
~~**20LYS-5301-7**~~	~~951~~	~~916~~	~~1.00~~	~~0.00~~	~~0.2930~~	~~2.0~~	~~23.85~~	~~1.5~~	~~0.05067~~	~~1.3~~	~~264.8~~	~~±4.0~~	~~226~~	~~± 29~~	~~-17~~
20LYS-5301-8	91	35	0.40	0.26	0.239	7.0	28.1	4.5	0.0489	5.3	224.6	±9.9	142	±130	-59
20LYS-5301-9	261	100	0.40	0.19	0.3096	3.0	23.04	1.4	0.0518	2.7	273.4	±3.6	278	± 61	2
20LYS-5301-10	400	127	0.33	0.00	0.3001	2.4	23.05	1.4	0.05016	1.9	273.8	±3.8	203	± 43	-35
20LYS-5301-11	382	264	0.71	0.00	0.3120	2.2	22.93	1.3	0.05190	1.8	275.1	±3.5	281	± 42	2
20LYS-5301-12	346	293	0.87	0.00	0.3016	2.4	23.12	1.4	0.0506	2.0	273.0	±3.6	221	± 46	-23
20LYS-5301-13	312	127	0.42	0.15	0.3109	3.0	22.65	1.5	0.0512	2.6	278.1	±4.0	248	± 60	-12
20LYS-5301-14	675	186	0.28	0.04	0.3139	1.9	22.41	1.3	0.05105	1.5	281.3	±3.5	243	± 34	-16
20LYS-5301-15	389	196	0.52	0.11	0.3069	2.4	23.18	1.3	0.0516	2.0	272.0	±3.4	269	± 45	-1

(1) Common Pb corrected using measured ^{204}Pb.

Underlined data: excluded due to being outliers

Strikethrough data: excluded due to high uranium concentration

Table 5: Geochronological data for sample 20LYS-5302

Spot	U (ppm)	Th (ppm)	$^{232}Th/^{238}U$	$^{206}Pb_c$ %	(1) $^{207}Pb^*/^{235}U$	±%	Total $^{238}U/^{206}Pb$	±%	(1) $^{207}Pb^*/^{206}Pb^*$	±%	(1) $^{206}Pb/^{238}U$ Age	±	(1) $^{207}Pb/^{206}Pb$ Age	±	% Discordant
20LYS-5302-01	400	254	0.66	0.15	0.2964	2.6	23.91	1.3	0.0515	2.2	263.7	± 3.4	262	± 50	-1
20LYS-5302-2	225	153	0.70	0.22	0.2808	3.3	24.92	1.4	0.0509	2.9	253.1	± 3.6	235	± 68	-8
20LYS-5302-3	543	489	0.93	0.00	0.2991	2.1	23.32	1.3	0.05058	1.6	270.7	± 3.4	222	± 37	-22
20LYS-5302-4	413	197	0.49	0.16	0.2847	2.4	23.70	1.4	0.04903	2.0	266.0	± 3.7	149	± 46	-78
20LYS-5302-5	612	496	0.84	0.05	0.2991	2.0	23.96	1.3	0.05201	1.6	263.4	± 3.2	286	± 36	8
20LYS-5302-6	88	36	0.43	0.50	0.256	12	28.6	10	0.0534	5.5	221	±22	346	±130	36
20LYS-5302-7	105	39	0.38	0.00	0.311	3.9	22.69	1.6	0.0512	3.5	278.1	± 4.2	251	± 82	-11
20LYS-5302-8	142	55	0.40	0.00	0.303	3.4	23.58	1.5	0.0519	3.1	267.8	± 4.1	279	± 70	4
20LYS-5302-9	113	59	0.54	0.00	0.291	3.9	23.69	1.6	0.0500	3.6	266.5	± 4.2	194	± 84	-37
20LYS-5302-10	106	40	0.39	0.68	0.278	6.1	24.51	2.0	0.0497	5.7	256.0	± 5.1	181	±130	-41
20LYS-5302-11	68	25	0.38	0.89	0.282	9.0	24.95	3.1	0.0514	8.5	251.1	± 7.7	259	±190	3
20LYS-5302-12	529	311	0.61	0.05	0.3201	2.9	22.13	2.4	0.05141	1.7	284.7	± 6.7	259	± 38	-10
20LYS-5302-13	222	82	0.38	0.11	0.2993	3.1	23.41	1.4	0.0509	2.7	269.4	± 3.7	235	± 63	-15
20LYS-5302-14	443	178	0.41	0.00	0.3037	2.1	23.09	1.3	0.05087	1.7	273.3	± 3.4	235	± 40	-16
~~**20LYS-5302-15**~~	~~972~~	~~384~~	~~0.41~~	~~0.33~~	~~0.3089~~	~~2.2~~	~~23.00~~	~~1.2~~	~~0.05170~~	~~1.8~~	~~273.5~~	~~± 3.3~~	~~272~~	~~± 41~~	~~-1~~
20LYS-5302-16	147	87	0.61	~~0.27~~	0.291	3.8	23.77	1.5	0.0503	3.5	264.9	± 3.8	208	± 81	~~-27~~

(1) Common Pb corrected using measured ^{204}Pb.

Underlined data: excluded due to being outliers

Strikethrough data: excluded due to high uranium concentration

Table 6: Geochronological data for sample 20LYS-5304

Spot	U (ppm)	Th (ppm)	$^{232}Th/^{238}U$	$^{206}Pb_c$ %	(1) $^{207}Pb^*/^{235}U$	±%	Total $^{238}U/^{206}Pb$	±%	(1) $^{207}Pb^*/^{206}Pb^*$	±%	(1) $^{206}Pb/^{238}U$ Age	±	(1) $^{207}Pb/^{206}Pb$ Age	±	% Discordant
~~**20LYS-5304-1**~~	~~1542~~	~~1402~~	~~0.94~~	~~0.00~~	~~0.3404~~	~~1.5~~	~~23.96~~	~~1.2~~	~~0.05157~~	~~0.92~~	~~263.6~~	~~±3.1~~	~~267~~	~~± 21~~	~~1~~
20LYS-5304-2	544	322	0.61	0.13	0.3124	1.9	23.76	1.3	0.05087	1.6	265.4	±3.3	235	± 37	-13
~~**20LYS-5304-3**~~	~~1391~~	~~1387~~	~~1.03~~	~~0.10~~	~~0.3336~~	~~1.5~~	~~23.98~~	~~1.2~~	~~0.05142~~	~~1.2~~	~~263.1~~	~~±3.1~~	~~260~~	~~± 27~~	~~-1~~
~~**20LYS-5304-4**~~	~~1174~~	~~864~~	~~0.76~~	~~0.07~~	~~0.3206~~	~~1.7~~	~~23.67~~	~~1.3~~	~~0.05099~~	~~1.2~~	~~266.6~~	~~±3.5~~	~~240~~	~~± 28~~	~~-11~~
20LYS-5304-5	209	85	0.42	0.95	0.3222	2.9	22.80	1.4	0.0495	5.7	274.2	±3.8	172	±130	-60
20LYS-5304-6	567	311	0.57	0.13	0.3027	2.0	23.50	1.3	0.05096	1.6	268.3	±3.4	239	± 38	-12
20LYS-5304-7	422	153	0.37	0.13	0.2941	2.2	23.48	1.3	0.04994	1.9	268.5	±3.5	192	± 45	-40
20LYS-5304-8	450	154	0.35	0.19	0.3136	2.2	23.43	1.3	0.05109	1.9	268.9	±3.5	245	± 44	-10
20LYS-5304-9	721	374	0.54	0.10	0.3120	2.0	23.58	1.2	0.05086	1.8	267.5	±3.3	235	± 41	-14
20LYS-5304-10	462	173	0.39	0.21	0.3057	2.1	23.65	1.3	0.0510	2.4	266.4	±3.4	241	± 55	-11
20LYS-5304-11	414	162	0.41	0.15	0.3138	2.2	22.92	1.3	0.0509	2.2	274.9	±3.5	237	± 52	-16
~~**20LYS-5304-12**~~	~~943~~	~~647~~	~~0.71~~	~~0.03~~	~~0.3218~~	~~1.6~~	~~24.03~~	~~1.2~~	~~0.05022~~	~~1.2~~	~~262.7~~	~~±3.2~~	~~205~~	~~± 29~~	~~-28~~
20LYS-5304-13	525	238	0.47	0.00	0.3163	2.0	23.42	1.3	0.05165	1.6	269.6	±3.4	270	± 37	0
20LYS-5304-14	424	208	0.51	0.00	0.3096	2.2	23.59	1.3	0.05046	1.8	267.7	±3.5	216	± 42	-24
20LYS-5304-15	259	99	0.40	0.10	0.3133	2.7	23.07	1.4	0.0511	2.5	273.3	±3.6	246	± 58	-11

(1) Common Pb corrected using measured ^{204}Pb.

Underlined data: excluded due to being outliers

Strikethrough data: excluded due to high uranium concentration

Table 7: Geochronological measurements on Temora 1 standard zircons

Spot	U (ppm)	Th (ppm)	$^{232}Th/^{238}U$	% $^{206}Pb_c$	Total $^{206}Pb/^{238}U$	±%	$^{207}Pb/^{206}Pb$	±%
TEM-1	229	65	0.29	0.12	.175	1.6	.054	1.9
TEM-2	159	82	0.53	0.10	.177	2.4	.054	2.3
TEM-3	82	24	0.30	0.21	.174	1.2	.057	3.4
TEM-4	124	37	0.31	0.24	.175	2.6	.058	2.7
TEM-5	304	138	0.47	0.16	.173	3.2	.055	1.7
TEM-6	338	82	0.25	0.15	.157	3.4	.054	1.6
TEM-7	161	77	0.49	0.21	.165	3.1	.056	2.2
TEM-8	114	58	0.53	0.79	.180	3.5	.056	2.6
TEM-9	76	26	0.36	1.01	.178	3.6	.057	3.1
TEM-10	180	96	0.55	0.00	.177	2.7	.055	2.1
TEM-11	65	22	0.35	0.88	.178	1.9	.053	3.6
TEM-12	438	229	0.54	0.14	.171	2.4	.055	1.4
TEM-13	368	191	0.54	0.00	.174	1.8	.055	1.5
TEM-14	506	81	0.17	0.05	.175	2.4	.055	1.3
TEM-15	433	211	0.50	0.05	.164	3.5	.055	1.5

Table 8: Whole-rock geochemistry data for all samples

Sample	SiO_2	Al_2O_3	Fe_2O_3	CaO	MgO	Na_2O	K_2O	TiO_2	MnO	P_2O_5	LOI	Total
17LYS5018	51.08	15.80	10.90	8.81	5.86	3.51	0.53	2.04	0.18	0.29	0.63	99.63
19LYH-3586B	51.80	14.45	13.25	7.35	4.10	3.99	1.38	2.87	0.21	0.36	0.31	100.11
19LYH-3586D	54.10	14.95	10.60	8.29	5.53	3.74	1.08	1.97	0.17	0.24	0.61	101.34
19LYH-3586E	51.90	15.05	11.90	7.95	4.93	3.87	1.17	2.44	0.19	0.27	0.45	100.16
19LYH-3587A	53.30	16.45	8.03	9.10	6.64	3.91	1.16	1.21	0.13	0.15	0.62	100.79
19LYH-3587B	52.30	15.50	10.70	7.83	4.88	4.37	1.68	2.03	0.17	0.24	0.17	99.93
19LYH-3588A	49.50	21.30	6.76	11.10	5.27	3.29	0.76	1.15	0.11	0.14	1.19	100.63
20LYS-5301a	48.98	19.19	8.19	10.53	5.80	3.13	1.16	1.42	0.13	0.16	0.99	99.70
20LYS-5301b	53.72	16.49	8.46	8.38	5.34	3.44	1.37	1.54	0.14	0.17	0.74	99.79
20LYS-5303a	50.24	16.36	9.69	9.45	6.84	3.38	0.98	1.66	0.16	0.19	0.88	99.82
20LYS-5303b	51.76	16.54	9.25	9.54	6.11	3.48	0.74	1.57	0.15	0.16	0.58	99.86
20LYS-5305a	52.41	14.40	12.75	7.46	3.90	4.01	1.29	2.74	0.20	0.34	0.09	99.61
20LYS-5305b	52.89	14.39	12.25	7.43	3.88	4.04	1.47	2.72	0.19	0.32	0.17	99.75
19LYH-3586A	58.20	19.05	6.70	3.90	1.56	5.86	2.24	1.03	0.06	0.13	0.27	99.00
19LYH-3586C	59.90	18.10	5.76	3.88	1.62	5.01	3.74	0.92	0.09	0.13	0.52	99.91
19LYH-3587C	60.40	18.35	6.00	3.47	1.28	5.26	3.85	0.96	0.10	0.15	0.34	100.33
20LYS-5304a	60.26	16.29	7.93	3.41	1.60	4.63	3.31	1.10	0.13	0.17	0.65	99.48
20LYS-5304b	61.59	17.26	5.57	3.05	1.44	4.64	3.73	1.07	0.10	0.15	0.70	99.31
20LYS-5302a	66.27	16.36	3.52	3.61	1.59	4.40	2.41	0.68	0.05	0.20	0.67	99.77
20LYS-5302b	67.50	15.89	3.34	3.33	1.28	4.42	2.35	0.60	0.05	0.18	0.78	99.71

Table 8 Continued

Sample	As	Co	Cu	Li	Mo	Ni	Pb	Sc	Zn	Ba	Ce	Cr	Cs	Dy	Er	Eu	Ga	Gd	Hf
17LYS5018	1.00	37	33.3	18.80	0.7	23.70	4.5	34.20	103.0	66.80	38.80	133.0	1.21	7.7	4.3	1.8	22.10	7.4	5.8
19LYH-3586B	<5	35	33	20	1	7	6	34	132	168.5	45.4	20	1.21	11.3	6.26	2.02	23.9	11.3	7.9
19LYH-3586D	5	34	33	20	2	13	5	32	95	111	28.8	180	1.48	7.38	4.24	1.63	21.1	6.91	5.8
19LYH-3586E	<5	34	21	20	2	10	4	30	106	128	28.9	40	1.83	8.05	4.78	2.12	23.5	7.47	6.5
19LYH-3587A	<5	33	37	20	1	51	5	24	70	131	23.2	320	2.25	5.2	3.09	1.24	18.8	5.16	4.8
19LYH-3587B	5	32	24	30	<1	6	<2	31	106	266	32.6	60	1.36	8.1	4.83	1.8	22.8	8.08	6.3
19LYH-3588A	<5	27	28	20	1	34	2	16	53	34.4	14.3	140	3.97	3.78	2.16	1.12	17.9	3.75	2.4
20LYS-5301a	1.37	31.50	43.32	25.06	0.54	42.25	4.57	26.52	66.73	53.57	16.53	168.12	2.95	4.75	2.68	1.33	17.42	4.40	3.01
20LYS-5301b	1.35	30.71	26.50	29.32	0.88	34.75	5.43	28.86	81.10	121.52	29.10	151.38	3.59	6.28	3.55	1.43	19.60	5.97	8.37
20LYS-5303a	1.13	40.03	28.71	25.23	1.23	60.55	4.40	31.36	79.10	44.40	21.62	220.11	3.87	5.77	3.25	1.51	18.64	5.37	3.93
20LYS-5303b	1.06	34.14	21.21	19.31	0.78	26.49	3.80	32.28	79.75	61.53	21.69	216.19	2.01	5.67	3.26	1.47	18.72	5.23	4.18
20LYS-5305a	1.88	32.85	23.33	15.92	1.09	6.10	6.41	35.16	123.83	211.42	41.38	20.22	1.22	9.81	5.52	2.31	23.37	9.35	7.96
20LYS-5305b	2.08	32.28	22.55	16.01	1.00	6.61	6.31	36.04	120.08	193.42	38.73	21.54	1.44	9.64	5.39	2.30	23.85	9.01	7.60
19LYH-3586A	<5	15	6	30	1	1	7	6	114	350	30.6	20	2.07	4.1	2.68	1.54	30.5	5.01	16.1
19LYH-3586C	<5	11	7	20	<1	3	12	13	83	2090	30.2	20	2.13	5.57	3.03	2.01	24.5	5.93	14.3
19LYH-3587C	6	8	7	30	1	<1	11	9	97	1335	33.4	10	2.02	6.17	3.43	1.94	25.7	7.13	13.9
20LYS-5304a	2.19	13.24	5.55	21.68	0.33	3.37	13.71	18.20	123.57	1013.93	45.23	14.05	2.18	7.45	4.05	1.89	23.55	8.26	18.76
20LYS-5304b	1.51	10.56	3.36	24.97	0.20	2.08	14.76	11.16	81.91	2128.22	33.93	10.14	2.11	5.34	3.18	2.08	22.08	5.75	19.50
20LYS-5302a	1.01	7.67	8.50	26.61	0.19	2.55	10.71	7.26	69.88	268.32	45.24	16.93	4.11	1.94	0.89	1.06	21.75	2.78	5.27
20LYS-5302b	1.22	6.49	3.02	28.44	0.09	1.57	10.41	6.37	72.73	252.13	43.59	12.03	4.12	1.80	0.86	1.01	21.55	2.61	5.56

Table 8 Continued

Sample	Ho	La	Lu	Nb	Nd	Pr	Rb	Sm	Sn	Sr	Ta	Tb	Th	Tm	U	V	Y	Yb	Zr
17LYS5018	1.5	14.80	0.65	5.3	26.5	5.51	9.50	6.91	1.40	345	0.4	1.27	1.5	0.68	0.7	213.00	41.6	4.30	234.00
19LYH-3586B	2.2	16.2	0.87	7.3	34.6	7.01	27.8	10	1	221	1.3	1.75	0.83	0.86	0.44	278	57.1	5.8	311
19LYH-3586D	1.41	11	0.56	4	21.6	4.39	25.3	5.6	2	246	0.9	1.06	2.24	0.58	0.76	220	37.1	3.93	210
19LYH-3586E	1.48	11.1	0.61	5.1	23.5	4.43	27.7	6.5	2	247	1.4	1.13	1.16	0.6	0.58	256	40.6	4.01	266
19LYH-3587A	1.04	9.2	0.4	3	16.4	3.36	37.5	4.38	1	236	0.9	0.77	1.68	0.42	0.76	168	28.2	2.88	165
19LYH-3587B	1.67	12.8	0.63	5.1	23.9	4.98	44.2	6.46	1	237	0.3	1.33	1.07	0.66	0.67	217	42.2	4.3	240
19LYH-3588A	0.76	5.4	0.31	2.7	10.9	2.24	23.8	3	2	358	0.2	0.6	0.8	0.33	0.38	137	20.8	2.18	92
20LYS-5301a	0.99	5.69	0.38	2.41	13.02	2.53	37.83	3.88	1.62	304.79	0.18	0.74	0.66	0.40	0.49	176.41	27.82	2.52	124.73
20LYS-5301b	1.32	10.79	0.52	4.30	19.72	4.11	45.27	5.49	1.77	250.21	0.32	1.00	1.88	0.55	0.97	177.92	37.11	3.41	326.90
20LYS-5303a	1.20	7.68	0.46	2.98	16.25	3.23	28.13	4.77	2.77	266.38	0.23	0.92	1.39	0.49	0.86	212.75	33.56	3.05	157.17
20LYS-5303b	1.20	7.88	0.47	3.36	15.87	3.15	18.74	4.65	1.97	262.68	0.26	0.90	1.78	0.49	0.67	210.53	33.50	3.09	161.46
20LYS-5305a	2.05	15.34	0.79	6.94	30.36	6.22	30.47	8.46	1.45	236.98	0.51	1.56	1.19	0.83	0.63	257.03	58.01	5.19	322.21
20LYS-5305b	2.00	14.52	0.78	6.94	27.94	5.83	37.09	8.17	1.72	236.58	0.50	1.53	1.41	0.81	0.67	256.43	56.78	5.13	314.34
19LYH-3586A	0.83	14.4	0.39	4.9	18	3.89	48.2	5.01	2	203	1.2	0.66	2.51	0.37	1.4	111	22.2	2.31	594
19LYH-3586C	1.05	13	0.49	7.9	19.8	4.14	50.7	5.13	1	241	1.8	0.84	2.16	0.47	1.36	70	27.7	3.33	514
19LYH-3587C	1.26	14.4	0.49	7.9	23	4.93	53.6	5.89	2	230	0.5	1.04	1.76	0.49	1.24	58	31.2	3.25	529
20LYS-5304a	1.52	19.42	0.63	10.47	30.65	6.31	39.24	7.79	1.85	210.44	0.58	1.26	3.39	0.61	1.93	58.56	40.76	3.95	703.56
20LYS-5304b	1.14	14.60	0.52	8.51	21.52	4.51	45.72	5.45	1.27	250.41	0.56	0.88	3.26	0.49	1.92	41.76	31.49	3.25	728.48
20LYS-5302a	0.35	21.29	0.11	4.89	19.64	5.25	56.74	3.71	1.74	484.59	0.40	0.38	4.78	0.12	1.42	44.87	10.57	0.76	219.26
20LYS-5302b	0.33	21.03	0.11	5.06	18.54	5.03	58.19	3.44	2.06	452.48	0.42	0.36	4.49	0.12	1.38	35.28	10.06	0.75	235.43